PHYSIK-DEPARTMENT

Non-equilibrium Field Theory of Condensed Matter Systems – Periodic Driving and Quantum Quenches

Dissertation
von

Simon Adrian Weidinger

TECHNISCHE UNIVERSITÄT
MÜNCHEN

TECHNISCHE UNIVERSITÄT
MÜNCHEN

PHYSIK-DEPARTMENT
Lehrstuhl für Kollektive Quantendynamik, Univ.-Prof. Dr. Michael Knap

Non-equilibrium Field Theory of Condensed Matter Systems – Periodic Driving and Quantum Quenches

Simon Adrian Weidinger

Vollständiger Abdruck der von der Fakultät für Physik der Technischen Universität München zur Erlangung des akademischen Grades eines

Doktors der Naturwissenschaften (Dr. rer. nat.)

genehmigten Dissertation.

Vorsitzender: Univ.-Prof. Christian Pfleiderer, Ph.D.

Prüfer der Dissertation:

1. Univ.-Prof. Dr. Michael Knap
2. Univ.-Prof. Dr. Wilhelm Zwerger

Die Dissertation wurde am 27.09.2018 bei der Technischen Universität München eingereicht und durch die Fakultät für Physik am 20.11.2018 angenommen.

Abstract

Quantum many-body systems far from equilibrium can show a wide range of different phenomena. Understanding non-equilibrium many-body systems is a non-trivial task, as one has to deal with a fully-time dependent situation and interactions. Field theoretic methods can provide insight into non-equilibrium physics. In this thesis we apply conserving approximations to study heating and dynamical quantum phase transitions in the $O(N)$-model, many-body localization of spinless lattice fermions and the dynamical full counting statistics after quenches in a Luttinger liquid.

Kurzfassung

Quantenvielteilchensysteme weit ab vom Gleichgeweicht zeigen eine große Bandbreite an verschiedenen Phänomenen. Es ist eine nichttriviale Aufgabe nichtgleichgewichts Quantenvielteilchensysteme zu verstehen, da man sowohl mit einer voll zeitabhängigen Situation als auch auch Wechselwirkungen konfrontiert ist. Feldtheoretische Methoden können Einsichten in die Nichtgleichgewichtsphysik liefern. In dieser Arbeit werden wir "erhaltende Näherungen" anwenden um das Heizen und dynamische Quantephasenübergänge im $O(N)$-Model, Vielteilchenlokalisierung von spinlosen Gitterfermionen und die "Full counting Statistik" nach Quenchen in einer Luttinger-Flüssigkeit zu untersuchen.

Contents

Chapter 1

Introduction

Quantum many-body systems far from equilibrium show a wide range of different phenomena and there are also many different ways to create non-equilibrium states. Furthermore, non-equilibrium states pose questions reaching from a fundamental to a practical level.
For the fundamental understanding of statistical mechanics and thermodynamics, the question if and how an isolated system reaches (thermal) equilibrium is highly relevant. Due to the unitary time evolution of isolated quantum systems entropy is conserved and it is not obvious how a thermal ensemble can be reached.
For generic many-body systems, the eigenstate thermalization hypothesis (ETH) [1, 2, 3, 4] provides a framework for understanding, why expectation values of observables at late times can be correctly obtained from the microcanonical ensemble, even if the system was initially in a state far from equilibrium.
However, there are also systems for which the ETH does not apply and that will never reach (thermal) equilibrium. Examples are integrable systems [5, 6, 7] possessing an infinite number of conserved quantities as well as disordered (many-body) localized systems [8, 9, 10, 11, 12].
Besides for statistical mechanics, an understanding of non-equilibrium quantum many-body systems is also essential for various different fields in physics such as optical, atomic and molecular physics, condensed matter physics and also cosmology. Also technological applications such as electronic devices like microchips or memory disks an understanding of (heat-) transport processes is key.
A system can be driven into a non-equilibrium state in different ways. In so called Floquet systems, the Hamiltonian itself is time-periodic, which is usually implemented with a periodic drive term. Floquet systems have become of major interest, as one can engineer specific non-trivial Hamiltonians with certain driving protocols, which host novel phases [13, 14, 15, 16, 17, 18, 19, 20, 21, 22, 23] such as time crystals [13, 16, 20, 21, 22, 23].
Another possibility is to consider quantum quenches, where the initial quantum state is not an eigenstate of the Hamiltonian, which governs the time evolution. Quantum quenches can be used to glean insight into highly excited states and to study the occurence of dynamical quantum phase transitions [24, 25, 26].
One can also introduce disorder into a system [8, 9, 10, 11, 12]. For non-interacting systems, the effects of disorder are well understood; with interactions, it is less clear. For instance one dimensional interacting systems can be either localized or delocalized depending on the disorder strength, while a non-interacting system would always be insulating as long as there is finite disorder. A characterization

of the transition between localized and ergodic behavior is still missing. These ways of creating an equilibrium situation are of course not exclusive and can all be combined.
Understanding non-equilibrium many-body systems is a non-trivial task, as one needs to deal both with a time-dependent situation and interactions.
One possible way is to use quantum optical and atomic synthetic many-body systems [27, 28, 29, 30, 31, 32, 33, 34, 35, 36]. Systems of atoms in optical lattices are very clean, almost isolated and have a very high degree of controllability. Furthermore many probes are available in these systems. Single-site resolution for example enables one to read out the occupation of single lattice sites, which gives access to time-resolved single site occupations and correlation-functions [37, 38, 39, 40, 41, 42]. All in all, these advantages have made synthetic many-body systems a highly valued tool in the "quantum simulation" of non-equilibrium systems. However, also condensed matter systems together with ultrafast spectroscopy [43, 44] are successfully used to explore non-equilibrium physics.

On the theoretical side, quantum field theoretic methods [45, 46] can provide lots of theoretical insight and understanding into non-equilibrium physics. In this thesis we apply conserving approximations [47, 48, 49] to study different models and non-equilibrium situations and build clear physical pictures on top of the results. We will use both large-N [48, 49] as well as small coupling expansions.
As models we will study the $O(N)$-model of relativistic scalar fields [50], the Tomanaga-Luttinger model [51, 52] and the Fermi-Hubbard model, which are paradigmatic models for quantum many-body systems.
Due to the quite diverse range of considered models and situations, we prefer to keep this introducation rather unspecific at this point and will give more focused introductions at the beginning of the respective chapters.
This thesis is mainly based on the following publications of the author:

[1] **Simon A. Weidinger**, Michael Knap, "Floquet prethermalization and regimes of heating in a periodically driven, interacting quantum system", *Scientific Reports* **7**, 45382 (2017)

[2] **Simon A. Weidinger**, Markus Heyl, Alessandro Silva, Michael Knap, "Dynamical Quantum Phase Transitions in Systems with Continuous Symmetry Breaking", *Phys. Rev. B* **96**, 134313 (2017)

[3] **Simon A. Weidinger**, Sarang Gopalakrishnan, Michael Knap, "A self-consistent Hartree-Fock approach to Many-Body Localization", *arXiv:*1809.02137 (2018)

The author of this thesis has made significant and substantial contributions to these publications, from contributions to the development of ideas, literature research, analytical calculations, design, development and implementation of numerical code, to the interpretation of results and writing of the papers.

The thesis is organized as follows: Ch. 2 gives a short technical introduction to non-equilibrium field theory and the 2PI effective action formalism, using the $O(N)$-model, Sec. 2.2, and lattice fermions, Sec. 2.3, as examples.
In Ch. 3 we study heating in the periodically driven $O(N)$-model using the large-N expansion to next-to-leading order. In Sec. 3.2 we lay out how the energy density can be obtained from two-point functions. Sec. 3.3 discusses the different heating regimes and shows that there is a intermediate regime where the system ceases to absorb energy. In Sec. 3.4 we discuss the leading order dynamics. In Sec. 3.5 we compare these findings to a model with time-dependent noise.
In Ch. 4 we study dynamical quantum phase transition in the quench dynamics of the $O(N)$-model with a leading order large-N approximation. Sec. 4.1 discusses two different notions of dynamical quantum phase transitions, in Sec. 4.2 we calculate the time evolution of a symmetry-breaking intial state and in Sec. 4.3 we calculate the return probability to the ground state manifold and furthermore show, that an intimate connection between the two different notions of dynamical quantum phase transitions exists in our model.
In Ch. 5 we study a model of spin-less lattice fermions with nearest-neighbor repulsion subject to a disorder potential by means of a self-consistent Hartree-Fock approach. Sec.'s 5.1 and 5.2 give a short introduction to many-body localization and the studied model. In Sec. 5.3 we look at the decay of different initial states and the differences between random and quasi-periodic disorder. In Sec. 5.4 we show that the local spectral function has sharp peaks in the localized phase, while it shows a broad spectrum in the delocalized phase. In Sec. 5.5 we analyze the amplitude-spectrum and the auto-correlations of the Hartree-Fock self-energy and argue, that the delocalization can be understood by noticing, that the Hartree-Fock self-energy acts as "self-consistent noise". In Sec. 5.6 we compare Hartree-Fock to exact diagonalization, in Sec. 5.7 we show what effects higher-order contributions could have. In Sec. 5.8 we look at the occupation dynamics of single sites for single disorder realizations, in order to show, that the decay of initial states is not just an effect of dephasing at leading order and in Sec. 5.9 we look at the difference between Hartree, Fock and Hartree-Fock simulations.
In Ch. 6 we study the full counting statistics of the particle number in a given, connected subsystem, after a quench from a gapped state to a gapless Tomanaga-Luttinger liquid. Sec. 6.1 we gives an overview over previous works investigating the connection of full counting statistics and entanglement entropy. In Sec. 6.2 we calculate the dynamics after a quench from the Mott-insulating to the superfluid phase in the one-dimensional Bose Hubbard model, using Luttinger liquid theory as an effective description. In Sec. 6.3 we use the results from Sec. 6.2 to calculate the full counting statistics and the number fluctuations after the quench. We show, that fluctuations grow linearly before saturating, similar to the entanglement entropy. In Sec. 6.4 we compare our findings from Luttinger liquid theory with numerical MPS simulations and show that predictions from Luttinger liquid theory are indeed observable. In Sec. 6.5 we use our findings to propose an experimental measurement procedure for the Luttinger parameter and test the procedure on

numerical data for small systems, showing that it works in principle.
Finally, we conclude in Ch. 7

Chapter **2**

The 2PI - Keldysh formalism

2.1 The closed time contour

Consider a situation, where a quantum system is initially prepared in a possibly mixed state $\hat{\rho}_0$ and its is evolution is governed by the possibly time dependent Hamiltonian $\hat{H}(t)$. Trotterization of the time evolution then leads to the evolution operator

$$\hat{U}(t,t') = \hat{\mathbb{T}} \exp\left\{-i \int_{t'}^{t} ds \hat{H}(s)\right\}, \tag{2.1}$$

where $\hat{\mathbb{T}}$ denotes the time-ordering of the exponential. Now we are interested in the expectation value of an observable $\hat{A}$ at a given time t. Using the Heisenberg picture of quantum mechanics, we obviously have

$$\langle \hat{A} \rangle (t) = \mathrm{tr}\left\{\hat{A}(t)\hat{\rho}_0\right\} = \mathrm{tr}\{\hat{U}^\dagger(t,0)\hat{A}\hat{U}(t,0)\hat{\rho}_0\} = \mathrm{tr}\left\{\hat{U}(0,t)\hat{A}\hat{U}(t,0)\hat{\rho}_0\right\}. \tag{2.2}$$

Eq. (2.2) is the essential observation, which leads to the introduction of the so called closed time or Keldysh-contour $\mathcal{C}$, graphically depicted in Fig. 2.1, which was first considered by Schwinger [45]. On the right hand side of Eq. (2.2) we see, that the system is first propagated from zero to time t, where the observable acts and than back from time t to time 0. Looking at Eq. (2.2), the closed time contour is acutally the most natural way to depict the time evolution of a quantum system, even in equilibrium.
In order to calculate correlation functions of the observable $\hat{A}$, for instance two-point functions, it is beneficial to introduce a generating functional. This can be done by adding a source term to the Hamiltonian [46],

$$\hat{H}(t) \longrightarrow \hat{H}_J^{\pm}(t) = \hat{H}(t) + J^{\pm}(t)\hat{A}, \tag{2.3}$$

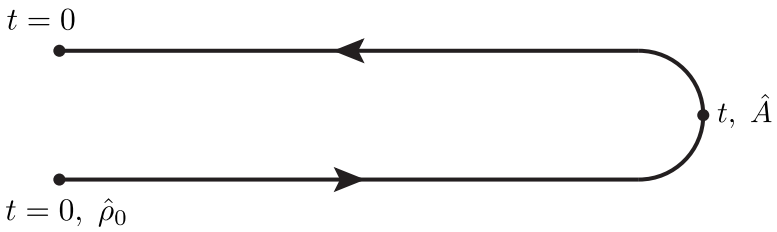

Figure 2.1: **The Keldysh closed time contour** $\mathcal{C}$

and defining

$$\mathcal{W}[J] = i \log \mathrm{tr}\Big\{ \hat{U}[J](0,t)\hat{U}[J](t,0)\hat{\rho}_0 \Big\}, \tag{2.4}$$

where $\hat{U}[J](t,0)$ is the time evolution operator corresponding to the Hamiltonian $\hat{H}_J^{\pm}(t)$. In Eq. (2.3) plus sign is used on the lower branch and the minus sign on the upper branch of the contour. This ensures that the source term does not cancel out and the generating function, Eq. (2.4) becomes non-trivial.
From the generating functional $\mathcal{W}[J]$, Eq. (2.4), we can now obtain correlation functions of the observable by calculating functional derivatives with respect to the source field $J^{\pm}(t)$,

$$\langle \hat{\mathbb{T}}_{\mathcal{C}} \hat{A}(t_1)\hat{A}(t_2)\cdots\hat{A}(t_n)\rangle = i^{n-1} \frac{\delta \mathcal{W}[J]}{\delta J^{\pm}(t_1)\delta J^{\pm}(t_2)\cdots\delta J^{\pm}(t_n)}, \tag{2.5}$$

here $\hat{\mathbb{T}}_{\mathcal{C}}$ indicates contour-ordering, i.e. the times $t_1, t_2, \ldots, t_n$ are ordered according to their appearence on the closed time contour.
In order to make formal manipulations shorter in notation, one usually interprets functions as defined on the Keldysh contour $J : \mathcal{C} \longrightarrow \mathbb{R}$ and defines the so called contour evolution operator

$$\hat{U}_{\mathcal{C}}[J] = \hat{U}[J](0,t)\hat{U}[J](t,0) \equiv \hat{\mathbb{T}}_{\mathcal{C}} \exp\left\{ -i \int_{\mathcal{C}} dt \hat{H}_J(t) \right\}. \tag{2.6}$$

With this, we can rewrite Eq. (2.5) in a simpler form:

$$\begin{aligned} \mathcal{W}[J] &= i \log \mathrm{tr}\Big\{ \hat{U}_{\mathcal{C}}[J]\hat{\rho}_0 \Big\} \\ \langle \hat{\mathbb{T}}_{\mathcal{C}} \hat{A}(t_1)\hat{A}(t_2)\cdots\hat{A}(t_n)\rangle &= i^{n-1} \frac{\delta \mathcal{W}[J]}{\delta J(t_1)\delta J(t_2)\cdots\delta J(t_n)}. \end{aligned} \tag{2.7}$$

Here we want to note, that even though Eq. (2.7) can simplify formal manipulations considerably, we will need to make the contour structure explicit again, when we perform numerical simulations.
In general the quantities of physical interest are the expectation value and the correlation functions of the observable $\hat{A}$, therefor it would be desirable to have a parameterization of the theory directly in terms of these quantities and not the source field J. This can be be achieved by a Legendre transform in an analogous fashion to equilibrium thermodynamics. The expectation value of $\hat{A}(t)$ in the presence of the source J is

$$A(t) \equiv \langle \hat{A}(t) \rangle = \frac{\delta W[J]}{\delta J(t)}, \tag{2.8}$$

hence we have

$$\Gamma[A] = W[J] - \int_{\mathcal{C}} dt' A(t')J(t')$$
$$\frac{\Gamma[A]}{\delta A(t)} = -J(t). \tag{2.9}$$

One can now also introduce a source, then defined on $\mathcal{C} \times \mathcal{C}$, for two-point functions of $\hat{A}(t)$ or even n-point functions.
In the following two sections, we will make the rather general discussing above more concrete, by applying them to two different models: The linear $O(N)$-model of relativistic scalar fields and spin-less fermions in a lattice. We will see, that upon including two-points functions and setting source fields to zero, Eq. (2.9) will yield a closed set of evolution equations directly for the expectation and two-point functions of the observable.

2.2 Relativistic scalar fields

As first concrete example for the application of the 2PI - Keldysh formalism we take the linear $O(N)$-model of a relativistic real scalar field [50]. Since we only want to focus on the technicalities of the method, we postpone a discussion of how the O(N)-model is physically relevant to a later chapter. Also, we will not discuss any particular protocol of how the system is driven out of equilibrium at the moment. The classical action S of the model is defined as

$$S[\mathbf{\Phi}] = \int_{x,\mathcal{C}} \left[\frac{1}{2}(\partial_t \Phi_a)^2 - \frac{1}{2}(\nabla \Phi_a)^2 - \frac{1}{2} m^2(t) \Phi_a \Phi_a - \frac{\lambda}{4!N} (\Phi_a \Phi_a)^2 \right], \tag{2.10}$$

where we already assume that time runs on the closed-time Keldysh contour $\mathcal{C}$. The real scalar field $\mathbf{\Phi}$ has N components labeled by $a = 1, 2, \ldots, N$ and summation over field components is assumed. We use a relativistic notation $x = (t, \boldsymbol{x})$ and $\int_{x,\mathcal{C}} = \int d^d x \int_{t,\mathcal{C}}$. An important feature of Eq. 2.10 is, that the action scales linearly with the number of field components, $S \sim N$, as it will enable an expansion of the effective action, which is non-perturbative in the coupling λ [48, 49].
Following the general outline in the previous section, we introduce source fields $J_a(x)$, $R_{ab}(x,y)$ for the vacuum expectation value $\phi_a(x) = \langle \Phi_a(x) \rangle$ and the contour-ordered Green's function $G_{ab}(x,y)$, respectively. The so called Schwinger functional, $W[J,R]$, is then defined as

$$W[J,R] = -i \log \int \mathcal{D}\Phi \exp\Bigg\{ iS[\mathbf{\Phi}] + i \int_{x,\mathcal{C}} J_a(x)\Phi_a(x) + \frac{i}{2} \int_{x,y,\mathcal{C}} R_{ab}(x,y)\Phi_a(x)\Phi_b(y) \Bigg\}. \tag{2.11}$$

Accordingly, the vacuum expectation value (VEV) and the two-point Green's functions are obtained as the functional derivatives of the Schwinger functional with respect to the source fields,

$$\begin{aligned}\phi_a(x) &= \frac{\delta W[J,R]}{\delta J_a(x)} \\ G_{ab}(x,y) &= 2\frac{\delta W[J,R]}{\delta R_{ab}(x,y)} - \phi_a(x)\phi_b(y).\end{aligned} \tag{2.12}$$

Next we perform a Legendre transformation of $W[J,R]$ with respect to the source terms and use the VEV and the Green's function directly as variables to parametrize the theory. As already discussed in the previous section, this yields an equivalent description of the physics, however with the advantage that one is working directly with the quantities of interest.

$$\begin{aligned}\Gamma[\phi,G] =& W[J,R] - \int_{x,\mathcal{C}} \frac{\delta W[J,R]}{\delta J_a(x)} J_a(x) - \int_{x,y,\mathcal{C}} \frac{\delta W[J,R]}{\delta R_{ab}(x,y)} R_{ab}(x,y) \\ =& W[J,R] - \int_{x,\mathcal{C}} \phi_a(x) J_a(x) \\ & - \frac{1}{2}\int_{x,y,\mathcal{C}} \Big(G_{ab}(x,y) + \phi_(x)\phi_b(y) \Big) R_{ab}(x,y)\end{aligned} \tag{2.13}$$

The quantum equations of motion for the field expectation ϕ and the Green's function G in the presence of sources are now obtained via functional differentiation,

$$\begin{aligned}\frac{\delta\Gamma[\phi,G]}{\delta\phi_a(x)} &= -J_a(x) - \int_{y,\mathcal{C}} R_{ab}(x,y)\phi_b(y) \\ \frac{\delta\Gamma[\phi,G]}{\delta G_{ab}(x,y)} &= -\frac{1}{2}R_{ab}(x,y).\end{aligned} \tag{2.14}$$

In order to get the pure evolution of the system not subject to any external source field, one just has to put $J_a(x) \equiv 0$, $R_{ab}(x,y) \equiv 0$.
To make further progress, one is now faced with the task of finding an explicit expression for the effective action $\Gamma[\phi,G]$. Before attempting to perform an perturbative expansion of any kind, it is beneficial to integrate out the 1-loop part in the Schwinger functional, Eq. 2.11, in a saddle-point fashion. This leads to the following decomposition of the effective action [48]:

$$\Gamma[\phi,G] = S[\phi] + \frac{i}{2}\,\mathrm{tr}_{\mathcal{C}}\log G^{-1} + \frac{i}{2}\,\mathrm{tr}_{\mathcal{C}}\, G_0^{-1}G + \Gamma_2[\phi,G], \tag{2.15}$$

where the first three terms constitute the saddle-point result and $\Gamma_2[\phi,G]$, called the 2PI effective action, contains all the interaction effects. The 2PI effective action is the non equilibrium equivalent of the Luttinger-Ward functional in equilibrium [53,

54, 47]. G_0 is the classical propagator or bare Green's function, and is given by

$$iG^{-1}_{0,ab}(x,y;\phi) = \frac{\delta^2 S[\phi]}{\delta\phi_a(x)\delta\phi_b(y)} = -\left(\Box_x + m^2 + \frac{\lambda}{3!N}(\phi_c(x))^2\right)\delta_{ab}\delta_{\mathcal{C}}(x-y) - \frac{\lambda}{3N}\phi_a(x)\phi_b(x)\delta_{\mathcal{C}}(x-y). \tag{2.16}$$

The important theoretical result is, that Γ_2 is formally the sum of all 2-particle irreducible (2PI) vacuum diagrams of $S_{\text{int}}[\phi,\varphi]$, where S_{int} consists of all terms in $S[\phi+\varphi]-S[\phi]$ of order three or higher in φ, hence the name 2PI effective action. The vacuum diagrams have to be computed with the full propagator G as lines and no tadpoles in φ. A Feynman diagram qualifies as two-particle irreducible if remains connected upon removing two Green's function lines. Removing a Green's function line from a diagram corresponds to a functional derivative with respect to G. It turns out, that the self-energy in our approach is given by the first derivative of Γ_2 with respect to G, as we will shortly see. Therefor, the fact that Γ_2 is the sum of all two-particle irreducible diagrams ensures, that we get a proper selfenergy. For the given model the interaction part of the action is

$$S_{\text{int}}[\phi,\varphi] = -\int_{x,\mathcal{C}}\left(\frac{\lambda}{3!N}\phi_a(x)\varphi_a(x)\varphi_b(x)\varphi_b(x) + \frac{\lambda}{4!N}\left(\varphi_a(x)\varphi_a(x)\right)^2\right). \tag{2.17}$$

If we use the representation Eq. (2.15), we can rewrite the equation of motion, Eq. (2.14), for the Green's function as

$$\begin{aligned} G^{-1}_{ab}(x,y) &= G^{-1}_{0,ab}(x,y) - iR_{ab}(x,y) - \Sigma_{ab}(x,y;\phi,G) \\ \Sigma_{ab}(x,y;\phi,G) &= 2i\frac{\delta\Gamma_2[\phi,G]}{\delta G_{ab}(x,y)}, \end{aligned} \tag{2.18}$$

where we have already put the source fields to zero. Eq. (3.3) just constitutes Dyson's equation on the closed-time Keldysh contour. It is important to note, that Eq. (3.3) are exact and involve no approximation so far. However, one is stilled faced with the problem of finding an explicit expression for the 2PI effective action Γ_2.

Kadanoff - Baym equations

For now let us proceed without specifying the 2PI effective action. In the current form Dyson's equation on the closed-time contour is not helpful for practical applications, we will now recast it in a from, which can be tackled numerically. We will make the simplifying assumption, that the vacuum expectation value vanishes, $\phi_a = 0$, to keep the discussion simple. Physically, this corresponds to the system being in the gapped phase, where the $O(N)$-symmetry is not broken, which will be the case in the following chapter, where we make use of the method to study

heating in the $O(N)$-model. We start by bringing the Green's function G to the right hand side and explicitly inserting the free inverse Green's function G_0^{-1}:

$$\left(\Box_x + m^2\right) G_{ab}(x,y) + i\int_{z,\mathcal{C}} \Sigma_{ac}(x,z)G_{cb}(z,y) = -i\delta_{ab}\delta_{\mathcal{C}}(x-y) \tag{2.19}$$

In dealing with a theory of real scalar fields it is favorable to decompose the Green's function $G_{ab}(x,y)$ defined on the closed-time contour $\mathcal{C}$ into its statistical and spectral components $F_{ab}(x,y)$ and $\rho_{ab}(x,y)$, respectively. They are defined as

$$\begin{aligned} F_{ab}(x,y) &= \frac{1}{2}\langle\{\Phi_a(x),\Phi_b(y)\}\rangle \\ \rho_{ab}(x,y) &= i\langle[\Phi_a(x),\Phi_b(y)]\rangle \end{aligned} \tag{2.20}$$

Both functions are real, with F being symmetric under an exchange $x,a \longleftrightarrow y,b$ and ρ being anti-symmetric. The canonical commutation relations obeyed by the scalar field and its first time-derivative imply the following two useful relations for the spectral function:

$$\begin{aligned} \rho_{ab}(x,y)|_{x^0=y^0} &= 0 \\ \partial_{x^0}\rho_{ab}(x,y)|_{x^0=y^0} &= \delta_{ab}\delta(\boldsymbol{x}-\boldsymbol{y}) \end{aligned} \tag{2.21}$$

The two-point contour-ordered Green's function can be expressed in terms of the statistical and spectral function,

$$G_{ab}(x,y) = F_{ab}(x,y) - \frac{i}{2}\mathrm{sgn}_{\mathcal{C}}(\mathrm{x}^0-\mathrm{y}^0)\text{æ}_{\mathrm{ab}}(\mathrm{x},\mathrm{y}), \tag{2.22}$$

which follows from simple algebra.
Inserting the decomposition, Eq. (2.22), into Eq. (2.19) , making the contour integration explicit and splitting the resulting equation into real and imaginary parts, we obtain the Kadanoff-Baym equations,

$$\begin{aligned} \left[\Box_x\delta_{ac} + M^2_{ac}(x)\right] F_{cb}(x,y) = &-\int_0^{x^0} dz^0 \int d^dz \Sigma^{\rho}_{ac}(x,z)F_{cb}(z,y) \\ &+\int_0^{y^0} dz^0 \int d^dz \Sigma^{F}_{ac}(x,z)\rho_{cb}(z,y) \\ \left[\Box_x\delta_{ac} + M^2_{ac}(x)\right] \rho_{cb}(x,y) = &-\int_{y^0}^{x^0} dz^0 \int d^dz \Sigma^{\rho}_{ac}(x,z)\rho_{cb}(z,y), \end{aligned} \tag{2.23}$$

which govern the time evolution of the statistical function F_{ab} and the spectral function ρ_{ab}. The self-energy is decomposed in the same way as the Green's function

into a statistical and a spectral part, after splitting of the local part, which just gives a renormalization of the bare mass.

$$\begin{aligned}\Sigma_{ab}(x,y) &= -i\Sigma^{(0)}_{ab}(x)\delta_{\mathcal{C}}(x-y) + \bar{\Sigma}_{ab}(x,y)\\ \bar{\Sigma}_{ab}(x,y) &= \Sigma^{F}_{ab}(x,y) - \frac{i}{2}\mathrm{sgn}_{\mathcal{C}}(x^0-y^0)\Sigma^{\rho}_{ab}(x,y)\\ M^2_{ab}(x) &= m^2 + \Sigma^{(0)}_{ab}(x)\end{aligned} \tag{2.24}$$

Large-N expansion of the 2PI effective action

As already stated, we do not have a closed from of Γ_2 for interacting theories and therefor we need a sensible approximation. Due to the scaling, $S \sim N$, of the classical action, one can expand the 2PI effective action Γ_2 in orders of $1/N$. This is the well established large-N expansion, which has been frequently used in both equilibrium and nonequilibrium and is known to produce qualitatively correct results [48]. Classifying the terms in the effective action according to their scaling with the number N of field components. Using that $\mathrm{tr}_{\mathcal{C}}$ involves also the trace over the field component index, we can easily deduce the scaling of the one-loop terms in Eq. (2.15):

$$\begin{aligned}&i\,\mathrm{tr}_{\mathcal{C}}\log G^{-1} \sim N\\ &i\,\mathrm{tr}_{\mathcal{C}}\, G_0^{-1}G = \underbrace{\mathrm{tr}_{\mathcal{C}}\left[-(\Box+m^2)G\right]}_{\sim N} + \underbrace{\frac{\lambda}{3!N}\,\mathrm{tr}_{\mathcal{C}}\left[\phi_a\phi_a\right]\mathrm{tr}_{\mathcal{C}}\left[G\right]}_{\sim N} - \underbrace{\frac{\lambda}{3N}\,\mathrm{tr}_{\mathcal{C}}\left[\phi_a\phi_b G_{ab}\right]}_{\sim N^0}\end{aligned} \tag{2.25}$$

Hence the leading order (LO) contributions scale $\sim N$ and the next-to-leading order (NLO) contributions scale $\sim N^0$. For the 2PI effective action we also classify the diagrams obtained from contractions of S_{int} according to their scaling with N. Each vertex is surpressed by a factor N^{-1} and a single loop contributes a factor N. It is clear, that diagrams with more independent summations over field indices scale more favorable with N, in other words products of traces of Green's functions have a higher scaling than traces of products of Green's functions. In the following two subsections, the LO and NLO contributions to Γ_2 are discussed in detail.

Leading order: $\Gamma_2^{(\mathbf{LO})} \sim N$

Part of the text in this section is taken from the following publication of the author:

- **Simon A. Weidinger**, Markus Heyl, Alessandro Silva, Michael Knap, "Dynamical Quantum Phase Transitions in Systems with Continuous Symmetry Breaking", *Phys. Rev. B* **96**, 134313 (2017)

Since contractions of $S_{\text{int}}[\phi, \varphi]$ are not allowed to contain any φ-tadpoles, the cubic vertex gives no contribution at LO, hence the 2PI effective action at leading order depends only on the Green's function. The leading order contribution of the quartic vertex is given by contracting fields with the same index and thus we obtain [48]

$$\Gamma_2^{(\text{LO})}[G] = \quad = \frac{\lambda}{4!N} \int_{x,\mathcal{C}} G_{aa}(x,x) G_{bb}(x,x) \tag{2.26}$$

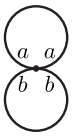

The proper self-energy at LO is hence only a loop consisting of a single Green's function:

$$\begin{aligned} \Sigma_{ab}^{(\text{LO})}(x,y) &= -i\Sigma_{ab}^{(0)}(x)\delta_{\mathcal{C}}(x-y) \\ \Sigma_{ab}^{(0)}(x) &= \frac{\lambda}{6N} G_{aa}(x,x)\delta_{ab} \end{aligned} \tag{2.27}$$

We notice, that the self-energy is a local function in space and time and can thus be completeley absorbed into a time-dependent and possibly position dependent effective mass. In other words the only effect of the interaction is to renormalize the mass/energy gap of excitations, but these renormalzed particles are then non-interacting. Hence at leading order in the large-N approximation we are still dealing with an effectively free field theory. This implies, that the system does not thermalize at leading order.

At leading order, we can also use an equivalent approach to calculate the time evolution of the system, which is based directly on Heisenberg's equations of motion of the field operators. This so called mode function formalism is more simple, as it does not use the notion of the closed-time contour or generating functionals. However, this simplicity comes at the cost of not being generalizable to higher orders in $1/N$.
In the limit of an infinite number of field components, $N \to \infty$, one can factorize the expectation value $\langle \frac{\hat{\Phi}_a \hat{\Phi}_a}{N} \hat{\Phi}_b \rangle = \langle \frac{\hat{\Phi}_a \hat{\Phi}_a}{N} \rangle \langle \hat{\Phi}_b \rangle + \mathcal{O}(1/N)$[50], therefor the only effect of the quartic term is to renormalize the mass-term of the field:

$$m_{\text{eff}}^2 = m^2 + \frac{\lambda}{6N} \langle \hat{\Phi}_a^2 \rangle. \tag{2.28}$$

The Hamiltonian of the model thus becomes effectively quadratic. We will assume that there is a finite vacuum expectation value $\phi(t) = \langle \hat{\Phi}_1(x,t) \rangle$ in the $a = 1$ component. Due to the limit $N \to \infty$, the $a = 1$ component can be in fact considered as a c-number variable, i.e. $\hat{\Phi}_1(t) \to \phi(t) \in \mathbb{R}$, analogously to the zero momentum mode in a mean-field description of the weakly interacting Bose gas. The remaining components, $a \geq 2$, we expand in a plain-wave type fashion in creation and annihilation operators $\hat{b}_p^{(a)\dagger}$, $\hat{b}_p^{(a)}$, which diagonalize the initial Hamiltonian at

$t = 0$:

$$\hat{\Phi}_a(x,t) = V^{-1/2}\sum_p \hat{\Phi}_a(p,t)e^{ipx}$$
$$\hat{\Phi}_{a\geq 2}(p,t) = f_p(t)\hat{b}_p^{(a)} + f_p^*(t)\hat{b}_{-p}^{(a)\dagger}, \tag{2.29}$$

The $f_p(t)$ are the eponymous mode functions. As we've assumed, that the VEV is only finite in the $a = 1$ component, we have a $O(N-1)$ symmetry in the remaining $a \geq 2$ components and hence the mode functions carry no field index.
Now using the effectively quadratic Hamiltonian and the decomposition, Eq. (4.4) of the field operator into mode functions, we can easily obtain the Heisenberg equations of motion at leading order in N:

$$\ddot{f}_p(t) + [p^2 + m_{\text{eff}}^2(t)]f_p(t) = 0$$
$$\ddot{\phi}(t) + m_{\text{eff}}^2(t)\phi(t) = 0, \tag{2.30}$$

where the time-dependent effective mass is given by

$$m_{\text{eff}}^2(t) = m^2 + \frac{\lambda}{6N}\left(\phi^2(t) + (N-1)\int_p |f_p(t)|^2\right). \tag{2.31}$$

Here one should note, that $\phi(t) \sim \sqrt{N}$ and thus both terms in the parenthesis in Eq. (4.6) show a linear scaling with N.
The initial conditions can be deduced from the requirement, that $\hat{b}_p^{(a)\dagger}$, $\hat{b}_p^{(a)}$ diagonalize the Hamiltonian at $t = 0$. This gives $f_p(0) = 1/\sqrt{2\omega_p}$ and $\dot{f}_p(0) = -i\sqrt{\omega_p/2}$, where the dispersion is given by $\omega_p = \sqrt{p^2 + m_{\text{eff}}^2(t=0)}$. In case the system is initially in the symmetry broken phase and the initial effective mass vanishes, $m_{\text{eff}}^2(0) = 0$, then the initial vacuum expectation value is determined by

$$(\phi_0)^2 = -\frac{6r_{\text{i}}^0}{\lambda} - (N-1)\langle\hat{\Phi}_2\hat{\Phi}_2\rangle. \tag{2.32}$$

Otherwise, if the system is in the symmetry broken state and the initial effective mass is finite, we have $\phi_0 = 0$. The first time derivative is zero in any case $\dot{\phi}_0 = 0$. This also implies, that if one starts with a vanishing vacuum expectation, it will remain so for all times. Physically this is due to the $O(N)$-symmetry of the model.

Next-to-leading order: $\Gamma_2^{(\text{NLO})} \sim N^0$

The diagrams contributing at NLO fall in two classes, one without the VEV ϕ and one containing the VEV. Here we note, that even though we will not consider the NLO time evolution of the field expectation value in the following chapters, it turns out that taking into account the VEV is helpful in the resummation of the

next-leading-order diagrams. Both classes contain infinitely many diagrams, but can be resummed in a closed form yielding integral equations. We can write

$$\Gamma_2^{(\mathrm{NLO})}[\phi, G] = \Gamma_2^{\mathrm{ring},1}[G] + \Gamma_2^{\mathrm{ring},2}[\phi, G]. \tag{2.33}$$

The diagrams in $\Gamma_2^{\mathrm{ring},1}$, containing no VEV, are generated by the quartic term in S_{int} and are a sum of polarization-bubbles, $\Pi_{ab}(x,y) = G_{ab}(x,y)G_{ba}(y,x)$, arranged in rings [48]:

$\Gamma_2^{\mathrm{ring},1} =$ 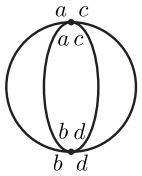 $+\frac{1}{3}$ 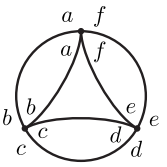 $+\frac{1}{4}$ 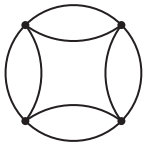 $+\ldots$ (2.34)

The series is just the Taylor-expansion of the logarithm, therefor

$$\begin{aligned}\Gamma_2^{\mathrm{ring},1}[G] &= \frac{i}{2}\mathrm{tr}_{\mathcal{C}} \log \mathrm{B(G)} \\ B_{ab}(x,y;G) &= \delta_{\mathcal{C}}(x-y) + \frac{i\lambda}{6N} G_{ab}(x,y)G_{ab}(x,y).\end{aligned} \tag{2.35}$$

The second class of diagrams $\Gamma_2^{\mathrm{ring},2}$, containing also the VEV, can be summed as

$$\Gamma_2^{\mathrm{ring},2}[\phi, G] = \frac{i\lambda}{6N} \int_{x,y,\mathcal{C}} \phi_a(x) G_{ab}(x,y) \phi_b(y) I(x,y;G), \tag{2.36}$$

where $I(G)$ is the sum of "bubble-chains" which obeys the Bethe-Salpeter like equation

$$I(x,y;G) = \frac{\lambda}{6N} G_{ab}(x,y)G_{ab}(x,y) - \frac{i\lambda}{6N} \int_{z,\mathcal{C}} I(x,y;G) G_{ab}(z,y)G_{ab}(z,y). \tag{2.37}$$

One can show easily, that $B(G)$ and $I(G)$ obey the relation

$$B^{-1}(x,y;G) = \delta_{\mathcal{C}}(x-y) - iI(x,y;G), \tag{2.38}$$

which will enable us to write down an expression for the selfenergy. Now we turn to the self-energy at NLO. Assuming that $\phi = 0$, only $\Gamma_2^{\mathrm{ring},1}$ is relevant and by calculating the functional derivative with respect to G we obtain [48]

$$\Sigma_{ab}^{(\mathrm{NLO})}(x,y) = -\frac{i\lambda}{3N} \delta_{\mathcal{C}}(x-y) G_{ab}(x,x) - \frac{\lambda}{3N} I(x,y;G) G_{ab}(x,y). \tag{2.39}$$

The first term in Eq. (2.39) is local and will just give a further renormalization of the effective mass. The second term however is nonlocal and incorporates interactions of the renormalized excitations, which go beyond a simple renormalization of coupling constants and the theory is now a truely interaction one. As we will

see shortly this leads to memory effects in the quantum evolution equations and we can expect new non-trivial effects at NLO.
Finally we decompose Eq.'s (2.39) and (2.37) into statistical and spectral parts, analogously to the Green's function in Eq. (2.22) and make the contour integrations explicit [48]:

$$\begin{aligned}\Sigma^{F,\mathrm{NLO}}(x,y) &= -\frac{\lambda}{3N}\left(F(x,y)I_F(x,y) - \frac{1}{4}\rho(x,y)I_\rho(x,y)\right)\\ \Sigma^{\rho,\mathrm{NLO}}(x,y) &= -\frac{\lambda}{3N}\left(F(x,y)I_\rho(x,y) + \rho(x,y)I_F(x,y)\right)\end{aligned} \tag{2.40}$$

$$\begin{aligned}\Pi_F(x,y) &= \frac{\lambda}{6}\left(F(x,y)F(x,y) - \frac{1}{4}\rho(x,y)\rho(x,y)\right)\\ \Pi_\rho(x,y) &= \frac{\lambda}{3}F(x,y)\rho(x,y)\end{aligned} \tag{2.41}$$

$$\begin{aligned}I_F(x,y) &= \Pi_F(x,y) - \int_0^{x^0} dz I_\rho(x,z)\Pi_F(z,y) + \int_0^{y^0} dz I_F(x,z)\Pi_\rho(z,y)\\ I_\rho(x,y) &= \Pi_\rho(x,y) - \int_{y^0}^{x^0} dz I_\rho(x,z)\Pi_\rho(z,y)\end{aligned} \tag{2.42}$$

Here we have also used the fact that for vanishing vacuum expectation value, we have $G_{ab}(x,y) = \delta_{ab}G(x,y)$ due to the $O(N)$-symmetry. Eq.'s (2.40), (2.41), (2.42) together with the Kadanoff-Baym equations, Eq. (2.23) now form a closed set of equations, which upon specifying the initial conditions for the statistical and spectral parts of the Green's function enable us to calculate the time evolution of $F_{ab}(x,y)$ and $\rho_{ab}(x,y)$. Of course, Eq. (2.23) cannot be solved analytically and one has to resort to numerical methods.
For the relativistic scalar field a simple leap-frog algorithm appears to yield satisfying results, due to the equation being second order in time. The time-space is discretized on an equidistant grid, $(t,t') \to (n\Delta t, m\Delta t)$.
The second-order time derivative is replaced by the combination of forward- and backward difference, e.g.

$$\partial_t^2 F(t,t') \to \frac{1}{\Delta t^2}\left[F(n+1,m) + F(n-1,m) - 2F(n,m)\right], \tag{2.43}$$

and time integrals are calculated with the trapezoidal rule, e.g.

$$\int_0^t d\tau\, F(\tau,t') \to \Delta t\left[\frac{F(0,m)+F(n,m)}{2} + \sum_{l=1}^{n-1} F(l,m)\right]. \tag{2.44}$$

Upon using these discretization rules for Eq.'s (2.23), (2.40), (2.41), (2.42), one obtains explicit equations for $F(n+1,m)$, $\rho(n+1,m)$ for $m \leq n$, which, together with the symmetry properties of F and ρ, are sufficient to propagate the initial conditions.

2.3 Lattice Fermions

As a second example for the application of the 2PI Keldysh formalism, we look at spin-less fermions on a d-dimensional lattice, with a nearest neighbor hopping J, density-density interactions U_{ij} and subject to a local onsite potential h_j,

$$\hat{H} = -J \sum_{\langle i,j \rangle} \hat{c}_i^\dagger \hat{c}_j + \sum_{i,j} U_{ij} \hat{n}_i \hat{n}_j + \sum_j h_j \hat{n}_j. \tag{2.45}$$

The Hamiltonian, Eq. 2.45, is just a generalization of the ubiquitous Hubbard model of spin-less fermions. Later on we will restrict ourselves to nearest-neighbor interactions, but as it does not complicate the discussion much, we will keep the structure of the interaction unspecified for now. To simplify notation, we introduce the one-body matrix $-\hat{J}_{ij} = \delta_{\langle i,j \rangle} + h_i \delta_{ij}$, with which we can write the Hamiltonian as

$$\hat{H} = \sum_{i,j} (-\hat{J}_{ij} \hat{c}_i^\dagger \hat{c}_j + U_{ij} \hat{n}_i \hat{n}_j). \tag{2.46}$$

In order to build a field-theoretic description, we trade operators for anticommuting Grassmann fields, originating from the standard coherent state path integral for fermions and write down the action corresponding to Eq. (2.46),

$$S[\bar{c}, c] = \int_{\mathcal{C}} dt \sum_{i,j} \left\{ \bar{c}_i (i\partial_t + \hat{J}_{ij}) c_j - U_{ij} \bar{c}_i \bar{c}_j c_j c_i \right\}. \tag{2.47}$$

As detailed in the last section for bosons, we follow the procedure of introducing sources for the fermion fields and the Green's function and performing a Legendre transformation such that we have a parametrization directly in terms of the full Green's function. Despite the fact, that the sources are now Grassmann fields and that the path integrals is fermionic there is no technical difference in the derivation, hence we give directly the result for the effective action:

$$\Gamma[G] = -i \operatorname{tr} \log G^{-1} - i \operatorname{tr} G_0^{-1} G + \Gamma_2[G]. \tag{2.48}$$

In a fermionic model, such as Eq. (2.46), the effective action $\Gamma[G]$ and hence the 2PI effective action $\Gamma_2[G]$ only depends on the Green's function, as fermions cannot condense due to the Pauli principle. The 2PI effective action is given by the sum of all two-particle irreducible diagrams of the interaction vertex

$$S_{\text{int}}[\bar{c}, c] = \int_{\mathcal{C}} dt \sum_{i,j} U_{ij} \bar{c}_i \bar{c}_j c_j c_i \tag{2.49}$$

and the bare Green's function is

$$G_{0,ij}^{-1}(t,t') = \delta_{\mathcal{C}}(t,t')(i\delta_{ij}\partial_t + \hat{J}_{ij}). \tag{2.50}$$

By requiring, that the effective action is stationary with respect to the Green's function, we obtain the Dyson equation for fermions,

$$\begin{aligned} G_{ij}^{-1}(t,t') &= G_{0,ij}^{-1}(t,t') - \Sigma_{ij}(t,t') \\ \Sigma_{ij}(t,t') &= -i\frac{\Gamma_2[G]}{\delta G_{ji}(t',t)}. \end{aligned} \tag{2.51}$$

Eq. (2.51) is again defined on the closed time Keldysh contour and in the following we will make the contour explicit.

Kadanoff-Baym equations

Rewriting the Dyson equation, Eq. (2.51) as an integral equation we get

$$(i\partial_t + \hat{J}) * \hat{G}(t,t') = \delta_{\mathcal{C}}(t,t')\hat{\mathbb{1}} + \int_{\mathcal{C}} dt''\, \hat{\Sigma}(t,t'') * \hat{G}(t'',t'), \tag{2.52}$$

where we introduced a matrix notation in the spatial indices, $(\hat{G}(t,t'))_{ij} = G_{ij}(t,t')$, $(\hat{\Sigma} * \hat{G})_{ij} = \sum_l \Sigma_{il} G_{lj}$, to keep notation short.
To make the contour integration explicit we first introduce greater and lesser Green's functions,

$$\begin{aligned} G_{ij}^{>}(t,t') &= -i\langle \hat{c}_i(t)\hat{c}_j^{\dagger}(t')\rangle \\ G_{ij}^{<}(t,t') &= i\langle \hat{c}_j^{\dagger}(t')\hat{c}_i(t)\rangle. \end{aligned} \tag{2.53}$$

In terms of $G^{>}$ and $G^{<}$ the contour ordered Green's function G is written as

$$G_{ij}(t,t') = \Theta_{\mathcal{C}}(t,t')G_{ij}^{>}(t,t') + \Theta_{\mathcal{C}}(t',t)G_{ij}^{<}(t,t'), \tag{2.54}$$

where $\Theta_{\mathcal{C}}(t,t')$ is the closed time contour Heaviside theta function, which is 1 if t' comes before t on the closed time contour and zero otherwise. Similarly we can also express the retarded and advanced Green's functions, G^{R} and G^{A} in terms of $G^{\lessgtr}$:

$$\begin{aligned} G_{ij}^{\mathrm{R}}(t,t') &= -i\Theta(t-t')\langle\{\hat{c}_i(t),\hat{c}_j^{\dagger}(t')\}\rangle = \Theta(t-t')[G_{ij}^{>}(t,t') - G_{ij}^{<}(t,t')] \\ G_{ij}^{\mathrm{A}}(t,t') &= i\Theta(t'-t)\langle\{\hat{c}_i(t),\hat{c}_j^{\dagger}(t')\}\rangle = \Theta(t'-t)[G_{ij}^{<}(t,t') - G_{ij}^{>}(t,t')] \end{aligned} \tag{2.55}$$

The selfenergy $\Sigma(t,t')$ can be also split into greater/lesser components upon we have subtracted a possible time local term:

$$\begin{aligned} \Sigma_{ij}(t,t') &= \delta_{\mathcal{C}}(t,t')\Sigma_{ij}^{\mathrm{HF}}(t) + \bar{\Sigma}_{ij}(t,t') \\ \bar{\Sigma}_{ij}(t,t') &= \Theta_{\mathcal{C}}(t,t')\Sigma_{ij}^{>}(t,t') + \Theta_{\mathcal{C}}(t',t)\Sigma_{ij}^{<}(t,t') \end{aligned} \tag{2.56}$$

The time local part of the selfenergy, $\Sigma^{\mathrm{HF}}(t)$ will turn out to correspond to Hartree-Fock diagrams.
Inserting the decompositions of $G(t,t')$ and $\Sigma(t,t')$ into greater and lesser parts, Eq's. (2.54) and (2.56), into the Dyson equation, Eq. (2.52), explicitly writing out the time integral over the closed time contour using the so called Langreth rules [55], we obtain the Kadanoff-Baym equations for the time evolution of the greater and lesser Green's functions in our lattice fermion model:

$$\begin{aligned}(i\partial_t + \hat{J} - \Sigma^{\mathrm{HF}}(t)) * \hat{G}^{\lessgtr}(t,t') &= I_L^{\lessgtr}(t,t') \\ \hat{G}^{\lessgtr}(t,t') * (-i\overleftarrow{\partial_{t'}} + \hat{J} - \Sigma^{\mathrm{HF}}(t')) &= I_R^{\lessgtr}(t,t'),\end{aligned} \tag{2.57}$$

where

$$\begin{aligned}I_L^{\lessgtr}(t,t') &= \int_0^t dt''\, \Sigma^{\mathrm{R}}(t,t'') * G^{\lessgtr}(t'',t') + \int_0^{t'} dt''\, \Sigma^{\lessgtr}(t,t'') * G^{\mathrm{A}}(t'',t') \\ I_R^{\lessgtr}(t,t') &= \int_0^t dt''\, G^{\mathrm{R}}(t,t'') * \Sigma^{\lessgtr}(t'',t') + \int_0^{t'} dt''\, G^{\lessgtr}(t,t'') * \Sigma^{\mathrm{A}}(t'',t').\end{aligned} \tag{2.58}$$

The equations of motion, Eq. (2.57), have to be solved numerically. In order not to lose the unitary and conserving nature of the Kadanoff-Baym equations an integration with the trapezoidal rule in conjunction with a predictor-corrector scheme is necessary. The time-space is discretized as in Sec. 2.2, $(t,t') \to (n\Delta t, m\Delta t)$ and Eq. (2.57) is integrated with the trapezoidal rule from $t = T$ to $t = T + \Delta$, which, for example, gives

$$\begin{aligned}G^{\lessgtr}(T+\Delta t,t') =& G^{\lessgtr}(T,t') + \frac{i\Delta t}{2}\Big[(\hat{J} - \Sigma^{\mathrm{HF}}(T+\Delta t)) * G^{\lessgtr}(T+\Delta t,t') \\ &- I_L^{\lessgtr}(T+\Delta,t') + (\hat{J} - \Sigma^{\mathrm{HF}}(T)) * G^{\lessgtr}(T,t') - I_L^{\lessgtr}(T,t')\Big].\end{aligned} \tag{2.59}$$

Eq. (2.59) is an implicit equation for $G^{\lessgtr}(T+\Delta t,t')$, which is solved using a predictor-corrector scheme: First, in the *prediction*-step, a predictor $G_p^{\lessgtr}(T+\Delta t,t')$ is calculated by replacing all $T+\Delta t$ with T on the right hand side of Eq. (2.59) and from this then also a predictor for $I_L^{\lessgtr}(T+\Delta,t')$ is obtained. Second, in the *correction*-step, we calculate a corrected $G_c^{\lessgtr}(T+\Delta t,t')$, by using the predictor Green's functions and predictor memory integrals on the right hand side of Eq. (2.59). This two-step process is then iterated until the predictor and corrector Green's functions, $G_p^{\lessgtr}(T+\Delta t,t')$ and $G_c^{\lessgtr}(T+\Delta t,t')$ respectively, agree within a certain accuracy.

Weak coupling expansion of the 2PI effective action

We will now assume, that density-density interaction U is small such that it is possible to expand the 2PI effective action $\Gamma_2[G]$ in powers of U. Diagrammatically

this means, that we organize diagrams according to the number of interaction vertices, U_{ij}, appearing. The expansion will be performed up to second order in U. We can write

$$\Gamma_2[G] = \Gamma_2^{\mathrm{H}}[G] + \Gamma_2^{\mathrm{F}}[G] + \Gamma_2^{\mathrm{SCB}}[G] + \Gamma_2^{\mathrm{Cross}}[G] + \mathcal{O}(U^3). \tag{2.60}$$

The first two terms, $\Gamma_2^{\mathrm{H}}[G]$ and $\Gamma_2^{\mathrm{F}}[G]$, comprise the Hartree-Fock approximation, which will give rise to the time local part of the selfenergy and is of order U. The third term, commonly referred to as self-consistent Born approximation, and the fourth term, which we will call cross approximation, are of order U^2 and are time nonlocal, such that they give rise to memory integrals on the right hand side of the Kadanoff-Baym equations, Eq. (2.57).
The Hartree diagram is

$\Gamma_2^{\mathrm{H}}[G] =$ 

$= \sum_{ij} U_{ij} \int_{\mathcal{C}} dt\; G_{ii}(t,t) G_{ii}(t,t).$ (2.61)

The Fock diagram is

$\Gamma_2^{\mathrm{F}}[G] =$ 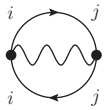

$= -\sum_{ij} U_{ij} \int_{\mathcal{C}} dt\; G_{ij}(t,t) G_{ji}(t,t).$ (2.62)

The self-consistent Born diagram is

$\Gamma_2^{\mathrm{SCB}}[G] =$ 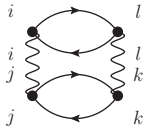

$$= 2i \sum_{ijkl} U_{ij} U_{kl} \int_{\mathcal{C}} dt\; dt'\; G_{il}(t,t') G_{li}(t',t) G_{jk}(t,t') G_{kj}(t',t). \tag{2.63}$$

The cross diagram is

$\Gamma_2^{\mathrm{Cross}}[G] =$ 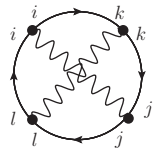

$$= -2i \sum_{ijkl} U_{ij} U_{kl} \int_{\mathcal{C}} dt\; dt'\; G_{ik}(t,t') G_{kj}(t',t) G_{jl}(t,t') G_{li}(t',t). \tag{2.64}$$

Calculating the functional derivative of the Hartree and Fock terms with respect to the Green's function, we obtain the Hartree-Fock selfenergy

$$\Sigma_{ij}^{\mathrm{HF}}(t) = \quad + \quad = -2i\delta_{ij}\sum_{l} U_{il}G_{ll}(t,t) + 2iU_{ij}G_{ij}(t,t), \quad (2.65)$$

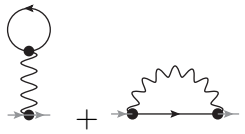

where the first term is the Hartree self-energy and the second part the Fock self-energy. For the SCB and Cross self-energy we get

$$\Sigma_{ij}^{\mathrm{SCB}}(t,t') = \quad = 8G_{ij}(t,t')\sum_{lk} U_{ik}U_{lj}G_{kl}(t,t')G_{kl}(t',t) \quad (2.66)$$

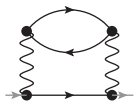

and

$$\Sigma_{ij}^{\mathrm{Cross}}(t,t') = \quad = -8\sum_{lk} U_{ik}U_{lj}G_{il}(t,t')G_{lk}(t',t)G_{kj}(t,t'). \quad (2.67)$$

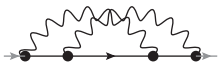

Finally, we decompose these self-energy contribution into greater and lesser parts,

$$\begin{aligned}
\Sigma_{ij}^{\mathrm{HF}}(t) &= -2i\delta_{ij}\sum_{l} U_{il}G_{ll}^{<}(t,t) + 2iU_{ij}G_{ij}^{<}(t,t) \\
\Sigma_{ij}^{\mathrm{SCB},\lessgtr}(t,t') &= 8G_{ij}^{\lessgtr}(t,t')\sum_{lk} U_{ik}U_{lj}G_{kl}^{\gtrless}(t,t')G_{kl}^{\lessgtr}(t',t) \\
\Sigma_{ij}^{\mathrm{Cross},\lessgtr}(t,t') &= -8\sum_{lk} U_{ik}U_{lj}G_{il}^{\lessgtr}(t,t')G_{lk}^{\gtrless}(t',t)G_{kj}^{\lessgtr}(t,t'). \quad (2.68)
\end{aligned}$$

Here a short note on the handling of equal time Green's functions in the diagrammatics is in order, as the contour ordered Green's function $G(t,t')$ is singular for $t = t'$. In the derivation of the coherent state path integral, one starts out with a normal ordered Hamiltonian, i.e. all creation operators standing to left of all annihilation operators. This implies, that creation operators are always evaluated on a coherent state at an infinitesimally later time, hence, to be precise, we should write the interaction vertex as $\bar{c}_i(t+0^+)\bar{c}_j(t+0^+)c_j(t)c_i(t)$. Consequently all equal time Green's functions in the Feynman diagrams for the 2PI effective action or the self-energy are evaluated at $(t, t+0^+)$ and thus we have $G(t,t) = G^{<}(t,t)$.

Chapter 3

Floquet prethermalization and regimes of heating in a periodically driven, interacting quantum system

The text and figures in this chapter are taken from the following publication of the author:

- **Simon A. Weidinger**, Michael Knap, "Floquet prethermalization and regimes of heating in a periodically driven, interacting quantum system", *Scientific Reports* **7**, 45382 (2017)

In order to provide a structure better suited to this thesis, certain sections have been merged and rearranged or renamed.

3.1 Thermalization in a periodically driven system

Periodically driving quantum many-body systems often leads to exotic phenomena that are absent in their undriven counterparts. The unitary quantum evolution of a periodically driven system at times that are commensurate with the drive period T is governed by the operator $\hat{U}(T) = \exp[-i\hat{H}_F T]$, which defines the Floquet Hamiltonian $\hat{H}_F$. The Floquet Hamiltonian $\hat{H}_F$ can be designed in such a way that it hosts novel and exotic phases of matter. Examples include, topologically non-trivial band structures realized by driving topologically trivial systems [56, 57, 58, 59, 60, 61, 62], and ergodic phases created by driving non-ergodic quantum systems [63, 64, 65, 66, 67, 68, 69]. Moreover, phases in periodically driven systems with no direct equilibrium analogue have been proposed [13, 14, 15, 16, 17, 18, 19, 20, 21, 22, 23], including Floquet time crystals which exhibit persistent macroscopic oscillations at integer multiples of the driving period [13, 16, 20, 21, 22, 23].
The eigenstate thermalization hypothesis (ETH) suggests that generic interacting many-body systems heat up to infinite temperature [70, 71], thus inhibiting the realization of such novel phases. A possible resolution is to stabilize the Floquet states by disorder such that the system becomes many-body localized and ETH does not apply [63, 64, 65, 68], as recently demonstrated experimentally [69]. However, this restricts the variety of accessible phases. Another route would be to resort to driving frequencies much higher than all other microscopic scales [72, 73, 74, 75]. But in that case $\hat{H}_{\mathrm{F}}$ becomes quasi-local and cannot possess any exotic phases. A

more general approach, is to resort to a transient *prethermal* regime [76, 77, 78, 79], which is characterized by the interaction time scale of the Floquet Hamiltonian required to realize exotic phenomena being much shorter than the heating timescale. It is therefore eminent to study the stability of such a Floquet prethermal regime in a general context.

In this work, we investigate the stability of the Floquet prethermal regime and the thermalization time scales in a generic interacting many-body system subject to a periodic drive. In particular, we focus on the quantum $O(N)$-model with modulated mass. To this end, we employ the 2-particle irreducible (2PI) effective action approach on the closed Keldysh contour including corrections up to next-to-leading order (NLO) in $1/N$ which allow the system to thermalize. The $O(N)$-model is a well established model for interacting many-body systems, both in condensed matter and cosmology [80, 81, 82, 83, 84, 85, 86, 87, 88, 89, 78]. In particular, the presence of nontrivial interactions at NLO as well as the bosonic nature of excitations render the $O(N)$-model useful for studying heating of a driven many-body system to infinite temperature. Based on our numerical simulations, we find a parametrically large regime of Floquet prethermalization, even when the driving frequency is comparable to other microscopic scales of the undriven Hamiltonian so long as the interactions of the system are not too strong; Fig. 3.1.

We study the quantum $O(N)$-model of N real scalar fields Φ_a, $a = 1, \ldots, N$ with the action [50]

$$S = \int_{x,\mathcal{C}} \left[\frac{1}{2}(\partial_\mu \Phi_a)^2 - \frac{1}{2} m^2(t) \Phi_a^2 - \frac{\lambda}{4!N} (\Phi_a \Phi_a)^2 \right]. \tag{3.1}$$

We use the abbreviation $\int_{x,\mathcal{C}} = \int d^d x \int_{\mathcal{C}} dt$, where the time integration runs over the closed-time Keldysh contour $\mathcal{C}$. Furthermore we assume that repeated indices are summed over. In momentum space a finite cut-off Λ is applied to regularize eventual UV divergencies. Consequently, we are effectively discussing a lattice system with a finite quasi-particle bandwidth. The bare mass $m^2(t) = m_0^2 - A\cos(\Omega t)$ is driven with amplitude A and frequency Ω, which, in a linear response regime ($A \ll \Omega, m_0$) creates pairs of excitations.

It is convenient to rescale time $t \to 2t/\Omega$ and the fields $\Phi_a \to (2/\Omega)^{1/2} \Phi_a$, and to introduce the effective coupling constants in the presence of an external drive:

$$g = \frac{2A}{\Omega^2}, \qquad u = \frac{8\lambda}{\Omega^3}. \tag{3.2}$$

The driving amplitude is rescaled by Ω^2, which is a consequence of the relativistic form of the action. The model (3.1) displays an equilibrium phase transition to an ordered, symmetry broken phase for $m_0^2 < 0$ and small $\lambda < \lambda_c$ at low temperatures. The drive destroys the ordered phase already at leading order in $1/N$ [78]. Hence, as we are interested in the long-time dynamics, we restrict ourselves to initial states in the symmetric phase. Furthermore, in the case of symmetric initial states, we find the same qualitative behavior in all spatial dimensions $d = 1, 2, 3$, and thus

the presented results focus on $d = 1$. We emphasize that our results represent the thermodynamic limit, and thus should be contrasted to the exact diagonalization of small systems.

In order to simulate the dynamics of the driven system, we use the nonequilibrium Keldysh formalism [90]. The time evolution of the two-point contour ordered Green's function $\hat{G}$ is governed by the self-consistent Dyson equation

$$\left(\Box_{t,x} + m^2(t)\right)\hat{G}(t,t') + i\int_{\mathcal{C}} dt''\hat{\Sigma}(t,t'') * \hat{G}(t'',t') = -i\hat{\mathbb{1}}\delta_{\mathcal{C}}(t-t'), \quad (3.3)$$

where $\Box_{t,x}$ is the d'Alembert operator and the self-energy $\hat{\Sigma}$ is given as the functional derivative of the 2PI effective action Γ_2 [47], see the methods section for details. The advantages of this approach are that it operates in the thermodynamic limit and respects the conservation laws associated with the global symmetries of the microscopic action, such as energy or momentum conservation. We decompose the contour ordered Green's function as $\hat{G}(t,t') = \hat{F}(t,t') - i/2\mathrm{sgn}_{\mathcal{C}}(t-t')\hat{\rho}(t,t')$, with the Keldysh or statistical correlation function $\hat{F}$, that is symmetric under a permutation of arguments, and the spectral function $\hat{\rho}$, that is antisymmetric when permuting the arguments.

We employ a $1/N$ fluctuation expansion to the real-time effective action Γ_2 to next-to-leading order (NLO) [48, 49]. While in the symmetric phase only a single diagram contributes at leading-order (LO), at NLO an infinite series of diagrams has to be summed. The self-energy up to NLO can be schematically represented by the following diagrammatic series

$\Sigma =$ 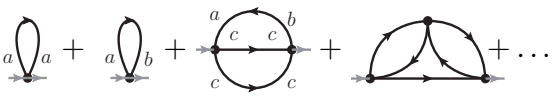 $+ \ldots$ (3.4)

where lines represent full Green's functions G and dots vertices, each of which comes with a factor $\sim \lambda/N$. In this scheme, the LO (first diagram) is equivalent to a self-consistent Hartree-Fock approximation and thus results in a time-local self-energy that solely renormalizes the bare mass; see methods section. A LO analysis is thus not sufficient to answer the question of whether a prethermal state can be stabilized, as it eliminates the possibility of infinite heating from the beginning. Only at NLO [all other diagrams in Eq. (3.4)] the self-energy contains parts which are non-local in time and lead to scattering and memory effects that ultimately enable thermalization.

The NLO evolution equations are integrated numerically for times up to $3.18 \cdot 10^4$ driving cycles. The momentum cutoff is set to $\Lambda = \pi$. As initial condition we use the LO groundstate of the $O(N)$-model for given interaction u and fixed renormalized mass $m^2_{\mathrm{eff}} = 1$, i.e. the bare mass m_0^2 gets adjusted accordingly. We have chosen this convention, since the physically relevant observable quantity is the renormalized mass m^2_{eff}, which has to be fixed to get comparable results. Furthermore, we set the drive amplitude to $g = 1/4$ and scan the interaction u and drive frequency Ω.

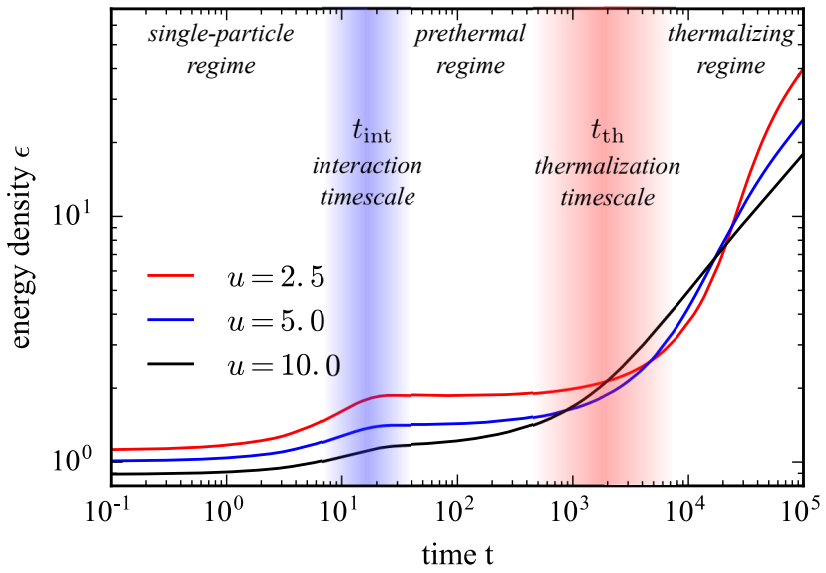

Figure 3.1: **Time evolution of the energy density in the periodically driven $O(N)$ model.** The energy density $\epsilon(t)$ exhibits three distinct dynamical regimes: (I) At short times t, single-particle rearrangements lead to a fast increase of the energy density, up to times t_{int} at which interactions become relevant. (II) At intermediate times, $t_{\mathrm{int}} < t < t_{\mathrm{th}}$, a stable Floquet prethermal regime occurs in which the interacting system ceases to absorb. (III) At late times, beyond the thermalization time scale $t > t_{\mathrm{th}}$, interactions between a large number of generated quasi-particle excitations cause strong heating. In that regime, the energy density displays an algebraic growth, $\epsilon(t) \sim t^{\alpha}$, with an exponent that approaches $\alpha \sim 1/2$ for strong interactions. The data is shown for drive frequency $\Omega = 2.3$ and for three different values of the interaction strength u, see legend.

3.2 Dynamics of the energy density

The central observable to study heating in any driven system is the energy density $\epsilon(t) = \langle \hat{H}(t) \rangle / V$, where V is the system volume. In our scheme the expectation value of the Hamiltonian is directly available from the Keldysh Green's function F. Calculating the expectation of the quadratic part of the Hamiltonian is straightforward, whereas for the quartic term, we use Heisenberg's equations of motion to express it in terms of higher order time derivatives of the Keldysh Green's function. We obtain

$$\epsilon(t) = \frac{N}{4} \int_p \left(2\partial_t \partial_t' - \partial_t^2 + \frac{4\left(p^2 + m_0^2\right)}{\Omega^2} \right) F(t, t', p)|_{t=t'}. \tag{3.5}$$

Typical plots of $\epsilon(t)$ are shown in Fig. 3.1. We can divide the heating of the system into three regimes: (I) At short times, up to the interaction timescale t_{int}, the

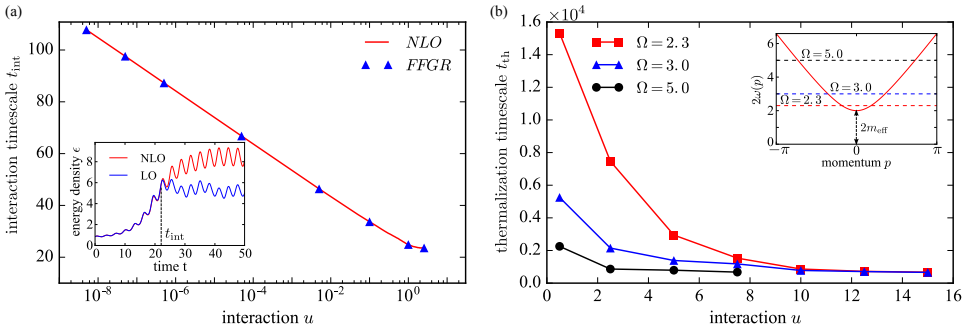

Figure 3.2: **Parametric dependence of the interaction and thermalization time scales.** (a) Interaction times scale t_{int} as a function of the interaction strength u. In the limit of weak interactions, $u \lesssim 1$, the interaction time t_{int} scales logarithmically with u. This behavior can be analytically understood from a calculation based on Floquet Fermi's Golden Rule (FFGR), symbols, which perfectly agrees with the numerically evaluated interaction time scale, solid line. For $u \gtrsim 1$, t_{int} is not well defined, as interaction effects matter as soon as the drive is switched on. The inset illustrates the definition of t_{int} by comparing the time evolution of the energy density using leading order (LO) and next-to-leading order (NLO) approximations. At LO the heating stops at t_{int} while at NLO the system very slowly absorbs energy from the drive and enters the Floquet prethermalization regime. (b) Thermalization timescale t_{th} as a function of the interaction strength u. The thermalization time scale t_{th} characterizes the crossover between the prethermal and the heating regime. It depends strongly on both the interactions u and drive frequency Ω. Inset: The driving frequencies Ω (dashed lines) lie within the initial bandwidth of quasi-particle pairs (solid line).

dynamics is dominated by single-particle rearrangements, leading to exponentially fast heating. In that regime, a LO approximation is sufficient to describe the dynamics and scattering of quasi-particles is essentially irrelevant. We define, the interaction timescale t_{int} as the time at which the LO and NLO results starts to deviate, which characterizes the time at which non-local contributions to the self-energy become important. (II) After this initial stage of heating, the system quickly enters a prethermal plateau with low absorption. This Floquet prethermal state persists up to the thermalization time t_{th} and can span several decades in time, thus providing a solid regime for Floquet engineering. (III) At late times $t \gtrsim t_{\mathrm{th}}$ heating becomes significant and we expect the system to approach the infinite temperature state. In that regime our data suggests a power-law growth of the energy density $\epsilon(t) \sim t^{\alpha}$. In the following, we discuss these regimes and where possible provide analytical arguments for the observed behavior.

3.3 Three dynamical regimes on the way to thermalization

Short time dynamics

At short times, NLO corrections are essentially irrelevant for the dynamics, as confirmed explicitly by comparing LO and NLO results; inset in Fig. 3.2 (a). At LO, the system is equivalent to a multi-dimensional anharmonic oscillator with periodically modulated frequencies (see details in the methods section). We can understand the dynamics in terms of a parametric resonance with the resonance condition set by $\Omega = 2\omega(p^\star)$, where $\omega(p) = (p^2 + m_{\text{eff}}^2)^{1/2}$ is the initial dispersion relation of excitations. The momentum-mode $p^\star$ grows exponentially and the fastest growing observable will be $F(t,t,p^\star) \sim e^{2\gamma_{p^\star} t}$. Consequently, using (3.5), the energy density will also grow exponentially in time $\epsilon(t) \sim e^{2\gamma_{p^\star} t}$. In the Gaussian limit, $u = 0$, this exponential growth would last indefinitely, but for finite u the self-consistently determined effective mass grows simultaneously with $F(t,t,p^\star)$, breaking the resonance condition at a certain time, and preventing any further energy-absorption in a LO approximation [78]. Note that since we fix the initial effective mass, $m_{\text{eff}}^2(t = 0) = 1$, the growth rate γ_p is independent of u. This is due to the fact, that the parametric resonance only depends on the frequency and amplitude of the drive as well as the initial quasi-particle spectrum of the system.

Taking into account NLO corrections quasi-particle excitations interact with each other which will eventually lead to heating. We estimate the validity of the LO calculation by $F(t,t,p^\star) \sim u^{-2/3}$, which determines the time when the first non-trivial diagrammatic contribution [sunset diagram, i.e., third diagram in Eq. (3.4)], becomes relevant [82]. Considering the exponential growth of $F(t,t,p^\star)$, the interaction timescale obeys the scaling $t_{\text{int}} \sim (2\gamma_{p^\star})^{-1} \log u^{-2/3}$. The logarithmic scaling of t_{int} with u is confirmed in Fig. 3.2 (a). Deviations from the logarithmic scaling exist for $u \gtrsim 1$, as in the strong interaction regime NLO processes are important already at initial times, which renders the interaction time scale ill-defined.

In order to validate that the scattering of quasi-particle excitations is the reason for the deviation of the LO and NLO results, we derive a Floquet Fermi's Golden rule (FFGR) [91], which formally considers NLO diagrams with the lowest number of interaction vertices (sunset diagram):

The simplest diagram leading to scattering between quasi-particles is the "sunset" diagram, see Fig. 3.3. This diagrams includes interactions of only two quasi-particles. By contrast, higher loop diagrams would include scattering events of more than two particles. As we discuss in the main text, these higher-order events become relevant only at later times. We obtain the following expression for the FFGR self-energy

$$\Sigma^{(\text{FFGR})}(t,t',p) = -\frac{\lambda}{18N} \int_{k,q} G(t,t',p+q) G(t,t',k) G(t',t,q+l). \qquad (3.6)$$

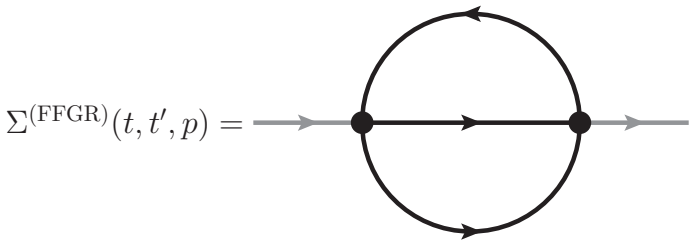

Figure 3.3: **Floquet Fermi's golden rule.** The "sunset" diagram takes into account scattering of two quasi-particles beyond a simple renormalization of the quasi-particle mass. It is non-local in time and leads to memory effects.

Splitting Eq. (3.6) into statistical and spectral components, we obtain

$$\begin{aligned}\Sigma^{F,\mathrm{FFGR}}(t,t',p) &= -\frac{\lambda}{3N}\int_q \left(F(t,t',p+q)\Pi_F(t,t',q) - \frac{1}{4}\rho(t,t',p+q)\Pi_\rho(t,t',q)\right)\\ \Sigma^{\rho,\mathrm{FFGR}}(t,t',p) &= -\frac{\lambda}{3N}\int_q \left(F(t,t',p+q)\Pi_\rho(t,t',q) + \rho(t,t',p+q)\Pi_F(t,t',q)\right).\end{aligned} \tag{3.7}$$

Expressing Σ^{FFGR} in this way, we see that the Floquet Fermi's golden rule analysis amounts to replacing the summation function I in the expression for the NLO self-energy, Eq. (2.40), with the polarization bubble Π.
We find perfect agreement between the interaction time t_{int} evaluated with the full NLO calculation and the FFGR, respectively, which demonstrates that scattering of created excitations is responsible for the deviations between the leading and next-to-leading order time evolution. This explains why the system can heat up further: Once scattering is taken into account, not only pairs of quasi-particles can be created but the energy can also be distributed over many excitations.

Floquet prethermalization

Once the parametric resonance regime is left, heating becomes extremely slow and the prethermal plateau is entered. In that regime the number of quasi-particles is small and hence the multi-particle scattering, which is enabling further energy absorption, is much slower than pair creation. The number of quasi-particle excitations is directly related to the equal time Keldysh Green's function F, which due to the self-consistent feedback continues to grow. As the thermalization timescale t_{th} is reached, the higher order loop diagrams [Eq. (3.4)] that allow for multi-particle scattering start to dominate. Thus, heating becomes significant and the Floquet prethermal state breaks down.
To quantitatively understand the thermalization time scale t_{th}, we study it as a function of the interaction strength u and driving frequency Ω; Fig. 3.2 (b). The

thermalization timescale and thus the lifetime of the prethermal plateau decreases with increasing u, however the functional dependence cannot be described by an exponential or power-law. The dependence is quite strong, with t_{th} changing over one order of magnitude as u varies in the interval $[0.5, 15]$ and $\Omega = 2.3$. Fixing the interaction u, we find that t_{th} decreases with increasing Ω. This is a consequence of all chosen frequencies lying within the initial bandwidth of quasi-particle pairs, $2 < \Omega < 2\sqrt{\Lambda^2 + 1}$, as illustrated in the inset of Fig. 3.2 (b). With increasing Ω, more momentum modes participate in the parametric resonance and consequently the Keldysh component F already ends up being larger as t_{int} is reached; see methods section. Based on our previous arguments on the quasi-particle density, the system thus will be earlier driven out of the prethermal plateau.
Our results do not contradict Refs. [72, 73, 74], which predict that heating is exponentially suppressed at large drive frequencies, as our results are all for small drive frequencies within the two-particle bandwidth. When increasing the drive frequency Ω in our model beyond the two particle bandwidth, the energy absorption becomes very slow. In that case, the system is far away from a parametric resonance and hardly responds to the drive at all.
Even though heating is slow within the prethermal regime $t_{\text{int}} < t < t_{\text{th}}$ it remains finite and the system does not become fully stationary. Nevertheless, in this regime the Green's function only depends extremely weakly on the stroboscopic center-of-mass time $T_n = (t + t')/2 = 2\pi n/\Omega$, where n is an integer. Thus, this extremely slow center-of-mass time dependence should not affect the much faster microscopic processes, that are required to realize novel prethermal states.

Thermalization

At times $t \gtrsim t_{\text{th}}$, the system is driven out of the prethermal regime and the absorption increases. Our numerical simulations suggest that the energy density grows as a powerlaw $\epsilon(t) \sim t^{\alpha}$ (Fig. 3.1), which can persist for several decades. We show the exponent α as a function of the interaction strength u for different driving frequencies Ω in Fig. 3.4. With increasing interaction u and drive frequency Ω the exponent approaches $1/2$, which appears as a lower bound. In the limit of large u and Ω, the thermalization time scale is smallest and hence, given the fixed maximum time that we can reach in our simulations, the accessible thermalization regime is largest for these parameters. This suggests that the powerlaw exponent might slowly creep to the universal value $1/2$ for any interaction u and drive frequency Ω in the asymptotic limit, $t \to \infty$. In contrast, we found linear heating at late times in the $O(N)$-model subject to colored noise; see methods section. Moreover, our results suggest that the driven $O(N)$-model heats to infinite temperature following the well defined prethermal plateau.

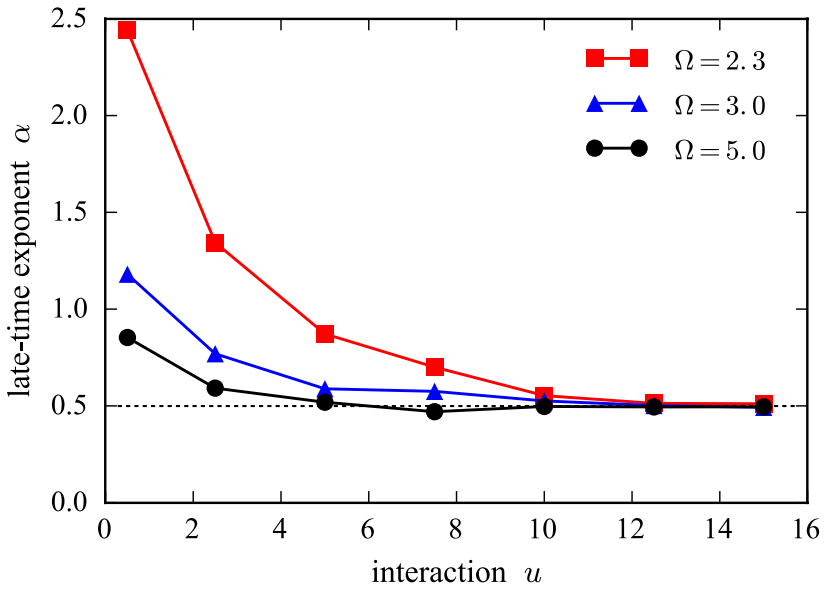

Figure 3.4: **Powerlaw exponent α of the absorbed energy in the thermalizing regime.** The exponent α is extracted from the algebraic growth of the energy density at late times $\epsilon(t) \sim t^{\alpha}$. With increasing interaction strength u and driving frequency Ω (but still within the single-particle band), the exponent α quickly approaches $1/2$, suggesting that in the asymptotic long-time limit, $t \to \infty$, the heating rate universally scales as $\epsilon(t) \sim \sqrt{t}$.

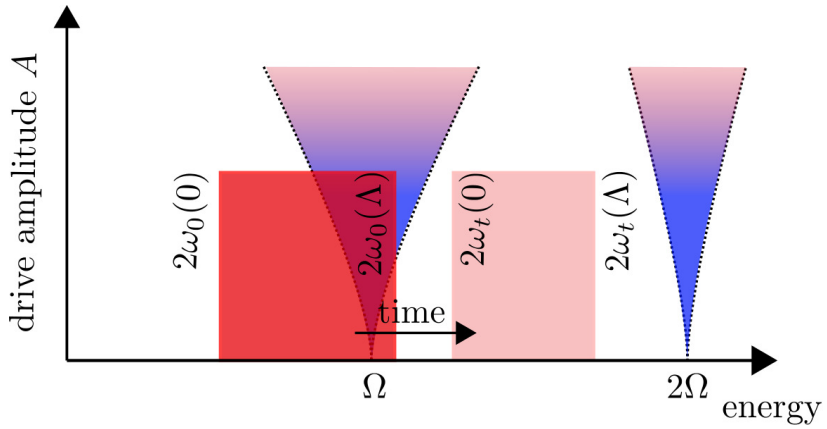

Figure 3.5: **Illustration of the parametric resonance.** When a part of the initial bandwidth (red shaded region) for quasi-particle pairs lies in a parametric resonance (blue shaded regions), the corresponding modes grow exponentially, which leads to an exponentially growth of the effective mass $m_{\text{eff}}(t)$. Accordingly the dispersion relation $\omega_t(p)$ is shifted toward higher energies (light red shaded region). Once the quasi-particle bandwidth lies completely in between to region of parametric resonance, the system stops absorbing energy in the leading order approximation. The parametric resonance at $n\Omega$, $n = 1, 2, \ldots$ is only sharp in the limit of vanishing drive amplitude A and smears out with increasing A. For small A, the width of the resonance grows linearly with A.

3.4 Heating at leading order

To leading order the self-energy is time-local and the evolution equations simplify to

$$\left[\partial_t^2 + p^2 + m_0^2 + A\cos\Omega t + \frac{\lambda}{6}\int_q F(t,t,q)\right] F(t,t',p) = 0$$
$$\left[\partial_t^2 + p^2 + m_0^2 + A\cos\Omega t + \frac{\lambda}{6}\int_q F(t,t,q)\right] \rho(t,t',p) = 0 \qquad (3.8)$$

The equations (3.8) describe coupled anharmonic parametric oscillators (one oscillator for each t' and p) with initial eigenfrequencies $\omega_0(p) = \sqrt{p^2 + m_{\text{eff}}(0)^2}$. Let us first discuss the entirely noninteracting case $\lambda = 0$, in which Eqs. (3.8) are independent Mathieu equations. It is known from classical mechanics, that the modes satisfying the resonance condition $2\omega_0(p) = n\Omega$ with $n = 1, 2, \ldots$ experience a parametric resonance and will grow exponentially in time. As there is no feedback on the spectrum of the system for $\lambda = 0$ this exponential growth in the resonant modes continues forever.
For finite λ, the exponential growth of the statistical correlation function $F(t,t',p)$ for momenta p satisfying the resonance condition leads to an exponential growth of the effective mass $m_{\text{eff}}^2(t) = m^2(t) + \lambda/6\int_q F(t,t,q)$, which shifts the dispersion of quasi-particles to higher energies and reduces the effective quasiparticle bandwidth $2[\sqrt{\Lambda^2 + m_{\text{eff}}(t)^2} - m_{\text{eff}}(t)]$ [78]. Therefore, the quasi-particle bandwidth will at a certain time lie entirely in between the parametric resonances and the system cannot absorb energy anymore, Fig. 3.5.
The failure of the system to absorb further energy can be traced back to the fact, that the LO self-energy is local in time and only leads to a renormalization of the quasi-particle dispersion. Except for this renormalization the quasi-particles remain sharp excitations and there is no mechanism present, that allows energy-transfer between them. Consequently, there is only energy absorption from the drive when the driving frequency hits the sharp resonance for the creation of quasi-particle pairs and the heating stops as soon as the resonance condition cannot be fulfilled anymore.

3.5 Thermalization through noise

We study the leading-order time evolution of the statistical Green's function subject to multiplicative noise

$$\left[\partial_t^2 + p^2 + m_0^2 + A\cos\Omega t + \frac{\lambda}{6}\int_q F(t,t,q) + \xi(t)\right] F(t,t',p) = 0. \qquad (3.9)$$

Introducing noise $\xi(t)$ is expected to mimic, at least very crudely, the effect of scattering. Therefore, the system is expected to heat to infinite temperature even with the leading order self-energy.

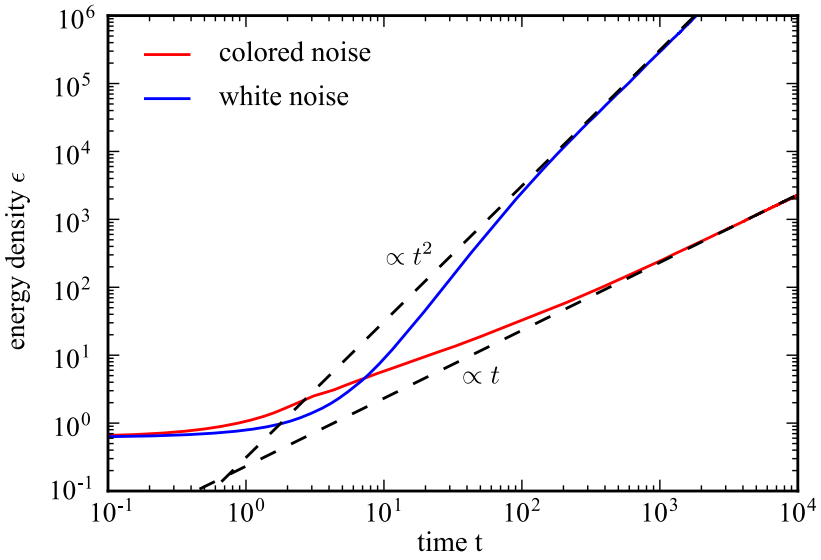

Figure 3.6: **Time evolution of the energy density obtained from leading order equations subject to noise.** With multiplicative noise the system absorbs energy indefinitely even at leading order. The energy density grows with a powerlaw $\epsilon(t) \sim t^{\alpha}$ for late times for arbitrary system parameters. Depending on whether the noise is white, i.e., completely uncorrelated in time or colored, i.e., correlated in time, the growth is quadratic or linear, respectively. From that we deduce that correlations in time slow down heating in the system. The data is shown for driving frequency $\Omega = 2.3$ and interaction strength $u = 1.0$. The strength of the white noise is $\gamma = 2.0/\Omega^2$ whereas for colored noise we have chosen $\sigma = 2/\Omega^2$ and $\tau = 20/\Omega$.

We explore two cases for the random process, which are white noise and correlated noise, respectively. In the case of white noise, $\xi_{\mathrm{w}}(t)$ reduce to Gaussian random variables with vanishing mean, $\langle \xi_{\mathrm{w}}(t) \rangle = 0$ and auto-correlation $\langle \xi_{\mathrm{w}}(t)\xi_{\mathrm{w}}(t') \rangle = \gamma^2 \delta(t - t')$. By contrast, the correlated noise $\xi_{\mathrm{c}}(t)$ obeys the stochastic differential equation of the Ornstein-Uhlenbeck process

$$d\xi_{\mathrm{c}}(t) = -\frac{1}{\tau}\xi_{\mathrm{c}}(t)dt + \sigma dW(t),\ \xi_{\mathrm{c}}(0) = 0, \tag{3.10}$$

where τ is the correlation time, σ controls the strength of the noise, and $W(t)$ is the standard Brownian motion. The auto-correlation of ξ_{c} is given by

$$\langle \xi_{\mathrm{c}}(t)\xi_{\mathrm{c}}(t') \rangle = \frac{\sigma^2 \tau}{2} \left(e^{-\frac{|t-t'|}{\tau}} - e^{-\frac{t+t'}{\tau}} \right) \tag{3.11}$$

and $\langle \xi_{\mathrm{c}}(t) \rangle = 0$. Note that white noise is recovered in the limit $\tau \to 0$, $\sigma \to \infty$, keeping $\sigma\tau = \gamma$ fixed. White noise is completely uncorrelated, while colored noise has exponentially decaying correlations in time. Hence, one expects that

the system thermalizes faster when it is subject to white noise. This is what we find by numerically solving Eq. (3.8). Moreover, we find that the energy-density grows according to a power-law $\epsilon(t) \sim t^{\alpha}$; Fig. 3.6. We exploit the similarity of Eq. (3.8) and an anharmonic oscillator, for which it has been shown that the energy grows quadratically in time for white noise ($\alpha = 2$), whereas colored noise leads to a linear growth $\epsilon \sim t$ ($\alpha = 1$) [92, 93]. The dynamical evolution in our system, Eq. (3.9), confirms these expectations. Therefore, the heating due to either white ($\epsilon \sim t^2$) or colored ($\epsilon \sim t$) noise is substantially faster than the asymptotic heating we observe when solving the equations of motion self-consistently up to NLO ($\epsilon \sim \sqrt{t}$). We attribute the slow heating obtained from the full solution up to NLO to the strong interactions between quasi-particles which cannot be simply mimicked by multiplicative noise.

3.6 Conclusions

Our results demonstrate, that a prethermal Floquet state can be stabilized in a periodically-driven quantum many-body system, despite strong interactions and despite the driving frequency being comparable to microscopic energy scales of the system. This opens the possibility of realizing exotic states in the Floquet prethermal regime, such as time crystals or other novel symmetry protected topologically phases. Furthermore, our study suggests a algebraic heating at late times of the form $\epsilon(t) \sim \sqrt{t}$, which is significantly slower than the linear Joule heating. We attribute this peculiar form of heating to the strong interactions between the dynamically generated quasi particles. How such a sublinear growth can be reconciled with the eigenstate thermalization hypothesis is an important open question. A future study based on a Floquet Boltzmann type approach might provide further insights into this behavior

Chapter 4

Dynamical quantum phase transitions in systems with continuous symmetry breaking

The text and figures in this chapter are taken from the following publication of the author:

- **Simon A. Weidinger**, Markus Heyl, Alessandro Silva, Michael Knap, "Dynamical Quantum Phase Transitions in Systems with Continuous Symmetry Breaking", *Phys. Rev. B* **96**, 134313 (2017)

In order to provide a structure better suited to this thesis, certain sections have been merged and rearranged or renamed.

4.1 Two concepts of dynamical quantum phase transitions

In recent years, synthetic quantum matter such as ultra-cold atoms, polar molecules, and trapped ions have demonstrated their capabilities to experimentally study nonequilibrium quantum states far beyond the regime of linear response and thus far beyond a thermodynamic description. Due to the isolation from the environment and the high level of control, experiments with synthetic quantum matter have shown that inherently dynamical phenomena can be realized and probed, ranging from many-body localization,[27, 28, 29, 30, 31, 32, 33], prethermalization,[94, 95] discrete time crystals,[34, 35] the particle-antiparticle production in the Schwinger model,[36] to emergent Bloch oscillations.[96] In addition, not only the dynamical phases themselves have become accessible in experiments, but also the associated dynamical transitions between the phases.[24, 25, 26]
Current experimental platforms for studying dynamics are often focusing on one- and two-dimensional systems. Yet, a future prospect concerns extensions toward the realization of non-equilibrium many-body states in three spatial dimensions, where new physical phenomena become accessible. This includes, for example, the possibility of spontaneously broken continuous symmetries at nonzero temperatures, which is excluded for lower dimensions due to the Mermin-Wagner theorem in systems with short range interactions.
In this work, we study the quantum dynamics of an interacting many-body system in three dimensions which exhibits such a spontaneously broken symmetry. Specif-

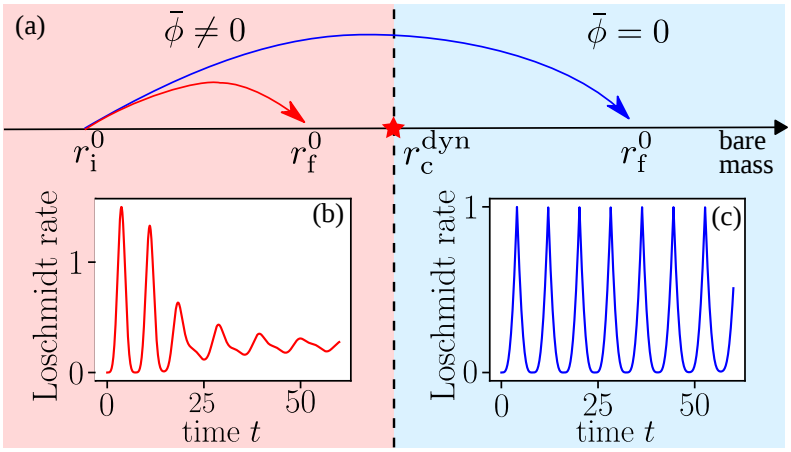

Figure 4.1: **Dynamical criticality in the Loschmidt echo for systems with spontaneous symmetry breaking**. (a) We study dynamical quantum phase transitions of the O(N) model following quantum quenches from an initial bare mass r_i^0 to a final bare mass r_f^0. The initial state is chosen to break the continuous symmetry of the O(N) model and hence is described by a finite order parameter. Our system exhibits a steady-state dynamical phase transition at $r_c^{\rm dyn}$, which separates the dynamically ordered phase in which the long-time average of the order parameter $\bar{\phi}$ remains finite, from the disordered phase in which $\bar{\phi}$ vanishes. We analytically calculate the Loschmidt echo and find that the associated rate function remains smooth for quenches within the dynamically ordered phase (b) but exhibits nonanalytic kink singularities when crossing the dynamical critical point $r_c^{\rm dyn}$ (c).

ically, we calculate the unitary real-time evolution of the O(N) vector model following a quantum quench of the mass, with an initial state that breaks the continuous symmetry of our system, see Fig. 4.1. We approach the problem fully analytically via the large-N limit, where the dynamics can be solved exactly.
The O(N) model exhibits a dynamical quantum phase transition in the asymptotic steady state, separating two dynamical phases with finite and vanishing order parameter, respectively. [97] Here, we show that in addition to the dynamical steady-state transition of the order parameter, the O(N) model exhibits a critical dynamical phenomenon on transient time scales. In particular, non-analyticities appear in the Loschmidt echo periodically in time when the dynamical transition is crossed by the quantum quench (Fig. 4.1). We show that in the O(N) model these singularities contribute only subextensively to the rate function associated with the Loschmidt echo. Making use of the analogy between the Loschmidt echo and the boundary partition function, this effect is reminiscent of surface phase transitions in equilibrium systems, which also contribute only subextensively to the free energy.[98] Furthermore, we find that the dynamical critical point obtained from the order parameter coincides with the one obtained from the Loschmidt echo. These different concepts of dynamical criticality are further linked by the fact that the non-analyticities in the Loschmidt echo occur at times when the order parameter crosses zero. A similar relation has been found in the long-range transverse-field Ising model.[99] We argue that our results are not specific to the O(N) model or the large-N limit, and hence apply to generic systems with a spontaneously broken continuous symmetry.

DPT-I: Order parameter dynamical quantum phase transitions

The first one, is associated with the time evolution of the order parameter.[100, 101, 102, 103, 104, 97, 105, 106, 99, 107, 108] The dynamical quantum phase transition is then characterized by a critical point which separates regimes where the long-time average of the order parameter $\bar{\phi}$ is either finite or zero. Close to this dynamical critical point the long-time average $\bar{\phi}$ exhibits scaling relations with critical exponents.[97, 106] However, the location of the dynamical critical point can in general differ from the equilibrium one and might also depend on the initial state, due to a dynamical renormalization of parameters.[106, 97]

DPT-II: Loschmidt echo dynamical quantum phase transitions

A second approach to study the nonequilibrium dynamical criticality is to exploit the formal similarity between the equilibrium partition function $Z = \mathrm{tr}[e^{-\beta\hat{H}}]$ and the Loschmidt amplitude $\langle\psi_0|e^{-i\hat{H}t}|\psi_0\rangle$. [109, 110] The equilibrium partition function becomes non-analytic at a conventional phase transition as a function of the control parameter such as temperature or pressure. It turns out, that the Loschmidt amplitude can also exhibit nonanalyticities, but as a function of time rather than a control parameter. Indeed it has been shown that the rate function, which is obtained from taking the logarithm of the Loschmidt amplitude, exhibits nonanalytici-

ties when the system is quenched across a quantum critical point whereas it remains smooth for quenches within the same dynamical phase.[109, 111, 110, 112, 113, 114, 115, 116, 117, 118, 99, 119, 107, 120, 108]. Recently, it became also possible to measure Loschmidt amplitudes in various experimental settings. [121, 24]
So far the Loschmidt amplitude has mostly been studied for one dimensional systems with discrete $\mathbb{Z}_2$ symmetries (see, however, Refs. [114, 116, 120]). In this work, we look at a three dimensional model with a continuous O(N) symmetry: the O(N) vector model. This model provides a universal description for many systems close to their critical point and is well established in the study of (non-equilibrium) quantum phase transitions.[50, 86, 97, 106, 88, 89] For example, the equilibrium Mott-insulator to superfluid transition in the Bose-Hubbard model falls into the universality class of the O(2) model and the Heisenberg antiferromagnet can be described by an O(3) model.
We propose the following generalization of the Loschmidt echo to systems with a continuously broken symmetry

$$\mathcal{L}(t) = \int\limits_{\{|\chi|=\phi_0\}} d^N\chi \, |\langle\chi|\Psi(t)\rangle|^2. \tag{4.1}$$

Here, $|\Psi(t)\rangle = \hat{U}(t)|\psi_0\rangle$ is the time evolved state after the quench and the integral is taken over the full set of symmetry-broken ground states $|\chi\rangle$, which can be pictured as a sphere within an N-dimensional space. The radius ϕ_0 is set by the order parameter in the initial state. Below we will analyze the dynamics of the rate function associated with the Loschmidt echo

$$\mathcal{R}(t) = -\frac{1}{L^d N} \log \mathcal{L}(t), \tag{4.2}$$

which shows nonanalytic behavior for quantum quenches from the dynamically ordered to the disordered phase.

4.2 Time evolution of a quantum state in the O(N)-model at large N

Heisenberg equations of motion in the mode function formalism

Let us assume in the following, that the system has been prepared in the symmetry-broken ground state $|\Psi_0\rangle$ at r_i^0, with the order parameter $\langle\hat{\Phi}_a\rangle = \delta_{1,a}\phi_0$ pointing along the $a = 1$ direction. The value of ϕ_0 is given by

$$(\phi_0)^2 = -\frac{6r_\mathrm{i}^0}{\lambda} - (N-1)\langle\hat{\Phi}_2\hat{\Phi}_2\rangle, \tag{4.3}$$

which follows directly from the initial mass being zero. Here, we also used, that there is a remaining $O(N-1)$-symmetry for the $a \geq 2$ components. We then

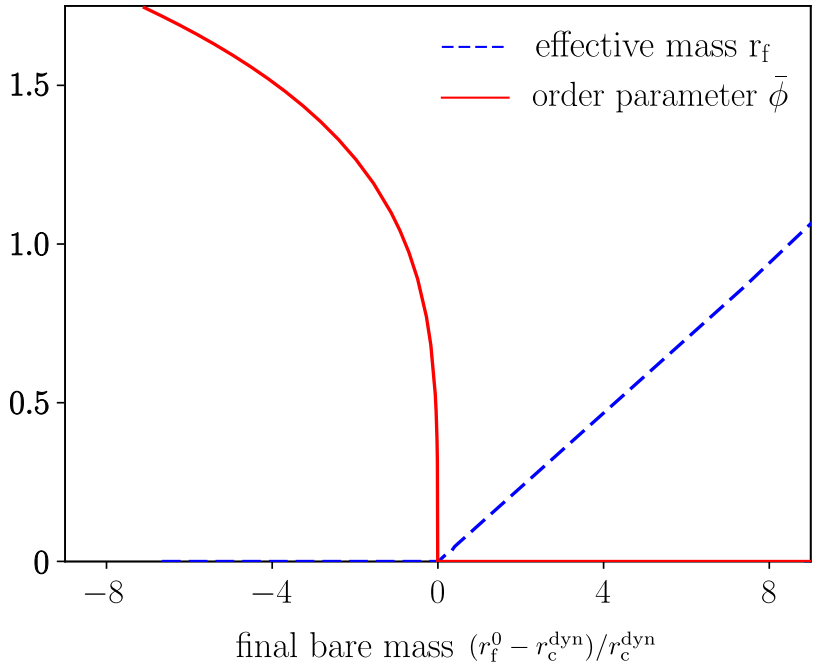

Figure 4.2: **Dynamical phase diagram of the O(N) model in three spatial dimensions.** The system is prepared in the equilibrium symmetry broken phase at zero temperature. For quenches to a point inside of the dynamically symmetry-broken phase, $r_f^0 < r_c^{dyn}$, the order parameter relaxes to a finite value $\bar{\phi}$ (red line) and the effective mass r_f remains zero, indicating the presence of gapless excitations in the steady state. For quenches into the symmetric phase, $r_f^0 > r_c^{dyn}$, the long-time average of the order parameter is zero $\bar{\phi} = 0$ and the effective mass r_f becomes finite (blue dashed line). Close to the critical point r_c^{dyn} the long-time average $\bar{\phi}$ vanishes as $(r_c^{dyn} - r_f^0)^{1/4}$ and the effective mass as $r_f \sim (r_f^0 - r_c^{dyn})$.[97]

suddenly change the mass to the final value $r_0 = r_\mathrm{f}^0$ and let the system evolve in time. If the final value r_f^0 is smaller than the dynamical critical value $r_\mathrm{c}^\mathrm{dyn}$, the system reaches an ordered steady state characterized by $r_\mathrm{f} = 0$ and $\bar{\phi} = \lim_{T\to\infty} \frac{1}{T}\int_0^\infty dt\phi(t) > 0$.[97] On the other hand, if $r_\mathrm{f}^0 > r_\mathrm{c}^\mathrm{dyn}$ the order is melted. Therefore, the effective mass $r_\mathrm{f} > 0$ and the order parameter $\bar{\phi} = 0$, as illustrated in the dynamical phase diagram for $d = 3$ in Fig. 4.2.
To obtain the equations of motion at $N \to \infty$, we treat the $a = 1$ component of the field as a classical variable, $\hat{\Phi}_1(t) \to \phi(t) \in \mathbb{R}$, and expand the $a \geq 2$ components into creation and annihilation operators that diagonalize the initial Hamiltonian[106]

$$\hat{\Phi}_{a\geq 2}(p,t) = f_p(t)\hat{b}_p^{(a)} + f_p^*(t)\hat{b}_{-p}^{(a)\dagger}, \tag{4.4}$$

where $\hat{\Phi}_a(x,t) = V^{-1/2}\sum_p \hat{\Phi}_a(p,t)e^{ipx}$. Note, that due to the $O(N-1)$ symmetry of the remaining $a \geq 2$ components, the time dependence is identical for all of them and hence the mode functions $f_p(t)$ in Eq. (4.4) do not carry a field component index.
Using the Heisenberg equations of motions, we obtain

$$\begin{aligned} &\ddot{f}_p(t) + [p^2 + r(t)]f_p(t) = 0 \\ &\ddot{\phi}(t) + r(t)\phi(t) = 0, \end{aligned} \tag{4.5}$$

with the time-dependent effective mass

$$r(t) = r_\mathrm{f}^0 + \frac{\lambda}{6N}\left(\phi^2(t) + (N-1)\int_p |f_p(t)|^2\right). \tag{4.6}$$

It is important to notice, that $\phi(t) \sim \sqrt{N}$. Therefore, both terms in the parenthesis in Eq. (4.6) scale linearly with N and contribute to the effective mass.
The initial conditions of Eq.'s (4.5) are $f_p(0) = 1/\sqrt{2|p|}$, $\dot{f}_p(0) = -i\sqrt{|p|/2}$, which follow from requiring that $\hat{b}_p$, $\hat{b}_p^\dagger$ diagonalize the initial Hamiltonian and $r(t=0) = 0$. Furthermore we have $\phi(0) = \phi_0$ and $\dot{\phi}(0) = 0$, with ϕ_0 given by Eq. (4.3). To regularize the infrared divergence of $f_p(0)$, we introduce an cut-off $p_0 = 2\pi/L$, with L being the linear extension of the system. This amounts to placing the field theory in a finite box with volume L^d. Eventual UV divergencies are regularized with a finite cut-off Λ in momentum space.

Time evolved state

In order to calculate the return probability to the groundstate manifold, we need to know the time evolved state $|\Psi(t)\rangle = \hat{U}(t)|\Psi_0\rangle$. In the $N \to \infty$ limit the state $|\Psi(t)\rangle$ factorizes in the field components due to the effectively quadratic Hamiltonian at leading order.[106] In the $a \geq 2$ components there is a squeezed state

$|\psi_{\mathrm{sq}}(t)\rangle$ and in the "classical" $a = 1$ component a coherent state $|\phi(t)\rangle$,

$$
\begin{aligned}
|\Psi(t)\rangle &= |\phi(t)\rangle \otimes |\psi_{\mathrm{sq}}(t)\rangle \\
|\phi(t)\rangle &= e^{-\frac{1}{2}\gamma^2\phi^2(t)} e^{\gamma\phi(t)\hat{b}_{p_0}^{(1)\dagger}} |0\rangle \\
|\psi_{\mathrm{sq}}(t)\rangle &= \prod_{\substack{p>0 \\ a\geq 2}} \frac{1}{\sqrt{|\alpha_p(t)|}} \exp\left\{ \frac{\beta_p^*(t)}{2\alpha_p^*(t)} (\hat{b}_p^{(a)\dagger})^2 \right\} |0\rangle,
\end{aligned} \tag{4.7}
$$

where $\alpha_p(t) = f_p(t)\sqrt{\frac{|p|}{2}} + i\frac{\dot{f}_p(t)}{\sqrt{2|p|}}$, $\beta_p(t) = f_p(t)\sqrt{\frac{|p|}{2}} - i\frac{\dot{f}_p(t)}{\sqrt{2|p|}}$ and $\gamma = L^{\frac{d-1}{2}} \left(\frac{\sqrt{d}\pi}{2}\right)^{\frac{1}{2}}$. The coherent state contribution gives rise to a finite order parameter $\langle\Psi(t)|\hat{\Phi}_1|\Psi(t)\rangle = \phi(t)$.

4.3 Return probability and rate function

Return probability

An arbitrary state in the groundstate manifold of (6.8) in the symmetry-broken phase can be written as

$$
|\chi\rangle = e^{-\frac{1}{2}\gamma^2\chi^2} e^{\gamma\chi^T\hat{b}_{p_0}^\dagger}|0\rangle, \tag{4.8}
$$

where $\chi = (\chi_1, \ldots, \chi_N)$, $|\chi|^2 = \phi_0^2$ and $\hat{b}_p = (\hat{b}_p^{(1)}, \ldots, \hat{b}_p^{(N)})$. The expectation of the field-operator in this state is given by $\langle\chi|\hat{\Phi}_a|\chi\rangle = \chi_a$. The overlap $\langle\chi|\Psi(t)\rangle$ factorizes into a product over the field components. For $a = 1$ we get a scalar product of two coherent states and for $a \geq 2$ we have scalar products of a coherent and a squeezed state, which we calculate by expanding the exponentials. For the return probability to a specific initial state, we obtain

$$
\begin{aligned}
|\langle\chi|\Psi(t)\rangle|^2 = \exp\Bigg\{ & -L^d N \int_p \log|\alpha_p(t)| \\
& - L^{d-1}\frac{\sqrt{d}\pi}{2}[\phi^2(t) + \phi^2(0) - 2\chi_1\phi(t) + \sum_{a\geq 2}\chi_a^2] \Bigg\}.
\end{aligned} \tag{4.9}
$$

In deriving this formula we also made use of the fact, that for large systems, $L \gg 1$, i.e., small $p_0 = 2\pi/L$, the ratio $\beta_{p_0}(t)/\alpha_{p_0}(t)$ approaches 1.
The overlap $|\langle\chi|\Psi(t)\rangle|^2$ is rotational invariant around the $a = 1$ axis. Hence, we use spherical coordinates (see Fig. 4.3) to calculate the integral over the groundstate manifold as required in Eq. (4.1). Defining $\theta \in [0, \pi]$ as the angle between the

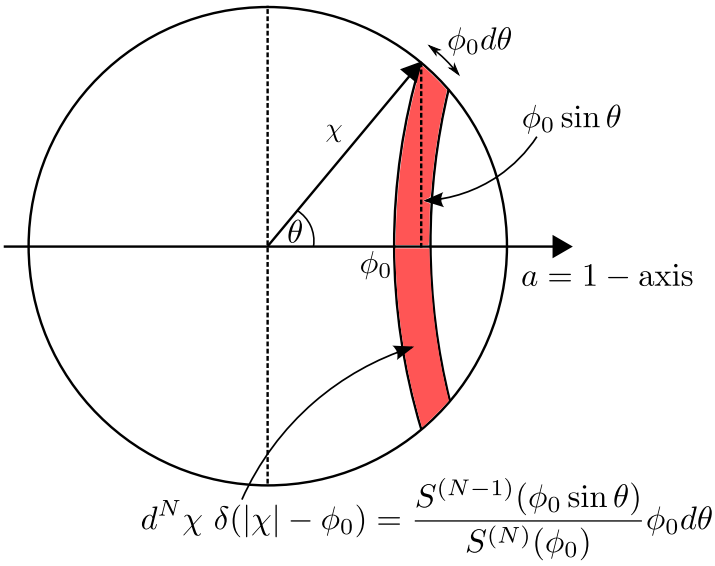

Figure 4.3: **Definition of the angle θ and surface element of the N-dimensional sphere.** The ground state manifold of the $O(N)$ model can be pictured as a sphere with radius ϕ_0 in a N-dimensional space. The return probability $\mathcal{L}(t)$ to the ground state manifold is obtained from the integral of the overlap $|\langle\chi|\Psi(t)\rangle|^2$ over this sphere. Defining θ as the angle between the vector χ and the initial order parameter $(\phi_0, 0, \ldots, 0)$ and making use of the rotational symmetry around the $(a = 1)$-axis, one can write the integration element $d^N\chi\ \delta(|\chi| - \phi_0)$ as the product of the arc length $\phi_0 d\theta$ and the surface area of the sphere in $N - 1$ dimensions $S^{(N-1)}(\phi_0 \sin\theta)$ generated by rotating χ around the $a = 1$ - axis with θ fixed. To obtain a probability measure, we finally divide the integration element by the total available surface area $S^N(\phi_0)$.

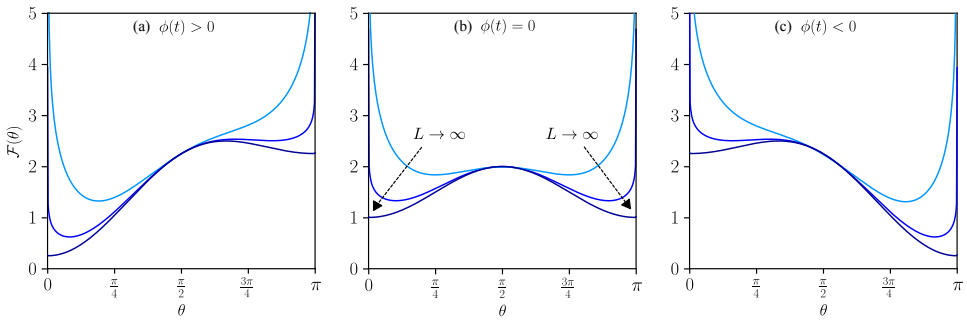

Figure 4.4: **Order parameter landscape for the angle θ:** The return probability, Eq. (4.11), can be interpreted as a classical partition function for the variable $\theta \in [0, \pi]$ moving in an effective free energy landscape $\mathcal{F}(\theta, \phi)$. The landscape has the form of a double well potential, where the order parameter $\phi(t)$ is acting as an external field, shifting the two wells against each other. For (a) $\phi(t) > 0$ the left minimum is energetically more favorable, while for (c) $\phi(t) < 0$ the situation is reversed. As the system size L is increased ($L = 1, 5, \infty$, darker lines correspond to larger L), the left (right) potential well is shifted toward $\theta = 0$ ($\theta = \pi$), as indicated by the arrows in panel (b). The angles $\theta = 0$ ($\theta = \pi$) correspond to the states having an order parameter parallel (anti-parallel) to the initial state. (b) When $\phi(t)$ changes sign the most relevant value of θ jumps from one well to the other, which gives rise to the kinks in the Loschmidt rate function $\mathcal{R}(t)$. All plots are for $N = 10$.

vector χ and the $a = 1$ axis, i.e., $\cos\theta = \chi_1/\phi_0$, we can write

$$|\langle\chi|\Psi(t)\rangle|^2 = \mathcal{N}_{\mathrm{sq}}(t)\exp\Bigg\{-L^{d-1}\frac{\sqrt{d}\pi}{2}\phi^2(0) \times\left[1+\left(\frac{\phi(t)}{\phi(0)}\right)^2+\sin^2\theta-2\left(\frac{\phi(t)}{\phi(0)}\right)\cos\theta\right]\Bigg\}. \tag{4.10}$$

Here, we introduced the abbreviation $\mathcal{N}_{\mathrm{sq}}(t) = \exp[-L^d N\int_p \log|\alpha_p(t)|]$. The integration element can be written as $d^N\chi\,\delta(|\chi|-\phi_0) = S^{N-1}(\phi_0\sin\theta)\phi_0 d\theta/S^N(\phi_0)$, where $S^n(r) = 2\pi^{\frac{n}{2}}\Gamma(n/2)^{-1}r^{n-1}$ is the surface of the n-sphere (see Fig. 4.3 for a graphical interpretation). Exponentiating the $\sin\theta$ - term, we obtain the return probability to the ground state manifold

$$\mathcal{L}(t) = A\,\mathcal{N}_{\mathrm{sq}}(t)\int_0^\pi d\theta e^{-L^{d-1}N\mathcal{F}(\theta,\phi(t))}, \tag{4.11}$$

with

$$\mathcal{F}(\theta,\phi) = \sqrt{\frac{\pi}{2}}\frac{\phi_0^2}{N}\left[1+\left(\frac{\phi}{\phi_0}\right)^2-2\left(\frac{\phi}{\phi_0}\right)\cos\theta+\sin^2\theta\right] - \frac{N-2}{N}L^{-d+1}\log\sin\theta \tag{4.12}$$

and a constant $A = \pi^{-1/2}\Gamma(\frac{N}{2})/\Gamma(\frac{N-1}{2})$. We will refer to $\mathcal{L}(t)$ also as Loschmidt Echo. Eq. (4.11) can be interpreted as a classical partition function of the angular variable θ moving in an order parameter landscape $\mathcal{F}(\theta,\phi(t))$, with $L^{d-1}N$ playing the role of inverse temperature. The energy landscape, Eq. (4.12), has the shape of a double well potential, where the order parameter ϕ is acting as an external field tilting the two wells against each other, see Fig. 4.4. The two wells are energetically equivalent, when the external field vanishes ($\phi(t) = 0$). For increasing L the two minima shift toward $\theta = 0$ and $\theta = \pi$, respectively. It appears as if the $\log\sin\theta$ term becomes irrelevant for $L\to\infty$, but it is still important as it confines the angle θ to the interval $[0,\pi]$.
In the thermodynamic limit $L \gg 1$, we can evaluate the integral in Eq. (4.11) using a saddle point approximation. Taking this limit corresponds to very low temperatures in the classical partition function and the variable θ will pick the minimum energy well

$$\mathcal{L}(t) \underset{L\gg1}{\simeq} \mathcal{N}_{\mathrm{sq}}(t)\exp\left[-L^{d-1}N\min_{\theta\in[0,\pi]}\mathcal{F}(\theta,\phi(t))\right]. \tag{4.13}$$

For $L\to\infty$, the last term in Eq. (4.12) vanishes and the minimum is at $\theta_{\min} = 0$ ($\theta_{\min} = \pi$) for $\phi(t) > 0$ ($\phi(t) < 0$), meaning that χ is parallel (antiparallel)

to the order parameter of the initial state. Therefore, only two states from the continuous ground state manifold contribute significantly to the Loschmidt echo: $\mathcal{L}(t) \sim (|\langle +\phi_0|\Psi(t)\rangle|^2 + |\langle -\phi_0|\Psi(t)\rangle|^2)$. This can be interpreted as follows: the order-parameter oscillates only along a fixed axis due to the symmetry of the Hamiltonian and cannot explore the whole ground state manifold.
Our result for the coherent state contribution to the Loschmidt rate function scales subextensively with system size as $\sim L^{d-1}$, see the prefactor of $\mathcal{F}(\theta, \phi(t))$ in Eq. (4.13). This is a consequence of the infrared divergence of the initial mode function $f_p(0)$ due to the spontaneously broken symmetry, which leads to the scaling of $\gamma \sim L^{(d-1)/2}$ in the coherent state, Eq. (4.7). From that, the wavefunction overlap $\langle\chi|\Psi(t)\rangle$ of the time evolved state and an arbitrary state in the ground state manifold contains terms, that scale subextensively $\sim L^{d-1}$. We emphasize that the subextensive scaling shows up only in the wave function overlap but not in expectation values of observables. Examples include the order parameter and the work performed in a quench. The latter shows a normal extensive scaling $\sim L^d$ with system size. The average work $\langle \hat{H}_f \rangle$ is given by the expectation value of the post-quench Hamiltonian in the initial state, $\langle \hat{H}_f \rangle = L^d \frac{r_f^0 - r_i^0}{2}(N \int_p \frac{1}{2|p|} + \phi_0^2)$. All higher cumulants of the work distribution function vanish in our leading order approximation. Generally, the logarithm of the Loschmidt amplitude acts as the generating function for cumulants of the work-distribution.[122, 123, 124] We also find in our model that to leading order in N, the Loschmidt echo reproduces exactly the cumulants of the work.

Rate function

Calculating the rate function $\mathcal{R}(t) = -L^{-d}N^{-1}\log\mathcal{L}(t)$ from Eq.(4.13), we find that

$$\begin{aligned}
\mathcal{R}(t) &= \mathcal{R}_{\mathrm{sq}}(t) + \frac{1}{L}\mathcal{R}_{\mathrm{coh}}(t) \\
\mathcal{R}_{\mathrm{sq}}(t) &= \int_p \log|\alpha_p(t)| \\
\mathcal{R}_{\mathrm{coh}}(t) &= \sqrt{\frac{\pi}{2}} N^{-1}\phi_0^2 \left[1 + \left(\frac{\phi(t)}{\phi_0}\right)^2 - 2\left|\frac{\phi(t)}{\phi_0}\right|\right].
\end{aligned} \tag{4.14}$$

The contribution from the squeezed state $\mathcal{R}_{\mathrm{sq}}$ is obtained from $\mathcal{N}_{\mathrm{sq}}$, and the coherent state contribution is obtained by explicitly calculating the minimum in Eq. (4.13). The rate function $\mathcal{R}_{\mathrm{sq}}$ is a smooth function of time, since $|\alpha_p(t)|$ is smooth and bounded from below by 1. $\mathcal{R}_{\mathrm{coh}}$ on the other hand exhibits kinks at zero crossings of $\phi(t)$ due to the absolute value in the last term of Eq. (4.14). As discussed above, the coherent state contribution is suppressed by a factor of L^{-1}. However, the squeezed-state part of the rate function $\mathcal{R}_{\mathrm{sq}}(t)$ relaxes to a constant value on a much shorter time-scale than the order parameter $\phi(t)$, because of an integral over momenta. Therefore, the non-analyticities in $\mathcal{R}_{\mathrm{coh}}(t)$ can be

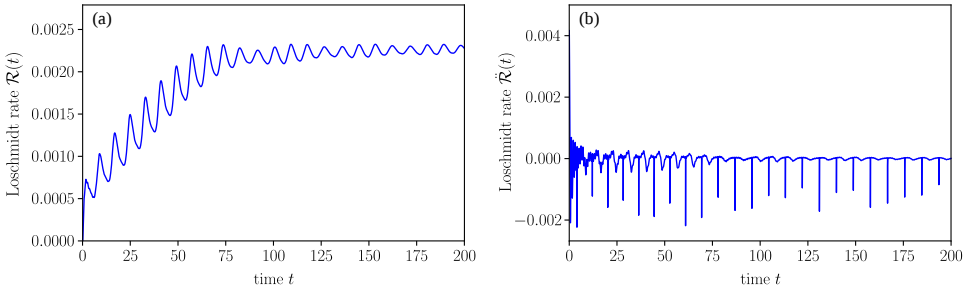

Figure 4.5: **Loschmidt rate function.** The Loschmidt rate function $\mathcal{R}(t)$ of the return probability to the groundstate manifold contains a squeezed state contribution $\mathcal{R}_{\mathrm{sq}}(t)$, which scales extensively with system size, and a coherent state contribution $\mathcal{R}_{\mathrm{coh}}(t)$ that scales subextensively. Whereas $\mathcal{R}_{\mathrm{sq}}(t)$ is a smooth function of time, $\mathcal{R}_{\mathrm{coh}}(t)$ shows kinks, when the system is quenched across the dynamical quantum phase transition. Due to the subextensive scaling of the coherent state contribution $\mathcal{R}_{\mathrm{coh}}$, the non-analytic behavior is not visible in the full rate-function $\mathcal{R}(t)$ of the return probability, (a). Nevertheless the non-analytic behavior is clearly observable in the second derivative $\ddot{\mathcal{R}}(t)$ as δ-peaks, since the squeezed state contribution relaxes on a much shorter time scale than the one of the coherent state, (b). The system parameters are $L = 2.5 \times 10^4$, $\lambda = 1.0$, $r_{\mathrm{i}}^0 = -1.0$ and $r_{\mathrm{f}}^0 = 0.0$.

identified for instance in the second derivative $\ddot{\mathcal{R}}(t)$ of the rate function. For the squeezed state, $\ddot{\mathcal{R}}_{\mathrm{sq}}(t) \approx 0$, whereas the coherent state retains prominent δ-peaks $\ddot{\mathcal{R}}_{\mathrm{coh}}(t) \sim \sum_{T_{\mathrm{kink}}} \delta(t - T_{\mathrm{kink}})$, as illustrated in Fig. 4.5.
The coherent state contribution to the Loschmidt rate function $\mathcal{R}_{\mathrm{coh}}(t)$ exhibits kinks at the zero crossings of the order parameter, $\phi(T_{\mathrm{kink}}) = 0$, see Fig. 4.6. From the numerical solution of the equations of motion (4.5) we also find that the order parameter relaxes to a non-zero value for quenches inside the dynamical symmetry-broken phase ($r_{\mathrm{f}}^0 < r_{\mathrm{c}}^{\mathrm{dyn}}$). In this case there are no zero crossings of $\phi(t)$ and hence we do not find any non-analyticities in $\mathcal{R}_{\mathrm{coh}}$. By contrast, for quenches to the symmetric phase ($r_{\mathrm{f}}^0 > r_{\mathrm{c}}^{\mathrm{dyn}}$), the order parameter oscillates around zero and approaches $\bar{\phi} = 0$ and $\mathcal{R}_{\mathrm{coh}}$ exhibits kinks. As a consequence, there is an intimate relation between the dynamical phase transition of the order parameter and the kinks in the Loschmidt rate function of the return probability to the groundstate manifold.
Following a quench to the symmetric phase, the effective mass $r(t)$, Eq. (4.6), attains a finite average value r_{f}, which feeds back into the equations of motion, Eq. (4.5), as frequency squared of $\phi(t)$. Accordingly, the kinks in $\mathcal{R}_{\mathrm{coh}}$ appear at equidistantly spaced times T_{kink} and the time ΔT_{kink} between two kinks is uniquely determined by r_{f}. The effective mass after a quench to the symmetric phase scales linearly with the distance of the final bare mass r_{f}^0 from the dynamical critical point

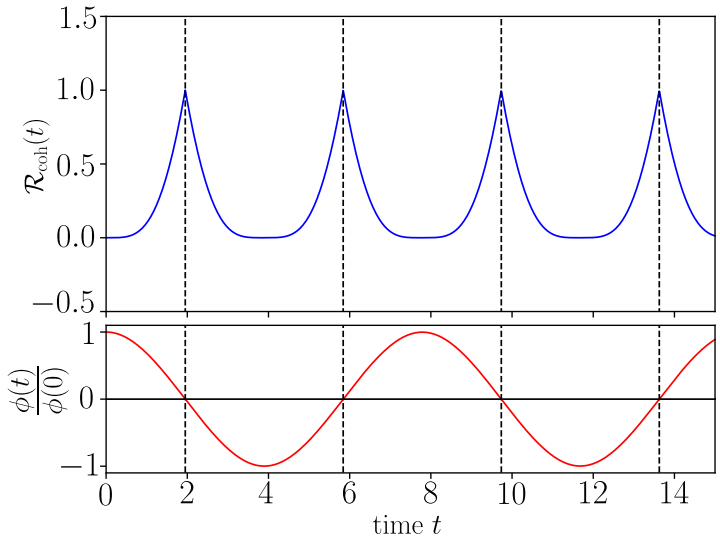

Figure 4.6: **Coherent state contribution to the rate function and order parameter dynamics.** The coherent state contribution $\mathcal{R}_{\rm coh}$ to the rate function exhibits kinks at the zero-crossings of the order parameter $\phi(t)$. The kinks appear periodically and the time between them $\Delta T_{\rm kink}$ is determined by final effective mass $r_{\rm f}$: $\Delta T_{\rm kink} \sim (r_{\rm f}^0 - r_{\rm c}^{\rm dyn})^{-\frac{1}{2}}$. The data is evaluated for the same parameters as in Fig. 4.5

$r_{\rm c}^{\rm dyn}$, $r_f \sim r_{\rm f}^0 - r_{\rm c}^{\rm dyn}$, as depicted in Fig. 4.2. We therefore find

$$\Delta T_{\rm kink} = \frac{\pi}{\sqrt{r_{\rm f}}} \sim (r_{\rm f}^0 - r_{\rm c}^{\rm dyn})^{-\frac{1}{2}}. \tag{4.15}$$

Therefore, the time between the kinks diverges with the same critical exponent upon approaching the dynamical critical point as the correlation length in equilibrium, which is a manifestation of the O(N) model being a relativistic field theory in which time and space scale in the same way.

4.4 Conclusion

We have studied the rate function of the return probability to the ground state manifold in the O(N) model following a quantum quench from a symmetry breaking initial state to the symmetric phase. The rate function exhibits kinks, which are located at the zero crossings of the order parameter $\phi(t)$ and are equally spaced with a period $\Delta T_{\rm kink}$ determined by the final effective mass. In our model, the non-analytic contribution to the return probability scales subextensively with system size. Such a subextensive contribution can also appear in equilibrium whenever a system undergoes a surface or impurity phase transition.

For quenches from the symmetric to the symmetry-broken phase kinks are absent, since the closing of the gap leads to a divergent time scale between kinks. Also, due to the absence of explicit symmetry-breaking terms in the Hamiltonian, no finite order parameter can be ever generated.
Our results for the non-equilibrium dynamics are obtained fully analytically to leading order in the number of components N of the field theory. We point out that the saddlepoint approximation, which we employ in the calculation of the return probability, only relies on the thermodynamic limit $L \to \infty$ and not on N being large. Furthermore the presence of kinks in the rate function $\mathcal{R}(t)$ hinges on the presence of the coherent state, i.e., a finite order parameter $\phi(t)$. Next-to-leading order corrections would modify the time evolution of the order parameter and the quantum fluctuations in the time evolved state, but would not destroy the symmetry-broken phase, i.e. the coherent contribution to the time evolved state. Therefore, we argue, that our results remain valid beyond a leading order approximation in $1/N$. Moreover, due to the universality of the O(N) model, we expect our results to be generic for dynamical critical points in models with continuous symmetries. In particular, the return probability should be dominated by the states parallel and anti-parallel to the initial state, leading to non-analytic behavior of the rate function for quenches from the symmetry-broken to the symmetric phase. Moreover, the zero crossings of the order parameter should determine the times at which nonanalyticities appear in the Loschmidt echo. It would be intriguing to explore these findings in other models with continuous symmetry breaking.

Chapter 5

A self-consistent Hartree-Fock approach to Many-Body Localization

The text and figures in this chapter are taken from the following publication of the author:

- **Simon A. Weidinger**, Sarang Gopalakrishnan, Michael Knap, "A self-consistent Hartree-Fock approach to Many-Body Localization", *arXiv:*1809.02137 (2018)

In order to provide a structure better suited to this thesis, certain sections have been merged, rearranged or renamed.

5.1 The problem of many-body localization

In recent years the phenomenon of many-body localization (MBL) has attracted major interest, both experimentally [125, 126, 127, 128, 129, 130, 131, 132, 133, 134, 135] and theoretically [8, 9, 10, 11, 12]. MBL systems, unlike generic quantum many-body systems, do not thermalize [136, 137, 138, 11]. In these systems, entanglement entropy grows logarithmically, and local quantum correlations survive for long times [139, 140, 141, 142, 143, 144, 145, 146]. The transition from the thermal to the MBL phase is an unconventional dynamical phase transition, and its critical properties have attracted much recent attention [147, 148, 149, 150, 151, 152, 153, 154, 155, 156, 157, 158]. Since the MBL phase does not thermalize, it is impossible to describe the MBL phase transition and the critical phenomena associated with it in the framework of equilibrium statistical physics. The central obstacle is that while the regimes deep in the thermal phase and deep in the localized phase are phenomenologically well understood [159, 160, 161, 162, 163], these phenomenologies (based respectively on equilibrium statistical physics and on local integrals of motion) are incompatible with one another, and both break down as the transition is approached.
In the present paper, we develop a field theoretic description of the many-body localization problem in the two-particle irreducible (2PI) Keldysh framework [164, 165, 46] by looking at the relaxation dynamics of initial states. Using a self-consistent weak-coupling expansion, we arrive to leading order at a self-consistent Hartree-Fock theory of the many-body dynamics, in which single particles move in the presence of the noise due to the other particles. At the Hartree-Fock level we are able to simulate the dynamics of systems of up to 192 sites for times up to $10^4 / J$

where J is the hopping. The Hartree-Fock theory captures both the slowdown of thermalization and the onset of a delocalized, subdiffusive phase in random systems [149, 150, 151, 166, 167, 168, 169, 170, 171, 172, 173]. By contrast, this subdiffusive phase is absent for systems with quasiperiodic potentials, consistent with Ref. [174].
Our approach also gives us access to the non-equilibrium local spectral function, which is expected to look qualitatively different for localized and delocalized systems [8]. Indeed we find, that the nonequilibrium local spectral function shows a broad spectrum at weak disorder, but exhibits sharp spikes at strong disorder (or for strong quasi-periodic potentials). The field-theoretic framework we develop can be extended beyond leading order, although higher orders are numerically intensive.

5.2 The disordered nearest-neigbor Hubbard model

We study a model of spinless fermions with nearest-neighbor interactions (i.e., a "spinless Fermi-Hubbard model")

$$\hat{H} = -J \sum_{\langle i,j \rangle} \hat{c}_i^\dagger \hat{c}_j + U \sum_{\langle i,j \rangle} \hat{n}_i \hat{n}_j + \sum_j h_j \hat{n}_j, \tag{5.1}$$

where h_i are chosen to be either uncorrelated random fields drawn from a box distribution $[-W, W]$ or a quasi-periodically varying potential. We quote results for the random case, except when otherwise specified. We fix the parameters $J = 1$, $U = 0.5$ and work with periodic boundary conditions. We investigate the model in one spatial dimension, even though our method can be readily extended to two dimensions. In one dimension and for the aforementioned set of parameters the Hamiltonian, Eq. (5.1), maps via the Jordan-Wigner transformation onto the disordered spin-$1/2$ XXZ-model at $J_z = 0.5 J_\perp$ and a reduced disorder strength $\tilde{W} = 0.5W$. The XXZ-model is a paradigmatic model in the study of many-body localization. Numerical studies based on exact diagonalization indicate a localization-delocalization transition at the critical disorder strength $\tilde{W}_c \simeq 3.6$ [147, 148].
To calculate the time evolution of the system, we use the nonequilibrium Keldysh field theory formalism [164, 165, 46]. In this approach one propagates the contour ordered Green's functions $G_{ij}(t, t') = \langle T_\mathcal{C} \hat{c}_i(t) \hat{c}_j^\dagger(t') \rangle$ on the Schwinger-Keldysh closed time contour (CTC) by solving a nonequilibrium Dyson equation. To make the CTC structure explicit, we introduce lesser and greater Green's functions, $G_{ij}^<(t, t') = i\langle \hat{c}_j^\dagger(t') \hat{c}_i(t) \rangle$ and $G_{ij}^>(t, t') = -i\langle \hat{c}_i(t) \hat{c}_j^\dagger(t') \rangle$, in which the

Dyson equations take the form

$$\Big[i\partial_t - \hat{J} + \hat{\Sigma}^{\mathrm{HF}}(t)\Big] * \hat{G}^{\lessgtr}(t,t') = \int_0^t dt''\, \hat{\Sigma}^{\mathrm{R}}(t,t'') * \hat{G}^{\lessgtr}(t'',t') + \int_0^{t'} dt''\, \hat{\Sigma}^{\lessgtr}(t,t'') * \hat{G}^{\mathrm{A}}(t'',t'). \tag{5.2}$$

Here $*$ denotes a matrix product over spatial indices i, j and $-\hat{J}_{ij} = -J\delta_{\langle i,j\rangle} + h_i\delta_{ij}$ is the sum of the hopping and onsite potential matrices. The lefthand side of Eq.(5.2) contains only terms local in time, in particular the Hartree-Fock selfenergy $\Sigma^{\mathrm{HF}}_{ij}(t)$. The righthand side on the other hand entails integrals over the entire past of the system, which incorporate memory effects in the dynamics. We expect that these time-nonlocal effects are necessary to capture full thermalization at weak disorder; however, as we shall see below, relaxation of a nonequilibrium initial state can be captured even if one neglects memory effects and takes into account only the time-local Hartree-Fock part of the self-energy, $\Sigma^{\mathrm{HF}}_{ij}(t)$. The self-consistent Hartree-Fock theory therefore maps Slater determinants to other Slater determinants, and in this sense does not give rise to full thermalization.
In the following, we focus on the nonequilibrium Dyson equation at the Hartree-Fock level,

$$\Big[i\partial_t - \hat{J} + \hat{\Sigma}^{\mathrm{HF}}(t)\Big] * \hat{G}^{\lessgtr}(t,t') = 0. \tag{5.3}$$

The selfenergy is in general given as the functional derivative of the two particle irreducible (2PI) effective action $\Gamma_2[G]$ [164] with respect to the Green's function and thus is a functional of the full Green's function, in contrast to normal perturbation theory, where one expands the self-energy in the bare Green's function. The Hartree-Fock selfenergy is obtained from an expansion of $\Gamma_2[G]$ to first order in the nearest neighbor repulsion U, such that

$$\begin{aligned}\Sigma^{\mathrm{HF}}_{mn}(t) &= \Sigma^{\mathrm{H}}_{mn}(t) + \Sigma^{\mathrm{F}}_{mn}(t) \\ &= 2U\delta_{mn}\sum_{\langle l,n\rangle} n_l(t) + 2iU\delta_{\langle m,n\rangle} G^{<}_{mn}(t,t).\end{aligned} \tag{5.4}$$

From the lesser and greater Green's functions one can obtain observables like the occupation numbers $n_j(t) = \langle \hat{n}_j(t)\rangle = -iG^{<}_{jj}(t,t)$ and also the retarded Green's function $G^{\mathrm{R}}_{ij}(t,t') = \Theta(t-t')[G^{>}_{ij}(t,t') - G^{<}_{ij}(t,t')]$.
We treat disorder in an exact way by sampling realizations from the disorder distribution, simulating the time evolution of the lesser/greater Green's functions $G^{\lessgtr}_{ij}(t,t')$ and in the end averaging the quantity of interest over the samples until convergence is achieved. Typically a few hundred samples are necessary. Therefore, no replica trick [175], as usually used in the equilibrium field theoretic treatment of disordered systems, is required.

Due to the absence of memory integrals in Eq. (5.3) at the Hartree-Fock level, we are able to treat system sizes up to 192 sites and times up to 10^4 hopping scales, which thus goes significantly beyond the state of the art of exact diagonalization in system size and matrix product state based approaches in time. Moreover, we show in App. 5.6, that our approach captures well the time evolution of small systems calculated by exact diagonalization and discuss field-theoretic results beyond Hartree-Fock in App. 5.7. Using a related framework based on quantum master equations that were derived from perturbation theory, Refs. [176, 177] studied the relaxation of disordered fermions. This approach however, does not necessarily conserve energy and the total particle number. The non-equilibrium Dyson equation (5.3) is a first order differential equation in time and one needs to fix initial conditions $G^{\lessgtr}_{ij}(0,0)$. In this work we will look at uncorrelated product initial states, which are uniquely defined by the occupations $n_j(0)$. These fix the lesser Green's functions $G^{<}_{ij}(0,0) = i\delta_{ij}n_j(0)$ and, using the anti-commutation relations of $\hat{c}_j$, $\hat{c}^\dagger_j$, also the greater Green's function $G^{>}_{ij}(0,0) = -i\delta_{ij}(1-n_j(0))$.

5.3 Relaxation of initial states

The main observable we use to study the relaxation of an initial state, is the density-density correlation function

$$\mathcal{C}(t) = \frac{2}{N}\sum_j \langle \hat{n}_j(t)\hat{n}_j(0)\rangle - 1, \tag{5.5}$$

where N is the number of fermions in the lattice. We consider half filled systems, $N = L/2$, where L is the size of the lattice. The correlation function has the property that $\mathcal{C}(t=0) = 1$. If the system is localized, i.e., the system remains in a spatially nonuniform state, $\mathcal{C}$ remains finite for all times, $\mathcal{C}(t\to\infty) \neq 0$. Instead, if the system becomes delocalized and there is a relaxation to a uniform state, the correlation function becomes zero at late times, $\mathcal{C}(t\to\infty) = 0$ [1].
As the density-density correlation, Eq. (5.5), is a four-point function, it is in general not possible to calculate it from two-point Green's functions. However, for product initial states, the four-point function reduces to a two-point function and, the lesser Green's function $G^{<}_{jj}(t,t)$ is sufficient to obtain $\mathcal{C}(t)$. For an initially staggered state, where every other site is occupied, i.e., $n_j(0) = 1$ for j even and $n_j(0) = 0$ for j odd, $\mathcal{C}(t)$ is identical to the imbalance $\mathcal{I}(t) = (N_\mathrm{e} - N_\mathrm{o})/(N_\mathrm{e} + N_\mathrm{o})$ between even and odd sites, which is often measured in optical lattice experiments [125].

[1] This is only strictly valid in the thermodynamic limit, for a finite size system $\mathcal{C}(t)$ will attain a residual value $\sim 1/L$ for late times even in the delocalized phase.

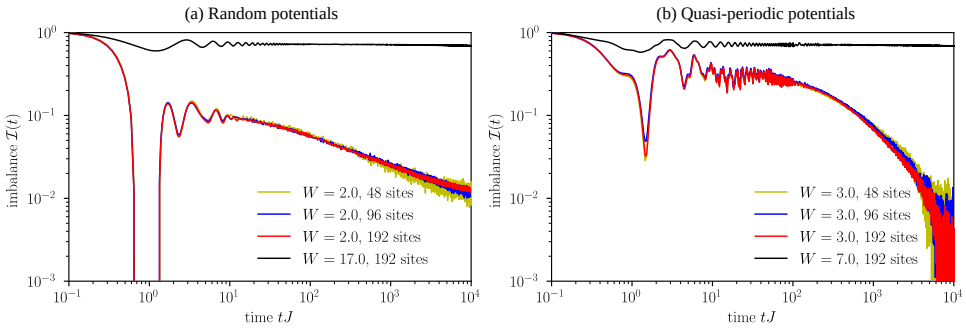

Figure 5.1: **Decay of the imbalance for a staggered initial state in one dimension for random and quasi-periodic potentials.** Initially we prepare the system in a staggered product state, where all even sites are occupied and all odd sites are empty. The time evolution of the system is obtained from the Kadanoff-Baym equations including Hartree-Fock effects of a nearest-neighbor repulsion $U = 0.5$. (a) In the case of weak disorder, $W = 2.0$ (yellow, blue, red), the imbalance $\mathcal{I} = (N_e - N_o)/(N_e + N_o)$ decays with a subdiffusive powerlaw, $\mathcal{I}(t) \sim t^{-\alpha}$, with an exponent $0 < \alpha < 1/2$. Finite size effects are still noticeable for system sizes of 96 and 192 sites and become relevant at $t \simeq 5000$. For strong disorder, $W = 17.0$, the imbalance $\mathcal{I}$ relaxes to a nonzero value indicating localization of the system (black). Finite size effects are not visible in this case (not shown). (b) For quasi-periodic disorder rare region effects are absent, as the energy mismatches between sites are always either small or large. Hence, in the case of weak disorder, $W = 3.0$, there is no subdiffusion and the imbalance $\mathcal{I}(t)$ is decaying faster than a powerlaw (yellow, blue, red). For strong disorder, $W = 7.0$, the system becomes localized (black line).

Random vs. quasi-periodic disorder

In order to study random systems, we draw the local potentials from a bounded box-distribution,

$$h_j \in [-W, W] \tag{5.6}$$

and refer to that as random disorder. However, recently many experiments have explored MBL using quasi-periodic potentials,

$$h_j = W\cos(2\pi\Phi j + \theta), \tag{5.7}$$

instead of uncorrelated randomness. Here Φ is the golden ratio and observables are averaged over several values of the phase θ. As the period of the cosine function is incommensurate with the lattice spacing, the potential looks quasi-random. Nevertheless, there are crucial differences to a truly random potential. First of all, there is already a localization transition in the one dimensional non-interacting system, commonly known as the Aubry-André model [178], at $W_c = 2$. Secondly, the detuning between neighboring sites is either always small or large throughout the whole system, depending on the value of the strength W, and hence rare regions are absent.

We first turn to the case of random disorder potentials. For weak disorder, $W = 2.0$, an initially staggered state relaxes and the imbalance decays *in random potentials* as a power law $\mathcal{I}(t) \sim t^{-\alpha}$, with an exponent α between 0 and $1/2$, Fig. 5.1(a). The powerlaw relaxation occurs due to the presence of rare region/Griffiths effects [149, 167, 171]. Griffiths effects arise due to the enclosure of non-relaxing localized regions in the otherwise delocalized system. The probability for having a localized inclusion in d dimensions is exponentially small in its size, $\sim q^{l^d}$, and the timescale for such a region to relax is exponentially long, $\sim e^{l/\xi}$, where ξ is the localization length in the inclusion. For uncorrelated disorder, it follows that the density of inclusions that are dynamically frozen on a timescale t is $q^{(\xi \log t)^d}$. In one dimension, these regions hence give rise to a residual contrast that scales as a power-law with a continuously varying exponent as disorder is tuned. In two dimensions, rare regions give rise to a faster decay of the contrast. Asymptotically, it is therefore expected that this log-normal decay should be subleading to hydrodynamic long-time tails [167].

If disorder is strong, $W = 17.0$, the system becomes localized and the imbalance $\mathcal{I}(t)$ saturates at a sizable finite value, indicating that the system keeps a memory of the initially imprinted staggered particle distribution. Deep in the localized phase there is no finite size dependence of the imbalance, because the localization length is much smaller than system size and particles do not experience the boundaries of the system. Consequently small size simulations are sufficient to observe the thermodynamic limit. On the other hand, finite size effects are considerable and still relevant even up to the order of hundreds of sites for $W = 2$.

The relaxation of the imbalance for various values of the disorder W and systems of 192 sites is shown in Fig. 5.2. Within the self-consistent Hartree-Fock theory,

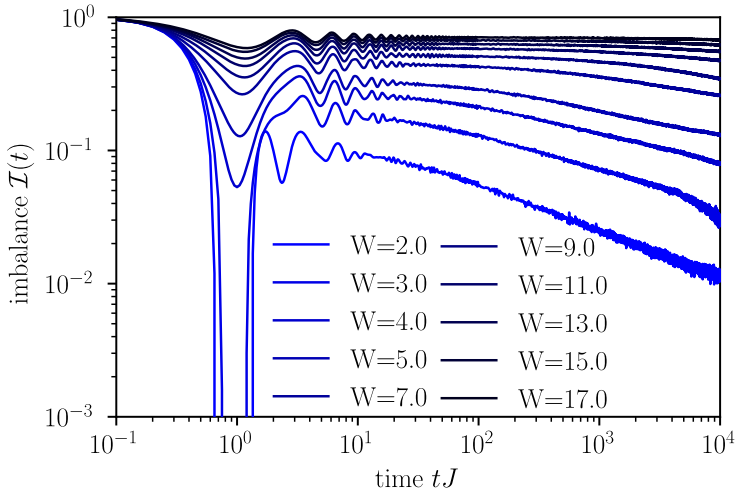

Figure 5.2: **Relaxation of the imbalance for varying disorder.** We gradually increase the disorder strength from $W = 2$ to $W = 17$ for systems of 192 sites, and monitor the relaxation dynamics of the imbalance $I(t)$ in time. Within the self-consistent Hartree-Fock approach we find that the system keeps its memory of the initial state to late times for disorder strength $W \gtrsim 15$, which corresponds to a disorder strength of $\tilde{W} \gtrsim 7.5$ in the XXZ-model.

the imbalance decays for a large parameter regime to zero with a subdiffusive power law. Only for $W \gtrsim 15$ (corresponding to $\tilde{W} \gtrsim 7.5$ in the XXZ-model), the imbalance ceases to relax on the simulated times. We argue in Sec. 5.5 for the existence of a true localization transition within our approximations, which would thus be at significantly larger disorder strength than the one obtained from small scale numerics, which has been estimated to be at $\tilde{W} \sim 3.6$ for our system [147, 140, 141, 148]. Note that previous large-system studies using the numerical linked-cluster approach [179] and a recent study using matrix product states [180] had also located the transition at much stronger disorder.

With quasi-periodic potentials we again find that including interactions at the Hartree-Fock level leads to a relaxation of the initially imprinted density pattern for weak disorder, $W = 3.0$, Fig.5.1(b). Yet, due to the strong spatial correlations of the quasi-periodic disorder, rare region effects are absent and our numerics does not show subdiffusive power-law decay of the imbalance. This is in contrast to a tDMRG and renormalization group study, which is however limited to shorter time scales [173]. Due to the fast decay one can still see the residual finite size value of $\mathcal{I}(t)$ even for system sizes of 192 sites at late times.

Note, that in the absence of interactions, the localization length $\xi \sim 1.2$ of the model with quasi-periodic disorder at $W = 3.0$ is significantly shorter than that of the model with random disorder at $W = 2.0$ ($\xi \sim 4.0$). Yet the imbalance decays much faster for quasi-periodic disorder, therefor we can expect, that the absence of a subdiffusive powerlaw decay is a genuine effect of the type of the disorder

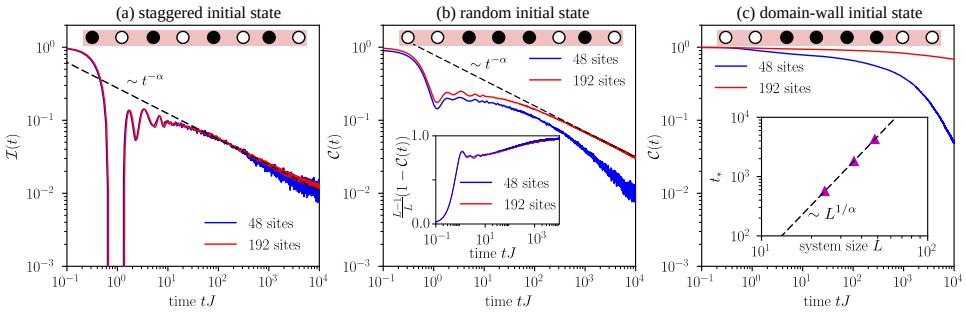

Figure 5.3: **Subdiffusive decay of different initial states for random disorder potentials.** We prepare the system in three different initial states, in a staggered initial state (a) where every other site is occupied, in a random initial state (b) where half of the sites are occupied at random positions, and in a domain-wall state (c) where a chain of length $L/2$ in the middle of the system is occupied with fermions. The states are depicted schematically at the top of each panel. In the case of a staggered initial state the density-density correlation function $\mathcal{C}(t)$ reduces to the imbalance $\mathcal{I}(t)$. (a) The staggered initial state shows the fastest relaxation and the imbalance decays according to a subdiffusive powerlaw $\mathcal{I}(t) \sim t^{-\alpha}$. (For the disorder strength shown, $\alpha = 0.351$). (b) Relaxation is slower for random initial states as they typically contain small blocks of occupied sites, which relax slowly due to the Pauli principle. For late times however the density-density correlation approaches the same subdiffusive powerlaw $\mathcal{C}(t) \sim t^{-\alpha}$ as the staggered initial state. To see this, large system sizes of several hundreds sites are required. The inset shows the proper short time finite size scaling of the correlation function. (c) The domain-wall initial state is slowest to relax due to the Pauli principle blocking hopping inside the block. The timescale t_* for melting the block, reminiscent of the Thouless time in diffusive systems, shows the scaling $t_* \sim L^{1/\alpha}$ with system size (inset), consistent with the presence of subdiffusive transport in the system. All graphs are shown for nearest neighbor repulsion $U = 0.5$ and disorder strength $W = 2.0$.

potential, rather than a mere disorder strength effect.
Increasing the disorder strength, the system localizes at weaker potential strength than in the case of a true random potential; it is already fully localized for $W = 7.0$. This is consistent with the intuitive picture of energy mismatches between sites becoming large everywhere without any statistical fluctuations.

Initial-state dependence

Besides the staggered state we also consider random initial states, where the initially occupied sites are chosen randomly as well as a domain-wall initial state where a block of $L/2$ sites in the middle of the system is initially occupied. In Fig. 5.3 we compare for *random disorder* the relaxation of the three type of initial states (staggered, random, and domain wall). From a coarse-grained, hydrodynamic point of view, these three types of initial states differ in that the staggered state is dominated by high-momentum fluctuations, the domain-wall initial state has exclusively low-momentum fluctuations, and the random state has fluctuations at all scales. As expected on general hydrodynamic grounds, therefore, the domain-wall state is much slower to relax than the staggered state: the timescale on which it relaxes can be interpreted as the Thouless time for the system.
The decay time scales of random initial states, Fig. 5.3(b), is in between the staggered initial state, (a) and the block initial state, (c). For random initial states, the density-density correlation $\mathcal{C}(t)$ is not only averaged over disorder realizations but also over different initial particle distributions, such that this case can be interpreted as the result for an infinite temperature ensemble. For large system sizes of 192 sites, the decay of $\mathcal{C}(t)$ approaches the same power-law decay $\sim t^{-\alpha}$ as the imbalance in the case of a staggered initial state at late times. This behavior is not observable for smaller systems, which in particular implies that numerics for small system sizes is not sufficient to study the power law relaxation in that observable.
To further corroborate the observation of subdiffusive particle transport in the system at weak disorder, we analyze the finite size scaling of the crossover timescale t_*, at which the block initial state starts to decay, see Fig. 5.3(c) (inset). For concreteness we define $t_\star$ as the time where $\mathcal{C}(t)$ has dropped to $1/(2e)$, though we have checked, that the scaling is insensitive to this specific choice. In a diffusive system the notion of $t_\star$ would be equivalent to the Thouless time t_{Th}, which scales quadratically with system size, $t_{\mathrm{Th}} \sim L^2$. For subdiffusive transport we find a steeper power law $t_* \sim L^{1/\alpha}$, where α is the exponent of the imbalance decay. The two exponents coincide, at least within the Hartree-Fock theory, because the timescale governing density relaxation across the system is the relaxation timescale of the slowest bottleneck expected in a system of size L. This slowest bottleneck should correspond to a Griffiths region with density $1/L$. Given that the density of a Griffiths region with timescale t scales as $1/t^\alpha$, we thus have that $t_* \sim L^{1/\alpha}$ (dashed line in the inset of Fig. 5.3 (c)). Our numerics yields a very good agreement of these two exponents, see Fig. 5.3(a) and (c)
Looking at panels (b) and (c) of Fig. 5.3, it can be seen, that finite size effects be-

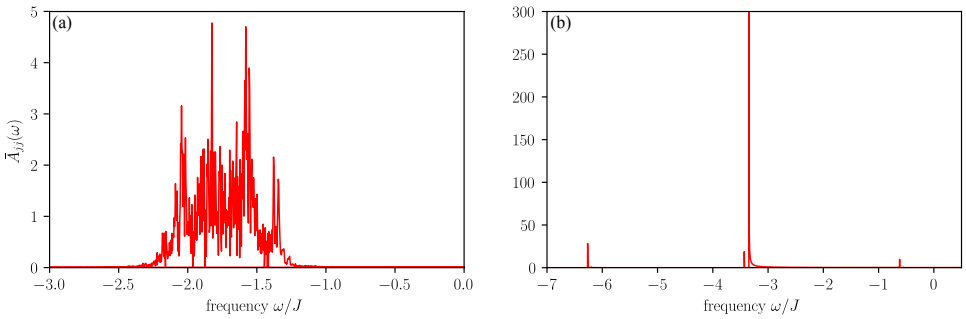

Figure 5.4: **Nonequilibrium local spectral function for a single disorder realization.** Averaging the nonequilibrium spectral function $A_{jj}(T,\omega)$ over the center-of-mass time T extracts the non-negative, non-oscillatory part $\bar{A}_{jj}(\omega)$, which can be interpreted analogously to the usual equilibrium spectral function. (a) For weak disorder, $W = 2.0$, the local spectral function $\bar{A}_{jj}(\omega)$ has a broad support and hence there is a finite energy window in which fermions can tunnel into/out of the site. This leads to the delocalization of the system. (b) In the case of strong disorder, $W = 17.0$, $\bar{A}_{jj}(\omega)$ has sharp delta spikes only for a finite set of frequencies, thus only fermions with energies from a set of measure zero can hop into or out of the site. Accordingly the system becomes localized. It is crucial to look at single sites and a single disorder realization, as averaging over either lattice sites or disorder would yield a sum of delta peaks which smears out the spectral function.

come noticeable already at $tJ \sim 1$ for a random or block initial state, while they only become relevant at late times for a staggered initial state, Fig. 5.3(a). This feature follows from the definition of $\mathcal{C}(t)$: for a staggered initial state, local relaxation takes place everywhere in the system at once, so the system-wide imbalance drops at a rate of order unity; but for a domain-wall initial state, all the relaxation takes place at the boundary, so the system-wide imbalance drops at a rate $O(1/L)$. The random initial state is, again, in between the two cases. Calculating the average number of domain walls for a chain of length L and periodic boundary conditions, as $\frac{L}{2}\left(1+\frac{L-4(N-L/2)^2}{L(L-1)}\right)$, we can remove the short time finite size effect, by properly rescaling the measured correlation function $\mathcal{C}(t)$, see inset of Fig. 5.3(b).

5.4 Spectral information

A useful quantity in the study of many-body localization is the local spectral function, defined as the imaginary part of the retarded Green's function, $A_{jj}(T,\omega) = -1/\pi\ \mathrm{Im}G^{\mathrm{R}}_{jj}(T,\omega)$. Here, $T = (t+t')/2$ is the so called center-of-mass time and the Fourier transform to frequency space ω is calculated with respect to the relative time $t_{\mathrm{rel}} = t - t'$. In a full nonequilibrium setting, Green's functions do

not only depend on the time difference t_{rel} but also on the absolute center-of-mass time T. Nonetheless, we will show in the following, that one can still extract similar information as in equilibrium.
Using the Lehmann representation assuming a nonequilibrium initial state, $A_{jj}(T,\omega)$ can be decomposed as

$$\begin{aligned} A_{jj}(T,\omega) &= \bar{A}_{jj}(\omega) + R_{jj}(T,\omega) \\ \bar{A}_{jj}(\omega) &= \sum_{n,m} |\psi_n|^2 \{ |C^{(j)}_{nm}|^2 \delta(\omega - \epsilon_{nm}) + n \leftrightarrow m \}, \end{aligned} \tag{5.8}$$

where $\psi_n = \langle n|\psi\rangle$, $C^{(j)}_{nm} = \langle n|\hat{c}_j|m\rangle$, $|n\rangle$ are the exact many-body eigenstates of the system, and ϵ_{nm} are the levelspacings between eigenenergies. The second term in the decomposition,

$$\begin{aligned} R_{jj}(T,\omega) = \sum_{m,n\neq l} \Bigg\{ & \mathrm{Re}[a^{(j)}_{mnl}(T)]\delta\left(\omega - E_m + \frac{E_n+E_l}{2}\right) \\ & + \mathrm{Re}[a^{(j)}_{mln}(T)]\delta\left(\omega + E_m - \frac{E_n+E_l}{2}\right) \\ & + \frac{1}{\pi}\mathrm{Im}[a^{(j)}_{mnl}(T)]\frac{1}{\omega - E_m + \frac{E_n+E_l}{2}} \\ & - \frac{1}{\pi}\mathrm{Im}[a^{(j)}_{mln}(T)]\frac{1}{\omega + E_m - \frac{E_n+E_l}{2}} \Bigg\}, \end{aligned} \tag{5.9}$$

contains all the dependence on center-of-mass time via the time-dependent coefficients $a^{(j)}_{mnl}(T) = e^{-i\epsilon_{nl}T}\psi^*_n\psi_l C^{(j)}_{nm}C^{(j)*}_{lm}$. Due to these oscillatory contributions, $R_{jj}(T,\omega)$ can become negative, which invalidates the positivity sum rule of the equilibrium spectral function. In contrast to the equilibrium spectral function, out of equilibrium $A_{jj}(T,\omega)$ also shows $1/\omega$ divergences due to the contribution of $R_{jj}(T,\omega)$, which would appear only in the real part of an equilibrium Green's function. By contrast, $\bar{A}_{jj}(\omega)$, which we will refer to as local spectral function in the following, has a form similar to an equilibrium spectral function. It is independent of the center-of-mass time T, nonnegative, and a weighted sum of δ-functions located at spectral lines $E_n - E_m$ of the system. One can obtain $\bar{A}_{jj}(\omega)$ from $A_{jj}(T,\omega)$ by averaging over center-of-mass time, $\bar{A}_{jj}(\omega) = \lim_{T\to\infty} T^{-1}\int_0^T dS\ A_{jj}(S,\omega)$ as the average will cancel the oscillatory terms in $A_{jj}(T,\omega)$.
Physically the local spectral function $\bar{A}_{jj}(\omega)$, is interpreted as the amplitude for a fermion with energy ω tunneling into or out of lattice site j. If disorder is weak and the system is delocalized, the local spectral function is finite for a continuous set of frequencies such that fermions with many different energies are able to tunnel into or out of a given site, see Fig. 5.4(a). In contrast, in the localized phase hopping into or out of a given site is only possible for fermions with a discrete set of energies, hence the local spectral function has only discrete sharp spectral lines, see Fig. 5.4(b).

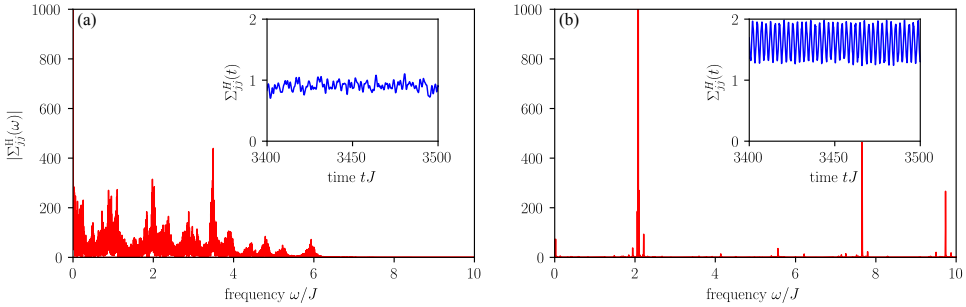

Figure 5.5: **Self-consistent noise interpretation of the Hartree selfenergy.** Delocalization in our system on the Hartree-Fock level can be understood by interpreting the Hartree-Fock self-energy $\Sigma^{\mathrm{HF}}_{ij}(t)$ as noise. Since $\Sigma^{\mathrm{HF}}_{ij}(t)$ is a functional of the Green's function, the noise is self-consistently generated by the system itself and hence it does not necessarily lead to relaxation. (a) The amplitude spectrum $|\Sigma^{\mathrm{H}}_{jj}(\omega)|$ of the Hartree selfenergy shows mixing of a continuous frequency range without any to prominent features for weak disorder, $W = 2.0$. In the time domain, $\Sigma^{\mathrm{H}}_{jj}(t)$ therefor looks like noise (inset) and consequently the system delocalizes. On the other hand, for strong disorder $W = 17.0$ (b), the amplitude spectrum only shows mixing of a discrete number of frequencies. Thus, $\Sigma^{\mathrm{H}}_{jj}(t)$ oscillates coherently in the time domain (inset) and the system remains localized. All data is shown for systems of size L=96.

As one is limited to a finite time evolution in numerics we average over center-of-mass times in the range $1000 \leq TJ \leq 7313$. Despite this already large averaging window, there are still some artifacts, like zero-crossings and $1/\omega$-singularities, of the T-dependent part $A_{jj}(T, \omega)$ visible in Fig. 5.4(b). This is due to the presence of oscillations with very long period, or in other words very close energy levels, which naturally appear in localized systems due to the absence of level repulsion.

5.5 A self-consistent noise interpretation

It is often assumed, that treating interactions at Hartree-Fock level is not sufficient to witness the breakdown of localization in a disordered system [8]. While this is true in thermal equilibrium, as we show in Sec. 5.3 this assumption does not hold in the case of quench dynamics that is considered here. The essential mechanism by which Hartree-Fock terms cause delocalization is as follows: the time-dependent Hartree-Fock potentials act as effective temporal noise, and a noninteracting system subject to noise will thermalize (though potentially with transient subdiffusive dynamics [181]). Intuitively, this can be understood as the noise process, with its continuous frequency spectrum, providing the missing energy for a fermion to hop between two energy-detuned sites. We also show in App. 5.8, that relaxation at

weak randomness is not due to dephasing effects between different disorder samples or due to averaging over different lattice sites, by computing the relaxation of the local density at single sites and for single disorder configurations.
In our Hartree-Fock theory the selfenergy $\Sigma_{ij}^{\mathrm{HF}}(t)$ is a deterministic function for a given disorder sample and a given initial state. However, its frequency spectrum can still potentially be broad, allowing for transitions between energy-detuned single-particle orbitals. To analyze this we compute the amplitude spectrum of the Hartree-Fock selfenergy $|\Sigma_{ij}^{\mathrm{HF}}(\omega)|$ for a single realization of the disorder. As the results are very similar for both the Hartree and the Fock contribution (see App. 5.9), we will focus on the amplitude spectrum of the Hartree selfenergy $|\Sigma_{jj}^{\mathrm{H}}(\omega)|$ only. If the amplitude spectrum is broad and mostly featureless as for disorder strength $W = 2.0$ in Fig. 5.5(a), the self-energy will look like noise in time domain, leading to delocalization (inset). When the amplitude spectrum consists only of a discrete set of sharp peaks, as is the case for strong disorder $W = 17.0$, Fig. 5.5 (b), the Hartree selfenergy is just a coherent oscillation in time (inset), leaving localization intact.
These numerical findings are consistent with what one might expect perturbatively, at weak interactions. A single lattice site overlaps with $\sim \xi$ single-particle orbitals, each at a different energy, and therefore the on-site potential fluctuates at $\sim \xi$ separate oscillation frequencies. At the same time, the energy detuning between a particular orbital and the others it overlaps with goes as $\delta_\xi \sim 1/\xi^2$ (or, more generally, polynomially in $1/\xi$). Thus, when $\xi \gg 1$, a particle in a given orbital is driven at enough different frequencies that it is likely to find a "noise"-induced resonant transition to another orbital. These transitions lead to yet more frequencies in the self-energy spectrum, inducing yet more transitions, and so forth, and eventually all particles delocalize. In the opposite limit, $\xi \ll 1$, the same logic indicates that localization is stable. In that limit, the amplitude of the Hartree self-energy at a typical site falls off as $\exp(-1/\xi)$ (from orbitals centered at nearest-neighbor sites; further orbitals are exponentially suppressed as $\exp(-L/\xi)$ [182]). For the same reason, a typical orbital has exponentially weak matrix elements to couple to any other orbitals. Thus, asymptotically, in this limit each orbital is subject to a weak, essentially time-periodic potential, which does not induce resonances, leading to a stable localized regime within this approximation.
We now calculate the autocorrelation function $\overline{\Sigma_{jj}^{\mathrm{H}}(t)\Sigma_{jj}^{\mathrm{H}}(0)}$ via averaging over disorder realizations, Fig. 5.6. We find that the autocorrelations show a decay which is consistent with a slow powerlaw $\overline{\Sigma_{jj}^{\mathrm{H}}(t)\Sigma_{jj}^{\mathrm{H}}(0)} \sim t^{-\beta}$ in the delocalized phase, $W = 2.0$. These noise correlations are much longer lived than in Ref. [181], where exponential correlations have been studied. However, when one repeats the arguments therein with power-law correlated noise, it turns out that the distribution of tunneling times is still fat tailed and hence subdiffusive transport is recovered in the system, which is consistent with our numerical observations. In contrast, for strong disorder, $W = 17.0$, the self-energy autocorrelations remain constant in time.
Despite the similarities between our Hartree-Fock treatment and Ref. [181], there

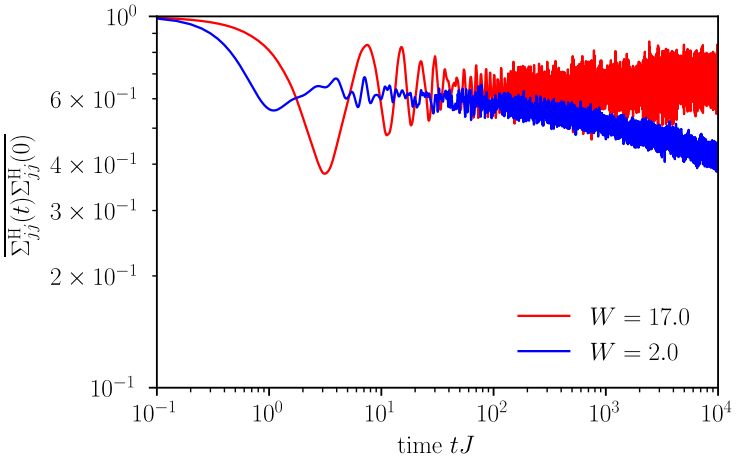

Figure 5.6: **Autocorrelation of the Hartree selfenergy.** We compute the autocorrelation $\overline{\Sigma^{\mathrm{H}}_{jj}(t)\Sigma^{\mathrm{H}}_{jj}(0)}$ of the Hartree selfenergy averaged over disorder realizations for systems of size L=96. The autocorrelation of $\Sigma^{\mathrm{H}}_{jj}(t)$ shows a decay in time, consistent with a slow powerlaw, when the disorder is weak, $W = 2.0$ (blue). One can therefore think of $\Sigma^{\mathrm{H}}_{jj}(t)$ as powerlaw correlated noise in a zeroth order approximation. In the localized phase, $W = 17.0$, the Hartree selfenergy shows non-decaying autocorrelations for all times (red).

are still some differences. Most importantly, the noise is generated self-consistently, so its strength is in general not constant in time. The distribution of $\Sigma^{\mathrm{HF}}_{ij}(t)$, obtained from disorder sampling is furthermore non-Gaussian. We expect that these differences lead to quantitative changes in the dynamics, which need to be addressed in more detailed, future investigations.

5.6 Comparison of Hartree-Fock with exact diagonalization

For small systems of 12 sites we compare the imbalance time-traces obtained from our Hartree-Fock approach to exact-diagonalization calculations in order to get a quantitative benchmark for our method. In the weak-disorder regime, Hartree-Fock tends to be more delocalizing, see Fig. 5.7. In the strong disorder limit, however, our method is in good quantitative agreement with exact diagonalization. The deviations at weak disorder stem on the one hand from neglecting higher order contributions to the self-energy and on the other hand from the fact that field theories have the tendency to mimic larger systems and hence provide results that are more delocalized compared to exact diagonalization.

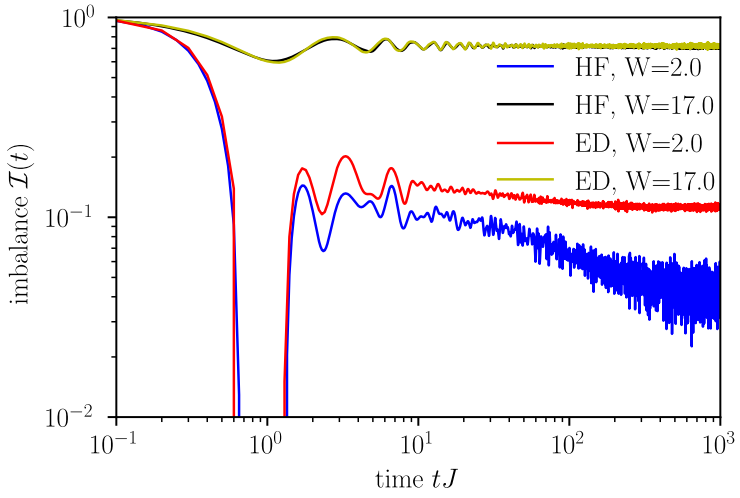

Figure 5.7: **Comparison between Hartree-Fock and exact diagonalization**. We compare the Hartree-Fock (HF) theory with exact diagonalization (ED) for small systems of 12 sites at weak disorder, $W = 2.0$, where HF delocalizes faster than ED, and at strong disorder, $W = 17.0$, where both are practically lying on top of each other. The faster decay of the HF time trace compared to ED for weak disorder can be first attributed to the fact that interactions are treated only perturbatively and second because field theories are not very sensitive to finite size effects.

5.7 Self-consistent Born approximation

The next-to-leading order contribution to the self-energy in our weak coupling expansion is often referred to as self-consistent Born approximation (SCBA), which is of second order in the interaction U. We calculate the SCBA contribution to the selfenergy and obtain

$$\Sigma_{ij}^{\mathrm{SCB}}(t,t') = 8G_{ij}(t,t')\sum_{lk} U_{ik}U_{lj}G_{kl}(t,t')G_{kl}(t',t). \tag{5.10}$$

We evaluate the Dyson equation taking self-energy contribution up to the SCBA and compute the time averaged correlation function for a staggered initial state and a domain wall initial state, see Fig. 5.8. Within the SCBA it is numerically expensive to reach late times, because the memory integrals on the right hand side of the Dyson equation (5.2) have to be computed. Therefore, our data is limited to times $tJ \sim 20$.
Hartree-Fock is overall consistent with SCBA, but the latter potentially delocalizes the system slightly less, at least on the accessible time scales. On the one hand, SCBA adds new decay channels to the dynamics which on the first sight should enhance delocalization, but on the other hand it might also decrease the self-consistent noise because the memory integral in the Dyson equation damps oscillations.
One possible scenario could be, that the second effect (weaker noise due to damping of oscillations) dominates at short times, before the first effect (larger number of decay channels) takes over at later times, as the SCBA contributions in Eq. (5.2) may build up slowly over time. Similar behavior has been found in the NLO dynamics of the $O(N)$ [183, 184, 185, 186].

5.8 Single samples and single sites

It is well established, that the nonequilibrium Keldysh 2PI approach is able to describe thermalization in a closed system. This is, however, only true, when the memory integrals on the right hand side of Eq. (5.2), i.e., the time non-local parts of the selfenergy, are included. The Hartree-Fock selfenergy on its own does not lead to thermalization. Nevertheless we have shown in our present work, that a pure Hartree-Fock time-evolution is already able to describe *relaxation* due to interaction effects in a disordered system. Just by looking at the decay of the imbalance or the density-density correlation of an initial state in Sec. 5.3, it is unclear whether this decay is only due to dephasing effects between different disorder samples and different lattice sites or true delocalization. In principle, this scenario can already be discarded by our results for the local spectral function in Sec. 5.4, which we computed for a single disorder realization. To further substantiate that the decay of the correlation functions is due to particle transport, we look at the occupation number $n_j(t)$ of a single site and a single disorder realization. In a delocalizing system, the

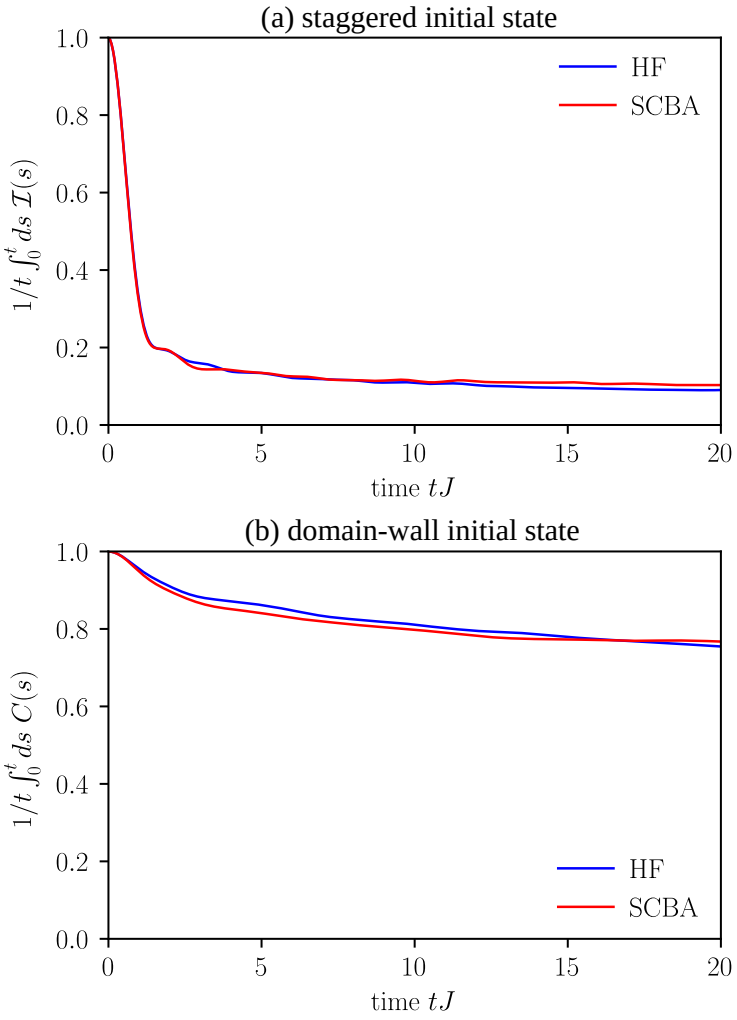

Figure 5.8: **Comparison of Hartree-Fock and SCBA at short times.** We compare the leading order Hartree-Fock dynamics with the nex-to-leading order self-consistent Born approximation, both for the (a) staggered and the (b) domain-wall initial state. The data shown is for a single disorder realization and a system size of $L = 48$

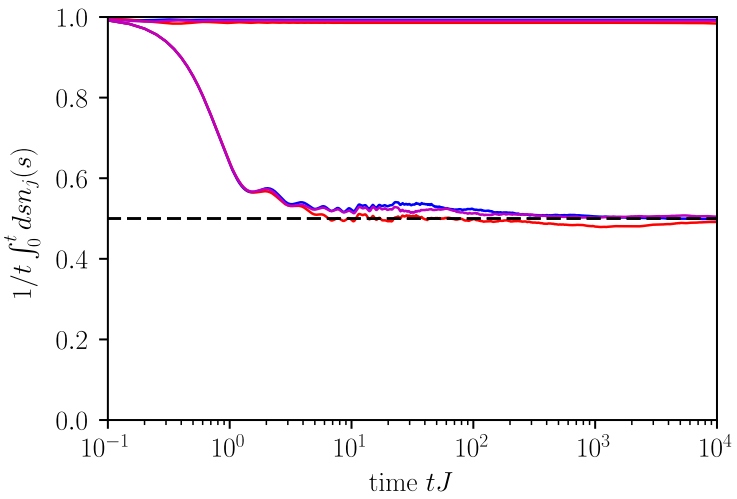

Figure 5.9: **Relaxation of an initially occupied site for a single disorder realization.** To verify that the decay of the density-density correlation is not due to dephasing or averaging effects, we compute the time averaged occupation on a single site and for a single disorder realization. For weak disorder, $W = 2.0$, (lower curves) this quantity decays to the average density of a half-filled lattice. By contrast, for strong disorder, $W = 17.0$, Without time averaging, $n_j(t)$ would be persistently oscillating about $1/2$ at late times. Therefor the decay of the imbalance $\mathcal{I}(t)$ or in general the correlation function $\mathcal{C}(t)$ is due to particle transport. For strong disorder, $W = 17.0$, the particle number does not decay on an initially occupied site, indicating localization of particles on the given site.

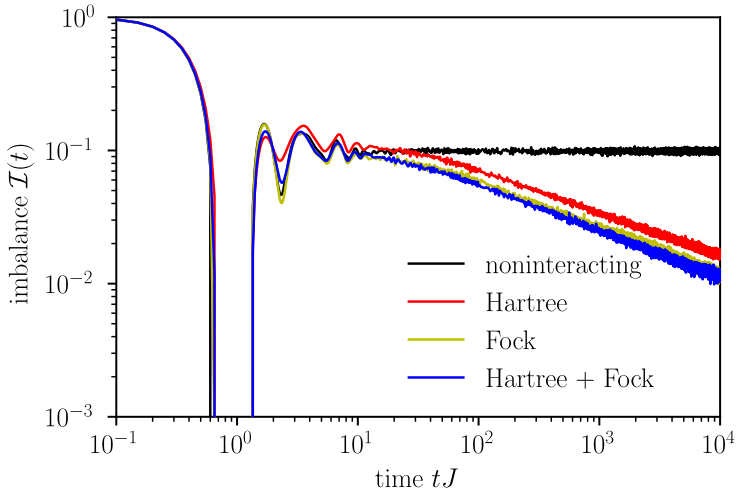

Figure 5.10: **Comparison between Hartree, Fock, and Hartree-Fock time evolution**. The time evolution of only Hartree (red), only Fock (yellow), and both Hartree and Fock (blue) is qualitatively similar. The time evolution is shown for random potentials of strength $W = 2.0$ in the subdiffusive phase and are compared to the localized, non-interacting system with the same disorder (black).

single-site occupation number will approach $1/2$ for late times, $n_j(t \to \infty) = 1/2$. On the Hartree-Fock level $n_j(t)$ contains oscillations which will persist forever and delocalization corresponds to these oscillations being centered around $1/2$. Decay of oscillations can only be obtained in higher order in the interaction and is a true many-particle effect. In order to remove the oscillations, we compute the time averaged occupations, $\lim_{t\to\infty} \frac{1}{t} \int_0^t ds\, n_j(s) = 1/2$, which smoothly approach $1/2$ at late times when the system delocalizes. That can be observed in Fig. 5.9, where we show that the time-averaged occupation number on a single site approaches $1/2$ for a few different disorder samples at weak disorder. For strong disorder the occupation remains close to its initial value, Fig. 5.9 as expected for a many-body localized system.

5.9 Analysis of the Hartree and Fock contributions

In Sec. 5.5, we have focused on analyzing the Hartree self-energy. In Fig. 5.10 we show, that the time evolution, when taking into account only Hartree, only Fock, or both Hartree and Fock contributions, are qualitatively similar. This is why it is sufficient to focus on the Hartree selfenergy, $\Sigma^{\mathrm{H}}_{jj}(t)$, when we analyzing the self-consistent noise.

5.10 Conclusions

In this work, we developed a self-consistent Hartree-Fock approach in the framework of the nonequilibrium Keldysh field theory to study interacting and disordered fermions, initialized in a far-from-equilibrium state. Our results show that this approach can capture a lot of the phenomenology of many-body localization. Using this technique, we study the time-evolution of systems of up to 192 lattice sites to times $10^4/J$. With that we can treat systems that are much larger than the ones accessible in exact diagonalization and study dynamics to times much longer than the ones accessible with matrix product states. Moreover, our results also indicate that near the many-body localization transition finite size effects are strong, and for certain observables systems of several hundreds of sites are required to obtain the asymptotic behavior.

The self-consistent Hartree-Fock approach is sensitive to rare-regions and therefore captures subdiffusive transport for weak random disorder. We showed that in correlated quasi-periodic potentials such subdiffusive transport does not exist, as can be understood from the absence of rare regions. The delocalization of our system on the Hartree-Fock level for weak disorder results from the dynamical nature of the self-energy, which we interpret as noise. For strong disorder, only a couple of frequencies contribute to the self-energy, and hence localization persists.

From a certain perspective it is surprising that Hartree-Fock theory is able to capture so much of the MBL phenomenology. This appears to have to do with our far-from-equilibrium initial state, which (together with the randomness) builds in fluctuations at many frequencies into the initial conditions for the Hartree-Fock dynamics. If we had instead started with an eigenstate of the noninteracting problem [8, 176] the Hartree-Fock theory would not give rise to thermalization, at least for weak interactions. The fact that the performance of mean-field approaches is sensitive to the fluctuations encoded in the initial state—as we see here—was recently pointed out in Ref. [187].

For future work, it will be interesting to study many-body localization in higher dimension and the effects of long-range interactions on the many-body localization transition with this approach and with that explore many-body localization in trapped ions [127], polar molecules [188], or condensed matter systems with dipolar interactions [134]. Moreover, many-body localized systems that are subjected to periodic driving fields [130] can be explored as well with this technique for large system sizes. From a more fundamental point of view, it would intriguing to investigate how one can use measures of the "spikiness" of the local spectral function to quantify the many-body localization transition, how they can be measured in ARPES type experiments for ultracold atoms [189], and whether these measures are consistent with the long-time evolution of the system.

Chapter 6

Using bipartite fluctuations to dynamically characterize a Luttinger Liquid

6.1 Connection between bipartite fluctuations and entanglement entropy in equilibrium

Entanglement has become of central interest in the study of quantum many-body systems [190, 191, 192, 193]. It is one of the hallmark features of quantum mechanics and especially relevant at low energies. For instance it can be used to distinguish phases of matter, for which no classification in terms of symmetry and local order parameter can be given, such as topologically ordered states [194, 195, 196].
The typical measures to quantify entanglement, are the von Neumann entanglement entropy or the n-Rényi entropies. In order to define these measures, one splits a system into two disjunct parts A and B and looks at the reduced density matrix $\hat{\rho}_A = \mathrm{tr}_B \left|\Psi\right\rangle\left\langle\Psi\right|$, for a given quantum state $\left|\Psi\right\rangle$. Then

$$\begin{aligned} S_{\mathrm{vN}} &= -\,\mathrm{tr}_A\{\hat{\rho}_A \log \hat{\rho}_A\} \\ H_n &= \frac{1}{1-n} \log \mathrm{tr}_A\, \hat{\rho}_A^n. \end{aligned} \tag{6.1}$$

Eq. (6.1) already shows, that obtaining the entanglement entropy is exponentially hard in general, as it requires knowledge of the whole density matrix of subsystem A. This holds true both in theory, where one usually has to rely on extensive numerics, and especially in experiment, where it has been only recently achieved to measure the second Rényi entropy in a small system of bosonic atoms in an optical lattice [197, 198, 135].
Due to these practical difficulties there have been studies, whether one can find alternative ways to quantify entanglement, without the need of having access to the reduced density matrix $\hat{\rho}_A$ [199, 200]. The basic idea is, that at least in systems with short-range interactions and well defined quasi-particle excitations, entanglement is mainly created by particles or, more generally, conserved charges crossing the boundary between subsystems A and B. Thus information about the entanglement entropy could be extracted from the full counting statistics of the charge/particle number in subsystem A.
For free fermions it has been indeed shown, that the von Neumann and Rényi entropies can be expressed in terms of an asymptotic series of the cumulants of the

particle number statistics in subsystem A [201, 202, 199, 200].
Another example, where entanglement entropy and particle number statistics are closely related, are conformal field theories (CFTs) and in particular Luttinger liquids. This is very interesting, as the low-energy properties of many one dimensional systems are captured by Luttinger liquid theory [51, 52, 203].
In a Luttinger liquid the entanglement entropy grows logarithmically in the subsystem size l [190, 192, 204, 205]

$$S_{\mathrm{vN}}(l) = \frac{1}{3}\log l + const.. \tag{6.2}$$

The particle number fluctuations $\mathcal{F}(l) = \langle \hat{N}_A^2 \rangle - \langle \hat{N}_A \rangle^2$ in the subsystem behave in the same way [200],

$$\mathcal{F}(l) = \frac{K}{\pi^2}\log l + const., \tag{6.3}$$

the only difference being the factor in front of the logarithm, which is essentially given by the so called Luttinger parameter K. The number fluctuations $\mathcal{F}$ are exactly the second and in fact the only non-vanishing cumulant in a Luttinger liquid. Therefor, in equilibrium, the entanglement in a Luttinger liquid can be quantified by particle number fluctuations, a quantity, which can be accessed significantly easier both in theory [206, 207] and experiment [208, 209, 210, 37, 211].
We study, whether the close relation between entanglement and particle number fluctuations in a Luttinger liquid also persists in a non-equilibrium setting. Concretely, we will look at the quantum dynamics after a quench from a gapped state into a Luttinger liquid and calculate the full counting statistics of the particle number in a subsystem in terms of the cumulant generating function.
We will show that, also in nonequilibrium, the fluctuations behave very similar to the entanglement entropy: After a quench, fluctuations grow linearly in time before saturating to a value that is extensive in subsystem size, after a time that is extensive in subsystem size. The only difference being the rate of the linear growth, which is universal for the entanglement entropy, while it depends linearly on the Luttinger parameter K for fluctuations.
As a quantum quench creates a highly excited state, we will use matrix product state simulations of the Bose-Hubbard model at unit filling to check whether our Luttinger liquid calculation can be expected to hold in a real system.
In addition, we will use these result, to propose a novel measurement procedure for the Luttinger parameter K, which thus far has proven to be very difficult to extract from experiments.

6.2 Quench from the Mott-insulator to a superfluid in the one dimensional Bose-Hubbard model

We want to study quenches from the Mott insulating to the superfluid phase in the one dimensional Bose-Hubbard model

$$H = -J\sum_i (b_i^\dagger b_{i+1} + b_{i+1}^\dagger b_i) + \frac{U}{2}\sum n_i(n_i - 1) \tag{6.4}$$

at half filling. The 1D Bose-Hubbard model at unit density, Eq. (6.4), displays a quantum phase transition from a Mott-insulator to a superfluid at the critical value $(J/U)_c \approx 0.3$ [212, 213, 214, 215].
Using the language of Bosonization the 1D Bose-Hubbard model can be mapped to a sine - Gordon-Model [52]

$$H_{SG} = \frac{v}{2}\int_x \left[K\pi\Pi^2(x) + \frac{1}{K\pi}(\partial_x\phi(x))^2 - 4\frac{\tilde{\Delta}}{v}\cos(\sqrt{2}\phi(x))\right]. \tag{6.5}$$

Here v is the velocity of sound waves, K the Luttinger parameter and $\tilde{\Delta}$ is a parameter stemming from the lattice depth of the optical lattice. The density operator for original bosons can be expressed in terms of the scalar field ϕ

$$\rho(x) = \rho_0 + \frac{1}{\pi}\partial_x\phi(x), \tag{6.6}$$

where ρ_0 is the average density and the second term describes density fluctuations. Using a renormalisation group analysis, one can show that the cosine term in Eq. (6.5) is irrelevant for $K > 2$ and relevant for $K < 2$, hence $K_c = 2$ marks the critical point between the gapped phase at $K < 2$ and the superfluid phase for $K > 2$. The full relation between K and J/U is not known, analytically only the following three reference points are known: $K = 1 \leftrightarrow J/U = 0$, $K = \infty \leftrightarrow J/U = \infty$ and $K = 2 \leftrightarrow (J/U)_c \approx 0.3$.
In the superfluid phase ($K > 2$) we can safely neglect the cosine term and see, that the low-energy properties of Eq. (6.4) are captured by a Luttinger-liquid. Deep in the Mott-insulating phase $(K < 2)$ we can assume, that the field amplitude ϕ is small, $\phi \ll 1$, such that we can expand the cosine term to order $\mathcal{O}(\phi^2)$, which leaves us with the theory of a massive scalar field. This reasoning justifies the choice of pre- and post-quench Hamiltonians in the following.
As we want to consider a quantum quench from a gapped phase into a Luttinger liquid (LL), the system is initially assumed to be in the ground state of the Hamiltonian

$$H_0 = \frac{\tilde{v}}{2}\int_x \left[\tilde{K}\pi\Pi^2(x) + \frac{1}{\tilde{K}\pi}(\partial_x\phi)^2 + m^2\phi^2\right]. \tag{6.7}$$

At time $t = 0$ the system is quenched into the gapless phase, described by a Luttinger liquid Hamiltonian with Luttinger parameter K and sound velocity v; thus for $t > 0$,

$$H = \frac{v}{2}\int_x \left[K\pi\Pi^2(x) + \frac{1}{K\pi}(\partial_x\phi)^2\right]. \tag{6.8}$$

In both H_0 and H, ϕ is a real scalar field and $\Pi = \partial_t \phi$ is the conjugate momentum. They obey the canonical commutation relation $[\phi(x), \Pi(x')] = i\delta(x - x')$.
For late convenience, we rescale time and fields

$$t \to t/v, \quad \phi \to \sqrt{K\pi}\phi, \quad \Pi \to \frac{1}{\sqrt{K\pi}}\Pi, \tag{6.9}$$

which makes all parameters disappear from the post-quench Hamiltonian H and shifts them to the pre-quench Hamilonian H_0,

$$H_0 = \frac{\nu}{2}\int_x \left[\frac{1}{\kappa}\pi\Pi^2(x) + \kappa(\partial_x\phi)^2 + \tilde{K}\pi m^2\phi^2\right] \tag{6.10}$$

$$H = \frac{1}{2}\int_x \left[\Pi^2(x) + (\partial_x\phi)^2\right], \tag{6.11}$$

where we use the abbreviations $\kappa = K/\tilde{K}$ and $\nu = \tilde{v}/v$.
We introduce creation and annihilation operators $b_p^\dagger$, b_p and $a_p^\dagger$, a_p in order to diagonalise H_0 and H, respectively. In terms of b_p, $b_p^\dagger$ the field operator and the conjugate momentum become

$$\begin{aligned}\phi_p &= \frac{1}{(2\nu\sqrt{p^2 + (m^*)^2})^{1/2}}(b_p + b_{-p}^\dagger) \\ \Pi_p &= -i\left(\frac{\nu\sqrt{p^2 + (m^*)^2}t}{2}\right)^{1/2}(b_p - b_{-p}^\dagger)\end{aligned} \tag{6.12}$$

and the *pre*-quench Hamiltonian takes the diagonal form $H = \int_p \nu\sqrt{p^2 + (m^*)^2}b_p^\dagger b_b$.
$m^* = \sqrt{\tilde{K}\pi}m^2$ is the energy gap of the initial Hamiltonian
In terms of a_p and $a_p^\dagger$ we have

$$\begin{aligned}\phi_p &= \frac{1}{\sqrt{2|p|}}(a_p + a_{-p}^\dagger) \\ \Pi_p &= -i\sqrt{\frac{|p|}{2}}(a_p - a_{-p}^\dagger),\end{aligned} \tag{6.13}$$

which diagonalises the *post*-quench Hamiltonian $H = \int_p |p| a_p^\dagger a_p$.
One can also express the two sets of creation and annihilation operators in terms of each other, what will help us to calculate expectation values after the quench:

$$\begin{aligned}a_p &= \frac{1}{2\sqrt{\gamma(p)}}\left[(1 + \gamma(p))b_p + (1 - \gamma(p))b_{-p}^\dagger\right] \\ a_p^\dagger &= \frac{1}{2\sqrt{\gamma(p)}}\left[(1 + \gamma(p))b_p^\dagger + (1 - \gamma(p))b_{-p}\right],\end{aligned} \tag{6.14}$$

where we have introduced $\gamma(p) = v/|p|\sqrt{p^2 + (m^*)^2}$. The time evolution of the operators a_p, $a_p^\dagger$ in the Heisenberg picture is trivial, as $H \sim a^\dagger a$: $a_p(t) = e^{-i|p|t}a_p$, $a_p^\dagger(t) = e^{i|p|t}a_p^\dagger$.

The *initial state* of the system $|\Psi(t=0)\rangle$ is chosen to be the groundstate $|0\rangle_b$ of the pre-quench Hamiltonian H_0, which is the vacuum of b, $b_p|0\rangle_b = 0$. In terms of the a, $a^\dagger$-basis, $|\Psi(0)\rangle$ is a squeezed state.
Using Eq. (6.14), it is easy to calculate expectation values of $a_p(t)$ and $a_p^\dagger(t)$ in $|0\rangle_b$. The following correlations are helpful to calculate number fluctuations:

$$\begin{aligned}
\langle a_p(t)a_{p'}(t)\rangle &= \frac{e^{-i2|p|t}}{4\gamma(p)}(1-\gamma^2(p))\delta_{p,-p'} \\
\langle a_p(t)a_{p'}^\dagger(t)\rangle &= \frac{1}{4\gamma(p)}(1+\gamma(p))^2\delta_{p,p'} \\
\langle a_p^\dagger(t)a_{p'}(t)\rangle &= \frac{1}{4\gamma(p)}(1-\gamma(p))^2\delta_{p,p'} \\
\langle a_p^\dagger(t)a_{p'}^\dagger(t)\rangle &= \frac{e^{i2|p|t}}{4\gamma(p)}(1-\gamma^2(p))\delta_{p,-p'}
\end{aligned} \tag{6.15}$$

6.3 Full counting statistics of the particle number after the quench

6.3.1 Cumulant generating function

We now want to calculate the full counting statistics of the particle number, $\hat{N}_l(t)$ in a subsystem of linear size l, which is completely determined by the generating function $\chi(\lambda,t) = \langle\psi(t)|e^{i\lambda\hat{N}_l}|\psi(t)\rangle = \langle\psi(0)|e^{i\lambda\hat{N}_l(t)}|\psi(0)\rangle$. From the generating function $\chi(\lambda,t)$ we can get all moments of $\hat{N}_l(t)$ differentiating with respect to λ,

$$\begin{aligned}
\langle\hat{N}_l^n(t)\rangle &= (-i)^n\partial_\lambda^n\chi(\lambda,t)|_{\lambda=0} \\
C_n(l,t) &= (-i)^n\partial_\lambda^n\log\chi(\lambda,t)|_{\lambda=0}.
\end{aligned} \tag{6.16}$$

Here the $C_n(l,t)$ are the cumulants of $\hat{N}_l(t)$. The set of all moments or cumulants completely determines the statistics of the subsystem particle number and one can reconstruct its probability distribution from them. The particle number fluctuations in a subsystem, $\mathcal{F}(l,t) = \langle(\hat{N}_l(t) - \langle\hat{N}_l(t)\rangle)^2\rangle$, are identical to the second cumulant $C_2(l,t)$.
From Eq. (6.6) we get

$$\hat{N}_l(t) = \int_0^l dx\,\hat{\rho}(x) = \rho_0 l + \sqrt{\frac{K}{\pi}}(\hat{\phi}(l,t) - \hat{\phi}(0,t)). \tag{6.17}$$

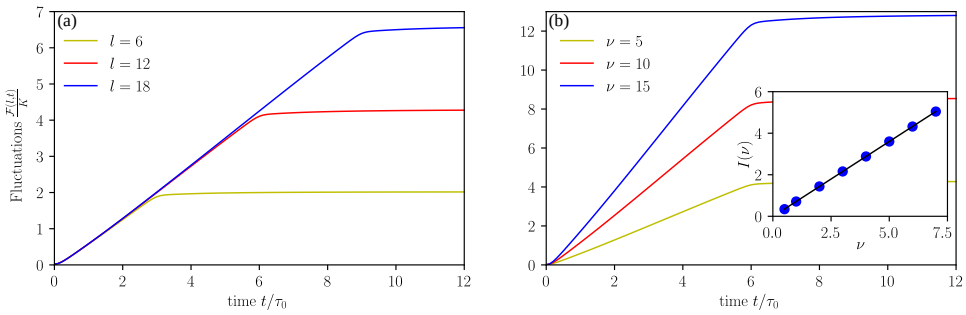

Figure 6.1: **Number fluctuations in a Luttinger liquid.** After a small time window of quadratic growth, the particle number fluctuations in a subsystem of size l grow linearly in time after a quantum quench from a gapped state. The growth saturates after time $l/2$ (in dimensionless units) and the growth rate is independent of the subsystem size l, panel (a). The slope of $\mathcal{F}(t)/K$ depends only on the ratio ν, panel (b), in the form of the function $I(\nu)$. $I(\nu)$ shows a linear dependenc on ν, panel (b) inset.

Inserting the decomposition of field operators into creation and annihilation operators $\hat{b}_p^\dagger$, $\hat{b}_p$ we find

$$\hat{N}_l(t) = \rho_0 l + \sqrt{\frac{K}{\pi}} \int_p \frac{e^{-\alpha|p|}}{2\sqrt{2|p|\gamma(p)}} (e^{ipl} - 1) \left[f_p(t) b_p + f_p^*(t) b_{-p}^\dagger \right], \quad (6.18)$$

where $f_p(t) = e^{-i|p|t}(1+\gamma(p)) + e^{i|p|t}(1-\gamma(p))$. Note that we have introduced the exponential factor $e^{-\alpha|p|}$ as smooth momentum cutoff. In order to evaluate the initial state expectation value of $e^{i\lambda\hat{N}_l(t)}$, we make use of the Zassenhaus formula $e^{X+Y} = e^X e^Y e^{-\frac{1}{2}[X,Y]} e^{\frac{1}{6}(2[Y,[X,Y]]+[X,[X,Y]])} \ldots$ and the fact, that $\hat{b}_p|\psi(0)\rangle = 0$. We obtain

$$\log \chi(\lambda, t) = i\lambda\rho_0 l - \lambda^2 \frac{K}{\pi} \int_0^\infty dp \, \frac{e^{-2\alpha p}}{p\gamma(p)} \sin^2\left(\frac{pl}{2}\right) \left[1 + (\gamma^2(p) - 1)\sin^2(pt)\right], \quad (6.19)$$

is one of main results of this section. Eq. 6.19 shows, that all cumulants of order three and higher vanish, $C_{n\geq 3}(l,t) = 0$. Hence the distribution of the particle number $\hat{N}_l(t)$ in the subsystem is gaussian, and even though the higher moments of $\hat{N}_l(t)$ are nonzero, they can all be expressed in terms of $C_1(l,t)$ and $C_2(l,t)$, i.e., the mean particle number in a subsystem, $\rho_0 l$, and the fluctuations $\mathcal{F}(l,t)$.

6.3.2 Particle number fluctuations

Expressing everything in terms of dimensionless variables and parameters, introducing $\tilde{p} = p/m^*$, $\tilde{l} = l/m^*$, $\tilde{p} = p/m^*$ and $\gamma(\tilde{p}) = \nu/\tilde{p}\sqrt{\tilde{p}^2+1}$,we finally obtain the fluctuations of the subsystem particle number

$$\mathcal{F}(\tilde{l},t) = \frac{2K}{\pi^2}\int_0^\infty d\tilde{p}\,\frac{e^{-2\tilde{\alpha}\tilde{p}}}{\tilde{p}\gamma(\tilde{p})}\sin^2\left(\frac{\tilde{p}\tilde{l}}{2}\right)\left[1+(\gamma^2(\tilde{p})-1)\sin^2(\tilde{p}m^*t)\right]. \quad (6.20)$$

The integral in Eq. (6.20) has to be evaluated numerically.
Plots of Eq. (6.20) for different values of $\tilde{l}$ and ν is shown in Fig. 6.1. One can see, that the fluctuations grow linearly in time for $m^*t < \tilde{l}/2$ and then saturate at a constant value. The subsystem size has no effect on the slope, which - in dimensionless units - depends only on the ratio $\nu = \tilde{v}/v$. In the linear growth regime, $m^*t < \tilde{l}/2$, we can write $\mathcal{F}(\tilde{l},t) = 2K/\pi^2 I(\nu)m^*t$. Plotting $I(\nu)$ as a function of ν, Fig. 6.1 (b) inset, shows that $I(\nu) = \text{const}\times\nu$, where the proportionality factor is determined from a linear fit to be 0.72169. For the fluctuations, this implies, that $\mathcal{F}(\tilde{l},t) = 2K/\pi^2 \times 0.72169\nu m^*t$ in the linear regime.
Let us now recall, that we have rescaled time with the sound velocity v, Eq. (6.9), switching back to the original time, i.e. we replace t with vt, we get that $\mathcal{F}(\tilde{l},t) = 2K/\pi^2 \times 0.72169vm^*t$, where vm^* is exactly the energy gap in the spectrum of the pre-quench Hamiltonian. Putting everything together, we can conclude, that

$$\mathcal{F}(l,t) = \text{const.} + \begin{cases} 0.72169\frac{2Kt}{\pi^2\tau_0} & t < l/2v \\ 0.72169\frac{Kl}{\pi^2 v\tau_0} & t > l/2v \end{cases}, \quad (6.21)$$

where $\tau_0 = 1/(vm^*)$ is the inverse energy gap of the initial Hamiltonian.
This results shows, that the close connection between particle number fluctuations and entanglement entropy extends from equilibrium to the dynamics after a quantum quench, as Ref.'s [216, 217] show, that

$$S_l(t) \simeq \frac{1}{3}\log\tau_0 + \begin{cases} \frac{\pi t}{6\tau_0} & t < l/2v \\ \frac{\pi l}{12v\tau_0} & t > l/2v \end{cases}. \quad (6.22)$$

The only difference between entanglement entropy and fluctuations is the growth rate, which is universal for the entanglement entropy and depends on the Luttinger parameter K for the fluctuations.

6.4 Numerical MPS results

In this section we benchmark our analytic results obtained from Luttinger liquid theory to matrix-product-state (MPS) simulations. In the numerical simulations, we calculate the time-evolution after the quench in the full Bose-Hubbard model at unit filling. The initial state is chosen as the ground state of the Bose-Hubbard Hamiltonian at onsite repulsion U_i, where $U_i \gtrsim 15$, such that the initial state is deep in the Mott-insulating phase and is approximately a product state. The post quench onsite repulsion U_f is chosen, such that the final Hamiltonian is in the superfluid phase.

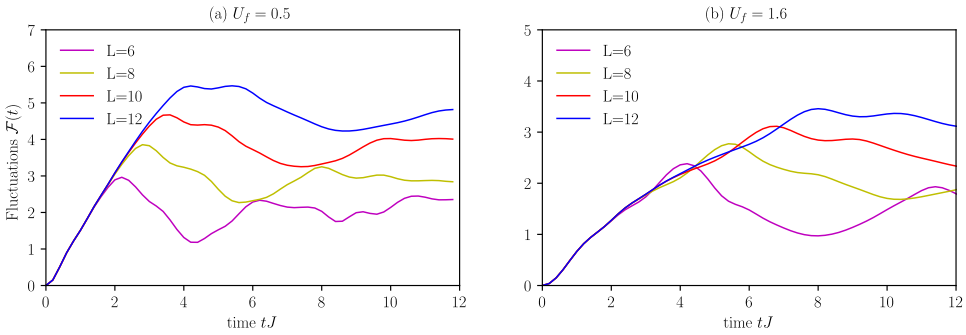

Figure 6.2: **Bipartite fluctuations after a quench from the Mott insulating to the superfluid phase in the 1D Bose-Hubbard model.** Matrix product state simulations of the 1D Bose-Hubbard model confirm the results obtain from Luttinger liquid theory. Bipartite fluctuations first grow quadratically and then linearly, yet the linear growth is cut of at a certain point due to heating effects. The linear dependence of the saturatuin timescale on subsystem size is clearly visible. Panel (a): At weak final onsite repulsion, $U_f = 0.5$, heating effects are weak and the linear growth regime extends from $tJ = 0.6$ up to $tJ = 2$. Panel (b): For stronger final onsite repulsion $U_f = 1.6$, the linear growth window $0.6 \lesssim tJ \lesssim 1.1$ becomes small. All curves are shown for $U_i = 100$.

Fig. 6.2 shows the growth of bipartite fluctuations obtained from MPS simulations for four different system sizes and two different values of the post-quench onsite repulsion, $U_f = 0.5$ panel (a) and $U_f = 1.6$ panel (b). The fluctuations show the characteristics predicted by Luttinger liquid calculation, first there is a small regime of quadratic growth, this is followed by the expected linear growth. The linear growth is however only visible in a short time-window before heating effects become relevant.

Luttinger liquid theory is strictly only applicable at low energies, where the system is close to the ground state. However, after the quench the system is in an highly excited state where nonlinear effects are visible. The size of the linear growth window depends on the value of final onsite repulsion U_f and decreases with increasing U_f. The system size has no effect on the size of the linear growth window. Fig. 6.2 shows a clear linear dependence of the onset of saturation on system size, which appears not to be affected by heating effects.

In Fig. 6.3 we show the growth of the entanglement entropy after the quench. As for the fluctuations, the curves show the characteristics expected from conformal field theory, first a quadratic growth regime, then the linear growth regime.

The linear dependence of the onset of saturation is clearly discernible also for the entanglement entropy.

CFT predicts, that the slope of the entanglement growth should be universal and independent of the interaction strength after the quench, as the parameter τ_0 is only

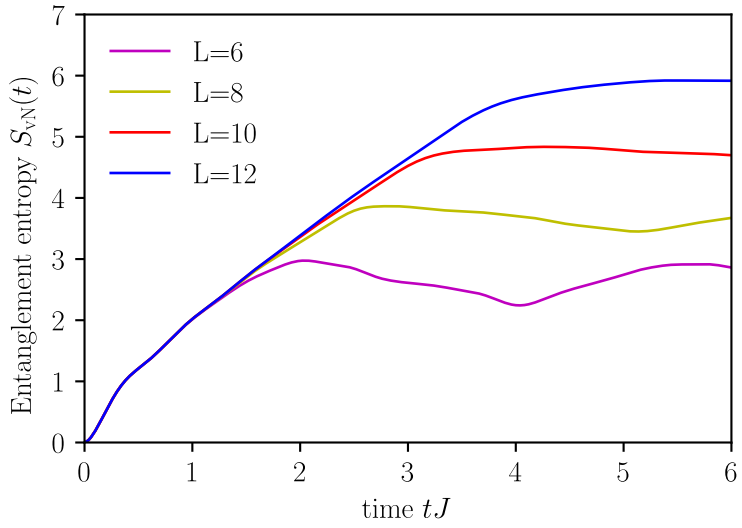

Figure 6.3: **Bipartite entanglement entropy after a quench from the Mott insulating to the superfluid phase in the 1D Bose-Hubbard model.** Matrix product state simulations of the 1D Bose-Hubbard model confirm the results obtained from conformal field theory [216, 217]. Bipartite entanglement entropy first grows quadratically and then linearly. The linear dependence of the saturation timescale on subsystem size is also clearly visible. All curves are shown for $U_i = 100$ and $U_f = 1.6$.

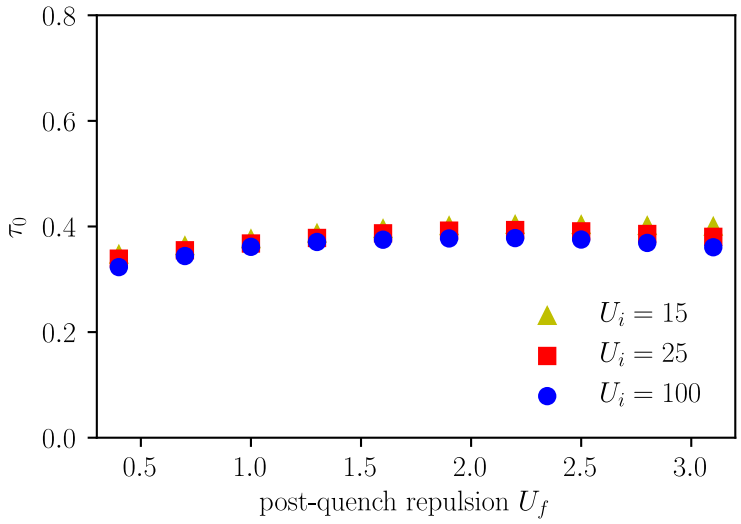

Figure 6.4: **Dependence of the timescale τ_0 on the final onsite repulsion U_f.** Conformal field theory and Luttinger liquid theory predict, that the timescale τ_0 only depends on the initial state and is independent of the final interaction parameter U_f. Extracting τ_0 from MPS-data on the entanglement entropy, one can see, that there is indeed a very weak dependence of τ_0 on U_f for $U \gtrsim 1.0$. For all curves the system size is $L = 12$.

dependent on the system before the quantum quench [216, 217]. To check this, we extract the timescale τ_0 from the entanglement entropy MPS-data and show the U_f dependence in Fig. 6.4 for different initial onsite repulsions U_i. As one can see, the dependence on U_f is weak. For $U_f \gtrsim 1.0$, τ_0 is almost independent of the final onsite repulsion, while for $U_f \lesssim 1.0$, it decreases noticeable with U_f. The reason for this decrease at small U_f is not clear, it could be a cut-off effect due to system size or high occupations of single sites, which are truncated in MPS-simulations, but become more relevant at weak onsite repulsion.
The dependence on the initial onsite repulsion U_i is also very weak over the whole range of U_f, which is consistent with the fact, that the system starts out very close to a perfect Mott-state for $U_i \gtrsim 15$.

6.5 Determining the Luttinger parameter from bipartite fluctuation measurements after a quench

Our result, that the slope of the bipartite fluctuations growth depends linearly on the Luttinger parameter K, in combination with the result from Ref's. [216, 217], that the entanglement grows with a universal slope, represents a possibility to measure K in optical lattice experiments. The procedure we propose will require access to time resolved data for the bipartite fluctuations for different values of the post-

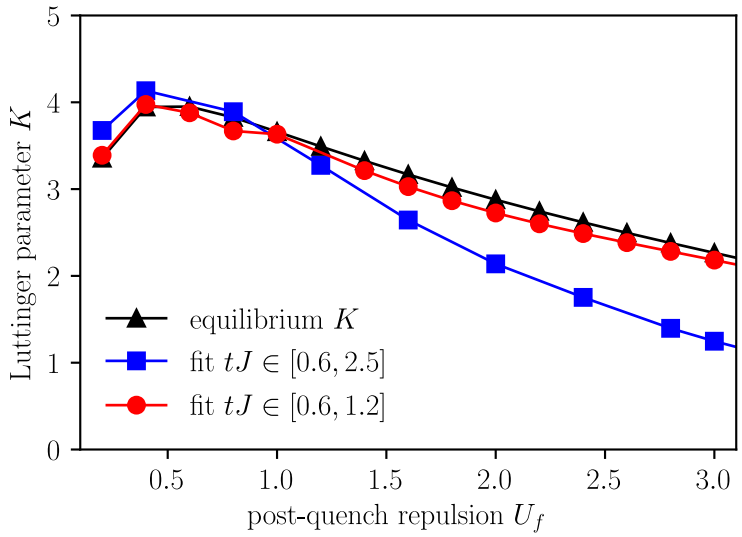

Figure 6.5: **Performance of the proposed measurement procedure for the Luttinger parameter.** Extracting the growth rate of bipartite fluctuations in the optimal fite window (red) and using we get almost perfect agreement with the finite size Luttinger parameter from equilibrium simulations (black). When using a large fit window (blue), there is still reasonable agreement for $U_f \lesssim 1.6$. For larger values of U_f deviations become sizable. All fluctuation data used is for a system size of $L = 12$. The entanglement entropy growth rate is extraced from a system size $L = 6$ and $U_f = 1.6$.

quench onsite repulsion U_f and a *single* time-trace of the second Rényi entropy H_2.

Measuring the bipartite fluctuations after a quantum quench is relatively simple in a Bose-Hubbard model, implemented as an optical lattice system, by employing single site resolution [40, 41, 42]. One lets the system evolve a certain time after the quench and counts the number of atoms in the subsystem one is interested in. This is done repeatedly in order to generate sufficient statistics for the subsystem occupation. The process is then repeated for different evolution times in order to get the time evolution of the bipartite fluctuations.

Getting access to time-resolved data for the second Rényi entropy H_2 after the quench is considerably more difficult and a highly non-trivial task. However, it has been recently achieved [198, 135].

According to Ref.'s [216, 217] the second Rényi entropy H_2 in the Luttinger liquid grows with the slope $\Delta H_2 = \pi/(8\tau_0)$ after the quench. Therefor we get in combination with Eq. (6.21)

$$K = \frac{\pi^3}{11.2}\frac{\Delta\mathcal{F}}{\Delta H_2}, \tag{6.23}$$

where $\Delta\mathcal{F}$ is the slope of the linear bipartite fluctuations growth after the quench.

Eq. (6.23) is the central equation for extracting the Luttinger parameter K from fluctuations and entropy time-traces.
As Luttinger theory and CFT predict, that τ_0 and hence ΔH_2 is independent of the post-quench onsite repulsion U_f, which is, apart from small deviations, also seen in our MPS simulations, it is actually sufficient to measure the slope of the second Rényi entropy at a single U_f^*.
In Fig. 6.5 we compare the Luttinger parameter extracted from MPS data with the procedure described above to the Luttinger parameter extracted from the finite size equilibrium density-density correlation function according to the method described in [212]. We use bipartite fluctuation data for a 12 site system and second Rényi entropy data for a 6 site system at $U_f^* = 1.6J$, which would also be feasible in current experiments. As can be seen in Fig. 6.5, the finite size Luttinger parameter extracted with our proposed method is slightly smaller, than the equilibrium K. It turns out, that this deviation is solely due to the Rényi entropy slope ΔH_2 being slightly larger than the CFT prediction, using the CFT result for ΔH_2 would make the curves overlap almost perfectly. This might very well be due to finite size or heating effects in the entanglement growth, which is very hard to decide based on our numerics.
In order to be able to discern the time window, where the bipartite fluctuations grow linearly, one needs a high resolution in time and small errorbars, which requires a lot of data. In order to check how robust our proposed procedure is against not being able to fit in the correct time window, we also fitted the bipartite fluctuations in the window $0.5 < tJ < 2.5$. The resulting values of the Luttinger parameter show a larger deviation, as can be expected, see Fig. 6.5(blue squares). However, for small final onsite repulsion $U_f \lesssim 1.4$, the agreement with the optimal curve is still reasonable.

6.6 Conclusion

We analytically calculate the full counting statistics of the particle number in a subsystem of size l in terms of the cumulant generating function $\chi(\lambda, t)$ after a quench from a gapped state to a Luttinger liquid. The obtained cumulant generating function contains only terms up to second order in the variable λ, such that all but the first and second cumulant vanish. This implies that the particle number statistics after the quench is gaussian.
From the cumulant generating function we show, that after a quench from a gapped state to a Luttinger liquid, particle number fluctuations in a subsystem grow linearly in time, with a rate, which depends linearly on the Luttinger parameter. The linear growth saturates after a time $l/(2v)$, where l is the size of the subsystem and v the Luttinger velocity. This behavior is similar to the von Neumann and Rényi entanglement entropies. Additional MPS simulations of quenches from the Mott-insulating to the superfluid phase in the one dimensional Bose-Hubbard model at half-filling show, that even though heating effects have to be expected in real

systems, the main characteristics are still visible within a transient time window. These heating effects tend to be stronger in the particle number fluctuations than in the entanglement entropy.
Based on our findings, we have further proposed a measurement procedure for the Luttinger parameter, which does not rely on the extraction of a power-law exponent from the decay of density-density correlation functions and should thus be applicable also for systems with moderate size. Our numerical analysis of this measurement procedure shows, that due to heating effects an experimental implementation would need a high time resolution and will thus be demanding, however it should then yield reasonably accurate results for the Luttinger parameter K.
In the future it would be interesting to see, whether one can develop a more detailed understanding of the heating effects present in the Bose-Hubbard model.

Chapter 7

Conclusion

In this thesis we studied the phenomenology of quantum many-body systems far from equilibrium, by using the tools of non-equilibrium quantum field theory, in particular conserving approximations. We studied four main problems: Heating and prethermalization in the periodically driven $O(N)$-model, dynamical quantum phase transition in quenches of the $O(N)$-model, many-body localization of spin-less lattice fermions and the full counting statistics of the particle number in a subsystem after quenches from a gapped state into a Luttinger liquid.
Our results for the driven $O(N)$-model show, that thermalization to infinite temperature is highly likely and that a prethermal Floquet state can be stabilized, even though interactions are strong and the driving frequency is almost resonant with the microscopic energy scales of the system. At late times we find algebraic heating, $\epsilon(t) \sim \sqrt{t}$, which is much slower than linear Joule heating.
In our study of dynamical quantum phase transitions of the $O(N)$-model we derived the rate-function of the return probability to the ground state manifold after a quench from a symmetry breaking initial state to the gapped phase. Kinks do appear in the rate function, located at the zero crossings of the order parameter and the time between kinks as a function of the distance to the dynamical quantum critical point shows critical scaling. Based on the close relation between the appearance of kinks and the order parameter dynamics we were able to draw a connection between the notions of order parameter dynamical quantum phase transitions and dynamical quantum phase transitions in the return probability. Eventhough our results were obtained with a leading order large-N expansion, we argue, that our results remain valid, when higher order corrections are taken into account.
For spin-less lattice fermions subject to a local disorder potential, we built a self-consistent Hartree-Fock approach. Remarkably much of the phenomenology of many-body localization is captured by our approach. Particularly useful is the possibility to simulate large systems to very late times, which was lacking in current exact numerical approaches. Our method shows, that close to the transition finite size effects are significant and several hundred sites are necessary to obtain asymptotic behavior. We also studied the difference between random disorder and quasi-periodic potentials; while in case of random disorder self-consistent Hartree-Fock captures rare region effects and we are able to see subdiffusive transport for weak disorder, these effects are absent for quasi-periodic disorder. Furthermore we argued that the delocalization of the system at Hartree-Fock is due to the "noisy" time-dependence of the Hartree-Fock self-energy.
For Luttinger liquids we showed, that the close relation between entanglement en-

tropy and particle number fluctuations, which was found in equilibrium also exists in non-equilibrium after quenches from a gapped state to the Luttinger liquid. This was done by calculating the full counting statistics, which furthermore showed, that the statistics of the particle number in a subsystem is gaussian. After validating our results from Luttinger liquid theory with matrix product state simulations of quenches from the Mott-insulating to the superfluid phase in the one dimensional Bose-Hubbard model, we used our results to propose a new measurement procedure for the Luttinger parameter.
Alltogether the results in this thesis reinforce, that non-equilibrium quantum field theory together with conserving approximations is a powerful tool to study non-equilibrium many-body systems, as it enables the investigation of large systems and helps building comprehensable pictures of the physics.
There are several possibilities for future extensions of the work in this thesis. Besides applying the field-theoretic methods to different models, let us focus on the ones discussed here. For the driven $O(N)$-model it would be interesting to derive a Floquet Boltzmann equation in order to study the late time heating after the prethermal plateau more in detail.
In the disordered Fermi-Hubbard model, it would be intriguing to explore the effect of periodic driving fields or how one can use the local spectral function to quantify the many-body localization transition. Periodic driving fields can be implemented into our self-consistent Hartree-Fock approach right away. For using the local spectral function to quantify the many-body localization transition on the other hand, one would need to find a good measure for the "spikeness" of the spectrum.

Acknowledgements

First of all I would like to thank Prof. Michael Knap for giving me the opportunity to do my doctoral studies with him and to work on all these interesting projects. Thank you for all the enlightening and helpful discussions and for having an active interest in my success. I learned a lot over the past years and I am very grateful for having been able to take part in the start of your Collective Quantum Dynamics group.

I am thankful for being able to collaborate with physicists outside of the Technical University of Munich and would like to thank, Markus Heyl, Alessandro Silva and Sarang Gopalakrishnan for our collaborations. The discussions with you have been very interesting and fruitful.

Furthermore I would to thank Prof. Wilhelm Zwerger for bringing me into contact with Prof. Michael Knap in the first place and also for the countless interesting and insightful discussions over lunch as well as agreeing to co-examine this thesis.

I also would like to extend my gratitude to all the members of the condensed matter theory group at the Technical University of Munich, it has been a very pleasant and productive atmosphere. Especially I would like to thank Annabelle and Fabian for letting me stay at their place during me visit to Boston and all the fun and interesting conversations and discussions. I was also very happy to share an office with Alex in the last year, thank you for our conversations about physics and our coffee/tea breaks.

I want to thank Karin Ramm and Joana Figueiredo for helping me with all the administrative matters and Stefan Recksiegel for managing the computer cluster at the department.

I would also like to acknowledge the Technical University if Munich - Institute of Advanced Study, the Deutsche Forschungsgemeinschaft (DFG) and the European Union FP7 for funding my research and as well as my travels to conferences and workshops. I also thank for the International Max Planck Research School for Quantum Science and Technology for organizing and funding my travels to summer schools and workshops.

Finally and foremost I am most grateful for the enormous support and patience of Tanja and my parents Brigitte and Franz, my sister Anna and my grandmother Hermine. I would not have managed to get here without you and thank you for all the joy you are giving me and for always being there.

Bibliography

[1] J. M. Deutsch, "Quantum statistical mechanics in a closed system," Phys. Rev. A **43**, 2046 (1991).

[2] M. Srednicki, "Chaos and quantum thermalization," Phys. Rev. E **50**, 888 (1994).

[3] M. Rigol, V. Djuno, and M. Olshanii, "Thermalization and its mechanism for generic isolated quantum systems," Nature **452**, 854 (2008).

[4] J. M. Deutsch, "Eigenstate thermalization hypothesis," Reports on Progress in Physics **81**, 082001 (2018).

[5] H. Bethe, "Zur Theorie der Metalle," Zeitschrift für Physik **71**, 205 (1931).

[6] B. Sutherland, *Beautiful Models: 70 Years of Exactly Solved Quantum Many-body Problems* (World Scientific, 2004).

[7] T. Kinoshita, T. Wenger, and D. S. Weiss, "A quantum Newton's cradle," Nature **440**, 900 (2006).

[8] D. M. Basko, I. L. Aleiner, and B. L. Altshuler, "Metal–insulator transition in a weakly interacting many-electron system with localized single-particle states," Annals of physics **321**, 1126 (2006).

[9] I. V. Gornyi, A. D. Mirlin, and D. G. Polyakov, "Interacting electrons in disordered wires: Anderson localization and low-t transport," Physical Review Letters **95**, 206603 (2005).

[10] J. Z. Imbrie, "On many-body localization for quantum spin chains," Journal of Statistical Physics **163**, 998 (2016).

[11] R. Nandkishore and D. A. Huse, "Many-body localization and thermalization in quantum statistical mechanics," Annu. Rev. Condens. Matter Phys. **6**, 15 (2015).

[12] E. Altman and R. Vosk, "Universal dynamics and renormalization in many-body-localized systems," Annu. Rev. Condens. Matter Phys. **6**, 383 (2015).

[13] V. Khemani, A. Lazarides, R. Moessner, and S. L. Sondhi, "Phase structure of driven quantum systems," Phys. Rev. Lett. **116**, 250401 (2016).

[14] D. V. Else and C. Nayak, "Classification of topological phases in periodically driven interacting systems," Phys. Rev. B **93**, 201103 (2016).

[15] C. W. von Keyserlingk and S. L. Sondhi, "Phase structure of one-dimensional interacting floquet systems. i. abelian symmetry-protected topological phases," Phys. Rev. B **93**, 245145 (2016).

[16] C. W. von Keyserlingk and S. L. Sondhi, "Phase structure of one-dimensional interacting floquet systems. ii. symmetry-broken phases," Phys. Rev. B **93**, 245146 (2016).

[17] R. Roy and F. Harper, "Abelian Floquet symmetry-protected topological phases in one dimension," Phys. Rev. B **94**, 125105 (2016).

[18] R. Roy and F. Harper, "Periodic Table for Floquet Topological Insulators," arXiv:1603.06944 (2015).

[19] A. C. Potter, T. Morimoto, and A. Vishwanath, "Classification of interacting topological floquet phases in one dimension," Physical Review X **6**, 041001 (2016).

[20] D. V. Else, B. Bauer, and C. Nayak, "Floquet Time Crystals," Phys. Rev. Lett. **117**, 090402 (2016).

[21] C. W. von Keyserlingk, V. Khemani, and S. L. Sondhi, "Absolute stability and spatiotemporal long-range order in floquet systems," Phys. Rev. B **94**, 085112 (2016).

[22] D. V. Else, B. Bauer, and C. Nayak, "Pre-thermal Time Crystals and Floquet topological phases without disorder," arXiv:1607.05277 (2016).

[23] N. Y. Yao, A. C. Potter, I.-D. Potirniche, and A. Vishwanath, "Discrete time crystals: rigidity, criticality, and realizations," arXiv:1608.02589 (2016).

[24] P. Jurcevic, H. Shen, P. Hauke, C. Maier, T. Brydges, C. Hempel, B. P. Lanyon, M. Heyl, R. Blatt, and C. F. Roos, "Direct Observation of Dynamical Quantum Phase Transitions in an Interacting Many-Body System," Phys. Rev. Lett **119**, 080501 (2017).

[25] N. Fläschner, D. Vogel, M. Tarnowski, B. S. Rem, D.-S. Luehmann, M. Heyl, J. C. Budich, L. MAthey, K. Sengstock, and C. Weiternberg, "Observation of a dynamical topological phase transition," arXiv:1608.05616 (2016).

[26] J. Zhang, G. Pagano, P. W. Hess, A. Kyprianidis, P. Becker, H. Kaplan, A. V. Gorshkov, Z.-X. Gong, and C. Monroe, "Observation of a Many-body Dynamical Phase Transition with a 53-Qubit Quantum Simulator," arXiv:1708.01044 (2017).

[27] M. Schreiber, S. S. Hodgman, P. Bordia, H. P. Lüschen, M. H. Fischer, R. Vosk, E. Altman, U. Schneider, and I. Bloch, "Observation of many-body localization of interacting fermions in a quasirandom optical lattice," Science **349**, 842 (2015).

[28] J.-y. Choi, S. Hild, J. Zeiher, P. Schauß, A. Rubio-Abadal, T. Yefash, V. Khemani, D. A. Huse, I. Bloc, and C. Gross, "Exploring the many-body localization transition in two dimensions," Science **352**, 1547 (2016).

[29] J. Smith, A. Lee, P. Richerme, B. Neyenhuis, P. W. Hess, P. Hauke, M. Heyl, D. A. Huse, and C. Monroe, "Many-body localization in a quantum simulator with programmable random disorder," Nat. Phys. **12**, 907 (2016).

[30] P. Bordia, H. P. Lüschen, S. S. Hodgman, M. Schreiber, I. Bloch, and U. Schneider, "Coupling Identical one-dimensional Many-Body Localized Systems," Phys. Rev. Lett. **116**, 140401 (2016).

[31] P. Bordia, H. P. Lüschen, U. Schneider, M. Knap, and I. Bloch, "Periodically driving a many-body localized quantum system," Nat. Phys. **13**, 460 (2017).

[32] H. P. Lüschen, P. Bordia, S. Scherg, F. Alet, E. Altman, U. Schneider, and I. Bloch, "Evidence for Griffiths-Type Dynamics near the Many-Body Localization Transition in Quasi-Periodic Systems," arXiv:1612.07173 (2016).

[33] P. Bordia, H. Lüschen, S. Scherg, S. Gopalakrishnan, M. Knap, U. Scheider, and I. Bloch, "Probing Slow Relaxation and Many-Body Localization in Two-Dimensional Quasi-Periodic Systems," arXiv:1704.03063 (2017).

[34] J. Zhang, P. W. Hess, A. Kyprianidis, P. Becker, A. Lee, J. Smith, G. Pagano, I. D. Potirniche, A. C. Potter, A. Vishwanath, N. Y. Yao, and C. Monroe, "Observation of a discrete time crystal," Nature **543**, 217 (2017).

[35] S. Choi, J. Choi, R. Landig, G. Kucsko, H. Zhou, J. Isoya, F. Jelezko, S. Onoda, H. Sumiya, V. Khemani, C. v. Keyserlingk, N. Y. Yao, E. Demler, and M. D. Lukin, "Observation of dicrete time-crystalline order in a disordered dipolar many-body system," Nature **543**, 221 (2017).

[36] E. A. Martinez, C. A. Muschik, P. Schindler, D. Nigg, A. Erhard, M. Heyl, P. Hauke, M. Dalmonte, T. Monz, P. Zoller, and R. Blatt, "Real-time dynamics of lattice gauge theories with a few-qubit quantum computer," Nature **534**, 516 (2015).

[37] W. S. Bakr, J. I. Gillen, A. Peng, S. Fölling, and M. Greiner, "A quantum gas microscope for detecting single atoms in a hubbard-regime optical lattice," Nature **462**, 74 (2009).

[38] J. F. Sherson, C. Weitenberg, M. Endres, M. Cheneau, I. Bloch, and S. Kuhr, "Single-atom-resolved fluorescence imaging of an atomic Mott insulator," Nature **467**, 68 (2010).

[39] M. Miranda, R. Inoue, Y. Okuyama, A. Nakamoto, and M. Kozuma, "Site-resolved imaging of ytterbium atoms in a two-dimensional optical lattice," Phys. Rev. A **91**, 063414 (2015).

[40] E. Haller, J. Hudson, A. Kelly, D. A. Cotta, B. Peaudecerf, G. D. Bruce, and S. Kuhr, "Single-atom imaging of fermions in a quantum-gas microscope," Nature Physics **11**, 738 (2015).

[41] L. W. Cheuk, M. A. Nichols, M. Okan, T. Gersdorf, V. V. Ramasesh, W. S. Bakr, T. Lompe, and M. W. Zwierlein, "Quantum-Gas Microscope for Fermionic Atoms," Phys. Rev. Lett. **114**, 193001 (2015).

[42] M. F. Parsons, F. Huber, A. Mazurenko, C. S. Chiu, W. Setiawan, K. Wooley-Brown, S. Blatt, and M. Greiner, "Site-Resolved Imaging of Fermionic ^{6}Li in an Optical Lattice," Phys. Rev. Lett. **114**, 213002 (2015).

[43] F. Krausz and M. Ivanov, "Attosecond physics," Rev. Mod. Phys. **81**, 163 (2009).

[44] R. Pazourek, S. Nagele, and J. Burgdörfer, "Attosecond chronoscopy of photoemission," Rev. Mod. Phys. **87**, 765 (2015).

[45] J. Schwinger, "Brownian motion of a quantum oscillator," Journal of Mathematical Physics **2**, 407 (1961).

[46] A. Kamenev, *Field theory of non-equilibrium systems* (Cambridge University Press, 2011).

[47] J. M. Cornwall, R. Jackiw, and E. Tomboulis, "Effective action for composite operators," Phys. Rev. D **10**, 2428 (1974).

[48] J. Berges, "Controlled nonperturbative dynamics of quantum fields out of equilibrium," Nucl. Phys. A **699**, 847 (2002).

[49] G. Aarts, D. Ahrensmeier, R. Baier, J. Berges, and J. Serreau, "Far-from-equilibrium dynamics with broken symmetries from the 1/N expansion of the 2PI effective action," Phys. Rev. D **66**, 045008 (2002).

[50] M. Moshe and J. Zinn-Justin, "Quantum field theory in the large N limit: a review," Phys. Rep. **385**, 385 (2003).

[51] F. D. M. Haldane, "Effective harmonic-fluid approach to low-energy properties of one-dimensional quantum fluids," Phys. Rev. Lett. **47**, 1840 (1981).

[52] T. Giamarchi, *Quantum Physics in One Dimension* (Clarendon Press, 2003).

[53] J. M. Luttinger and J. C. Ward, "Ground-state energy of a many-fermion system. ii," Phys. Rev. **118**, 1417 (1960).

[54] G. Baym, "Self-consistent approximations in many-body systems," Phys. Rev. **127**, 1391 (1962).

[55] D. C. Langreth in, *Linear and Nonlinear Electron Transport in Solids* (Springer US, 1976).

[56] T. Oka and H. Aoki, "Photovoltaic Hall effect in graphene," Phys. Rev. B **79**, 081406 (2009).

[57] T. Kitagawa, T. Oka, A. Brataas, L. Fu, and E. Demler, "Transport properties of nonequilibrium systems under the application of light: Photoinduced quantum Hall insulators without Landau levels," Phys. Rev. B **84**, 235108 (2011).

[58] N. H. Lindner, G. Refael, and V. Galitski, "Floquet topological insulator in semiconductor quantum wells," Nat. Phys. **7**, 490 (2011).

[59] M. Aidelsburger, M. Atala, M. Lohse, J. T. Barreiro, B. Paredes, and I. Bloch, "Realization of the hofstadter hamiltonian with ultracold atoms in optical lattices," Phys. Rev. Lett. **111**, 185301 (2013).

[60] H. Miyake, G. A. Siviloglou, C. J. Kennedy, W. C. Burton, and W. Ketterle, "Realizing the harper hamiltonian with laser-assisted tunneling in optical lattices," Phys. Rev. Lett. **111**, 185302 (2013).

[61] G. Jotzu, M. Messer, R. Desbuquois, M. Lebrat, T. Uehlinger, D. Greif, and T. Esslinger, "Experimental realisation of the topological Haldane model with ultracold fermions," Nature **515**, 237 (2014).

[62] M. Aidelsburger, M. Lohse, C. Schweizer, M. Atala, J. T. Barreiro, S. Nascimbène, N. R. Cooper, I. Bloch, and N. Goldman, "Measuring the chern number of hofstadter bands with ultracold bosonic atoms," Nat. Phys. **11**, 162 (2015).

[63] P. Ponte, A. Chandran, Z. Papić, and D. A. Abanin, "Periodically driven ergodic and many-body localized quantum systems," Annals of Physics **353**, 196 (2015).

[64] A. Lazarides, A. Das, and R. Moessner, "Fate of many-body localization under periodic driving," Phys. Rev. Lett. **115**, 030402 (2015).

[65] D. A. Abanin, W. D. Roeck, and Francois, "Theory of many-body localization in periodically driven systems," Ann. Phys. **372**, 1 (2016).

[66] M. Kozarzewski, P. Prelovšek, and M. Mierzejewski, "Distinctive response of many-body localized systems to a strong electric field," Phys. Rev. B **93**, 235151 (2016).

[67] J. Rehn, A. Lazarides, F. Pollmann, and R. Moessner, "How periodic driving heats a disordered quantum spin chain," Phys. Rev. B **94**, 020201(R) (2016).

[68] S. Gopalakrishnan, M. Knap, and E. Demler, "Regimes of heating and dynamical response in driven many-body localized systems," Phys. Rev. B **94**, 094201 (2016).

[69] P. Bordia, H. Lüschen, U. Schneider, M. Knap, and I. Bloch, "Periodically driving a many-body localized quantum system," arXiv:1607.07868 (2016).

[70] L. D'Alessio and M. Rigol, "Long-time behavior of isolated periodically driven interacting lattice systems," Phys. Rev. X **4**, 041048 (2014).

[71] A. Lazarides, A. Das, and R. Moessner, "Equilibrium states of generic quantum systems subject to periodic driving," Phys. Rev. E **90**, 012110 (2014).

[72] D. Abanin, W. De Roeck, F. Huveneers, and W. W. Ho, "A rigorous theory of many-body prethermalization for periodically driven and closed quantum systems," arXiv:1509.05386 (2015).

[73] D. A. Abanin, W. De Roeck, and W. W. Ho, "Effective Hamiltonians, prethermalization and slow energy absorption in periodically driven many-body systems," arXiv:1510.03405 (2015).

[74] D. A. Abanin, W. De Roeck, and F. Huveneers, "Exponentially Slow Heating in Periodically Driven Many-Body Systems," Phys. Rev. Lett. **115**, 256803 (2015).

[75] T. Mori, T. Kuwahara, and K. Saito, "Rigorous Bound on Energy Absorption and Generic Relaxation in Periodically Driven Quantum Systems," Phys. Rev. Lett. **116**, 120401 (2016).

[76] M. Bukov, S. Gopalakrishnan, M. Knap, and E. Demler, "Prethermal Floquet Steady States and Instabilities in the Periodically Driven, Weakly Interacting Bose-Hubbard Model," Phys. Rev. Lett. **115**, 205301 (2015).

[77] E. Canovi, M. Kollar, and M. Eckstein, "Stroboscopic prethermalization in weakly interacting periodically driven systems," Phys. Rev. E **93**, 012130 (2016).

[78] A. Chandran and S. L. Sondhi, "Interaction-stabilized steady states in the driven $O(N)$ model," Phys. Rev. B **93**, 174305 (2016).

[79] N. H. Lindner, E. Berg, and M. S. Rudner, "Universal chiral quasi-steady states in periodically driven many-body systems," arXiv:1603.03053 (2016).

[80] F. Cooper, S. Habib, Y. Kluger, and E. Mottola, "Nonequilibrium dynamics of symmetry breaking in $\lambda\Phi^4$ theory," Phys. Rev. D **55**, 6471 (1997).

[81] D. Boyanovsky, de Vega HJ, R. Holman, and J. Salgado, "Analytic and numerical study of preheating dynamics." Phys. Rev. D **54**, 7570 (1996).

[82] J. Berges and J. Serreau, "Parametric resonance in quantum field theory," Phys. Rev. Lett. **91**, 111601 (2002).

[83] J. Berges and T. Gasenzer, "Quantum versus classical statistical dynamics of an ultracold Bose gas," Phys. Rev. A **76**, 033604 (2007).

[84] S. Sotiriadis and J. Cardy, "Quantum quench in interacting field theory: A self-consistent approximation," Phys. Rev. B **81**, 134305 (2010).

[85] B. Sciolla and G. Biroli, "Quantum quenches, dynamical transitions, and off-equilibrium quantum criticality," Phys. Rev. B **88**, 201110 (2013).

[86] A. Chandran, A. Nanduri, S. S. Gubser, and S. L. Sondhi, "Equilibration and coarsening in the quantum $O(N)$ model at infinite N," Phys. Rev. B **88**, 024306 (2013).

[87] P. Smacchia, M. Knap, E. Demler, and A. Silva, "Exploring dynamical phase transitions and prethermalization with quantum noise of excitations," Phys. Rev. B **91**, 205136 (2015).

[88] A. Chiocchetta, M. Tavora, A. Gambassi, and A. Mitra, "Short-time universal scaling in an isolated quantum system after a quench," Phys. Rev. B **91**, 220302(R) (2015).

[89] A. Maraga, A. Chiocchetta, A. Mitra, and A. Gambassi, "Aging and coarsening in isolated quantum systems after a quench: Exact results for the quantum $O(N)$ model with $N \to \infty$," Phys. Rev. E **92**, 042151 (2015).

[90] L. V. Keldysh, "Diagram Technique for Nonequilibrium Processes," Sov. Phys. JETP **20**, 1018 (1965).

[91] M. Knap, M. Babadi, G. Refael, I. Martin, and E. Demler, "Dynamical Cooper pairing in non-equilibrium electron-phonon systems," arXiv:1511.07874 (2015).

[92] K. Mallick and P. Marcq, "Anomalous diffusion in nonlinear oscillators with multiplicative noise," Phys. Rev. E **66**, 041113 (2002).

[93] K. Mallick and P. Marcq, "Effects of parametric noise on a nonlinear oscillator," Physica A **325**, 213 (2002).

[94] M. Gring, M. Kuhnert, T. Langen, T. Kitagawa, B. Rauer, M. Schreitl, I. Mazets, D. A. Smith, E. Demler, and J. Schmiedmayer, "Relaxation and prethermalization in an isolated quantum system," Science **337**, 1318 (2012).

[95] T. Langen, S. Erne, R. Geiger, B. Rauer, T. Schweigler, M. Kuhnert, W. Rohringer, I. E. Mazets, T. Gasenzer, and J. Schmiedmayer, "Experimental observation of a generalized Gibbs ensemble," Science **348**, 207 (2015).

[96] F. Meinert, M. Knap, E. Kirilov, K. Jag-Lauber, M. B. Zvonarev, E. Demler, and H.-C. Nägerl, "Bloch oscillations in the absence of a lattice," Science **356**, 945 (2017).

[97] B. Sciolla and G. Biroli, "Quantum quenches, dynamical transitions, and off-equilibrium quantum criticality," Phys. Rev. B **88**, 201110(R) (2013).

[98] H. W. Diehl, "The theory of boundary critical phenomena," International Journal of Modern Physics B **11**, 3503 (1997).

[99] B. Zunkovic, M. Heyl, M. Knap, and A. Silva, "Dynamical Quantum Phase Transitions in Spin Chains with Long-Range Interactions: Merging different concepts of non-equilibrium criticality," arXiv:1609.08482 (2016).

[100] E. A. Yuzbashyan, O. Tsyplyatyev, and B. L. Altshuler, "Relaxation and Persistent Oscillations of the Order Parameter in Fermionic Condensates," Phys. Rev. Lett. **96**, 097005 (2006).

[101] M. Eckstein, M. Kollar, and P. Werner, "Interaction quench in the hubbard model: Relaxation of spectral function and the optical conductivity," Phys. Rev. B **81**, 115131 (2010).

[102] A. Gambassi and P. Calabrese, "Quantum quenches as classical critical films," Europhys. Lett **95**, 6 (2010).

[103] M. Schiro and M. Fabrizio, "Time-Dependent Mean Field Theory for Quench Dynamics in Correlated Electron Systems," Phys. Rev. Lett. **105**, 076401 (2010).

[104] B. Sciolla and G. Biroli, "Dynamical transitions and quantum quenches in mean-field models," J. Stat. Mech.: Theor. and Exper. **11**, P11003 (2011).

[105] S. A. Hamerla and G. S. Uhrig, "Dynamical transition in interaction quenches of the one-dimensional Hubbard model," Phys. Rev. B **87**, 064304 (2013).

[106] P. Smacchia, M. Knap, E. Demler, and A. Silva, "Exploring dynamical phase transitions and prethermalization with quantum noise of excitations," Phys. Rev. B **91**, 205136 (2015).

[107] J. C. Halimeh and V. Zauner-Stauber, "Dynamical phase diagram of quantum spin chains with long-range interactions," arXiv:1610.02019 (2016).

[108] I. Homrighausen, N. O. Abeling, V. Zauner-Stauber, and J. C. Halimeh, "Anomalous dynamical phase in quantum spin chains with long-range interactions," Phys. Rev. B **96**, 104436 (2017).

[109] M. Heyl, A. Polkovnikov, and S. Kehrein, "Dynamical Quantum Phase Transitions in the Transverse-Field Ising Model," Phys. Rev. Lett. **113**, 135704 (2013).

[110] M. Heyl, "Dynamical Quantum Phase Transitions in Systems with Broken-Symmetry Phases," Phys. Rev. Lett. **113**, 205701 (2014).

[111] C. Karrasch and D. Schuricht, "Dynamical phase tran- sitions after quenches in non-integrable models," Phys. Rev. B **87**, 195104 (2013).

[112] F. Andraschko and J. Sirker, "Dynamical quantum phase transitions and the Loschmidt echo: A transfer matrix approach," Phys. Rev. B **89**, 125120 (2014).

[113] J. Kriel, C. Karrasch, and S. Kehrein, "Dynamical quantum phase transitions in the axial next-nearest-neighbor Ising chain," Phys. Rev. B **90**, 125106 (2014).

[114] E. Canovi, P. Werner, and M. Eckstein, "First-order dynamical phase transitions," Phys. Rev. Lett **113**, 265702 (2014).

[115] S. Vajna and B. Dóra, "Disentangling dynamical phase transitions from equilibrium phase transitions," Phys. Rev. B **89**, 161105 (2014).

[116] B. Dóra, F. Pollmann, J. Fortágh, and G. Zaránd, "Loschmidt Echo and the Many-body Orthogonality Catastrophe in a Qubit-Coupled Luttinger Liquid," Phys. Rev. Lett. **111**, 046402 (2013).

[117] M. Heyl, "Scaling and Universality at Dynamical Quantum Phase Transitions," Phys. Rev. Lett. **115**, 140602 (2015).

[118] S. Sharma, S. Suzuki, and A. Dutta, "Quenches and dynamical phase transitions in a nonintegrable quantum Ising model," Phys. Rev. B **92**, 104306 (2015).

[119] M. Heyl, "Quenching a quantum critical state by the order parameter: Dynamical quantum phase transitions and quantum speed limits," Phys. Rev. B **95**, 060504(R) (2017).

[120] T. Fogarty, A. Usui, T. Busch, A. Silva, and J. Goold, "Dynamical phase transitions, temporal orthogonality and the dynamics of observables in one dimensional ultra-cold quantum gases: from the continuum to the lattice," arXiv:1704.07659 (2017).

[121] M. Cetina, M. Jag, R. S. Lous, I. Fritsche, J. T. M. Walraven, R. Grimm, J. Levinsen, M. M. Parish, R. Schmidt, M. Knap, and E. Demler, "Ultrafast many-body interferometry of impurities coupled to a fermi sea," Science **354**, 96 (2016).

[122] P. Talkner, E. Lutz, and P. Hänggi, "Fluctuation theorems: Work is not an observable," Phys. Rev. E **75**, 050102(R) (2007).

[123] A. Silva, "Statistics of Work Done on a Quantum Critical System by Quenching a Control Parameter," Phys. Rev. Lett. **101**, 120603 (2008).

[124] M. Campisi, P. Hänggi, and P. Talkner, "Colloquium: Quantum fluctuation relations: Foundations and applications," Rev. Mod. Phys. **83**, 1653 (2011).

[125] Schreiber, Michael and Hodgman, Sean S. and Bordia, Pranjal and Lüschen, Henrik P. and Fischer, Mark H. and Vosk, Ronen and Altman, Ehud and Schneider, Ulrich and Bloch, Immanuel, "Observation of many-body localization of interacting fermions in a quasi-random optical lattice," Science , 7432 (2015).

[126] S. S. Kondov, W. R. McGehee, W. Xu, and B. DeMarco, "Disorder-induced localization in a strongly correlated atomic hubbard gas," Physical Review Letters **114**, 083002 (2015).

[127] J. Smith, A. Lee, P. Richerme, B. Neyenhuis, P. W. Hess, P. Hauke, M. Heyl, D. A. Huse, and C. Monroe, "Many-body localization in a quantum simulator with programmable random disorder," Nature Physics **12**, 907 (2016).

[128] P. Bordia, H. P. Lüschen, S. S. Hodgman, M. Schreiber, I. Bloch, and U. Schneider, "Coupling identical one-dimensional many-body localized systems," Physical Review Letters **116**, 140401 (2016).

[129] J.-y. Choi, S. Hild, J. Zeiher, P. Schauß, A. Rubio-Abadal, T. Yefsah, V. Khemani, D. A. Huse, I. Bloch, and C. Gross, "Exploring the many-body localization transition in two dimensions," Science **352**, 1547 (2016).

[130] P. Bordia, H. Lüschen, U. Schneider, M. Knap, and I. Bloch, "Periodically driving a many-body localized quantum system," Nature Physics **13**, 460 (2017).

[131] P. Bordia, H. Lüschen, S. Scherg, S. Gopalakrishnan, M. Knap, U. Schneider, and I. Bloch, "Probing slow relaxation and many-body localization in two-dimensional quasiperiodic systems," Phys. Rev. X **7**, 041047 (2017).

[132] H. P. Lüschen, P. Bordia, S. Scherg, F. Alet, E. Altman, U. Schneider, and I. Bloch, "Observation of slow dynamics near the many-body localization transition in one-dimensional quasiperiodic systems," Physical Review Letters **119**, 260401 (2017).

[133] P. Roushan, C. Neill, J. Tangpanitanon, V. M. Bastidas, A. Megrant, R. Barends, Y. Chen, Z. Chen, B. Chiaro, A. Dunsworth, A. Fowler, B. Foxen, M. Giustina, E. Jeffrey, J. Kelly, E. Lucero, J. Mutus, M. Neeley, C. Quintana, D. Sank, A. Vainsencher, J. Wenner, T. White, H. Neven, D. G.

Angelakis, and J. Martinis, "Spectroscopic signatures of localization with interacting photons in superconducting qubits," Science **358**, 1175 (2017).

[134] D. M. Silevitch, G. Aeppli, and T. F. Rosenbaum, "Probing many-body localization in a disordered quantum magnet," arXiv:1707.04952 (2017).

[135] A. Lukin, M. Rispoli, R. Schittko, M. E. Tai, A. M. Kaufman, S. Choi, V. Khemani, J. L'eonard, and M. Greiner, "Probing entanglement in a many-body-localized system," arXiv:1805.09819 (2018).

[136] J. M. Deutsch, "Quantum statistical mechanics in a closed system," Physical Review A **43**, 2046 (1991).

[137] M. Srednicki, "Chaos and quantum thermalization," Physical Review E **50**, 888 (1994).

[138] M. Rigol, V. Dunjko, and M. Olshanii, "Thermalization and its mechanism for generic isolated quantum systems," Nature **452**, 854 (2008).

[139] G. De Chiara, S. Montangero, P. Calabrese, and R. Fazio, "Entanglement entropy dynamics of heisenberg chains," Journal of Statistical Mechanics: Theory and Experiment **2006**, P03001 (2006).

[140] M. Žnidarič, T. Prosen, and P. Prelovšek, "Many-body localization in the Heisenberg XXZ magnet in a random field," Phys. Rev. B **77**, 064426 (2008).

[141] J. H. Bardarson, F. Pollmann, and J. E. Moore, "Unbounded growth of entanglement in models of many-body localization," Physical Review Letters **109**, 017202 (2012).

[142] M. Serbyn, M. Knap, S. Gopalakrishnan, Z. Papić, N. Y. Yao, C. R. Laumann, D. A. Abanin, M. D. Lukin, and E. A. Demler, "Interferometric probes of many-body localization," Physical Review Letters **113**, 147204 (2014).

[143] Y. Bahri, R. Vosk, E. Altman, and A. Vishwanath, "Localization and topology protected quantum coherence at the edge of hot matter," Nature communications **6**, 7341 (2015).

[144] M. Serbyn, Z. Papić, and D. A. Abanin, "Quantum quenches in the many-body localized phase," Phys. Rev. B **90**, 174302 (2014).

[145] E. J. Torres-Herrera, A. M. Garcia-Garcia, and L. F. Santos, "Generic dynamical features of quenched interacting quantum systems: Survival probability, density imbalance, and out-of-time-ordered correlator," Phys. Rev. B **97**, 060303 (2018).

[146] M. Schiulaz, E. J. Torres-Herrera, and L. F. Santos, "Thouless and relaxation time scales in many-body quantum systems," arXiv:1807.07577 [cond-mat] (2018).

[147] A. Pal and D. A. Huse, "Many-body localization phase transition," Phys. Rev. B **82**, 174411 (2010).

[148] D. J. Luitz, N. Laflorencie, and F. Alet, "Many-body localization edge in the random-field heisenberg chain," Physical Review B **91**, 081103 (2015).

[149] K. Agarwal, S. Gopalakrishnan, M. Knap, M. Müller, and E. Demler, "Anomalous diffusion and griffiths effects near the many-body localization transition," Physical Review Letters **114**, 160401 (2015).

[150] R. Vosk, D. A. Huse, and E. Altman, "Theory of the many-body localization transition in one-dimensional systems," Phys. Rev. X **5**, 031032 (2015).

[151] A. C. Potter and R. Vasseur, "Symmetry constraints on many-body localization," Phys. Rev. B **94**, 224206 (2016).

[152] S. Gopalakrishnan and R. Nandkishore, "Mean-field theory of nearly many-body localized metals," Phys. Rev. B **90**, 224203 (2014).

[153] P. T. Dumitrescu, R. Vasseur, and A. C. Potter, "Scaling theory of entanglement at the many-body localization transition," Phys. Rev. Lett. **119**, 110604 (2017).

[154] T. Thiery, F. Huveneers, M. Müller, and W. De Roeck, "Many-body delocalization as a quantum avalanche," arXiv:1706.09338 (2017).

[155] V. Khemani, S. Lim, D. Sheng, and D. A. Huse, "Critical properties of the many-body localization transition," Phys. Rev. X **7** (2017).

[156] I. V. Gornyi, A. D. Mirlin, D. G. Polyakov, and A. L. Burin, "Spectral diffusion and scaling of many-body delocalization transitions," Annalen der Physik **529**, 1600360 (2017).

[157] A. Goremykina, R. Vasseur, and M. Serbyn, "Analytically solvable renormalization group for the many-body localization transition," arXiv:1807.04285 (2018).

[158] J.-H. Han and K.-S. Kim, "Boltzmann transport theory for many-body localization," Phys. Rev. B **97**, 214206 (2018).

[159] P. M. Chaikin and T. C. Lubensky, *Principles of Condensed Matter Physics* (Cambridge University Press, 1995).

[160] R. Vosk and E. Altman, "Many-body localization in one dimension as a dynamical renormalization group fixed point," Physical Review Letters **110**, 067204 (2013).

[161] D. A. Huse, R. Nandkishore, and V. Oganesyan, "Phenomenology of fully many-body-localized systems," Physical Review B **90**, 174202 (2014).

[162] M. Serbyn, Z. Papić, and D. A. Abanin, "Local conservation laws and the structure of the many-body localized states," Physical Review Letters **111**, 127201 (2013).

[163] V. Ros, M. Müller, and A. Scardicchio, "Integrals of motion in the many-body localized phase," Nuclear Physics B **891**, 420 (2015).

[164] G. Baym and L. P. Kadanoff, "Conservation laws and correlation functions," Physical Review **124**, 287 (1961).

[165] L. V. Keldysh *et al.*, "Diagram technique for nonequilibrium processes," Sov. Phys. JETP **20**, 1018 (1965).

[166] Y. Bar Lev, G. Cohen, and D. R. Reichman, "Absence of diffusion in an interacting system of spinless fermions on a one-dimensional disordered lattice," Phys. Rev. Lett. **114**, 100601 (2015).

[167] S. Gopalakrishnan, K. Agarwal, E. A. Demler, D. A. Huse, and M. Knap, "Griffiths effects and slow dynamics in nearly many-body localized systems," Physical Review B **93**, 134206 (2016).

[168] S. Gopalakrishnan, M. Müller, V. Khemani, M. Knap, E. Demler, and D. A. Huse, "Low-frequency conductivity in many-body localized systems," Phys. Rev. B **92**, 104202 (2015).

[169] M. Mierzejewski, J. Herbrych, and P. Prelovšek, "Universal dynamics of density correlations at the transition to the many-body localized state," Phys. Rev. B **94**, 224207 (2016).

[170] P. Prelovšek, M. Mierzejewski, O. Barišić, and J. Herbrych, "Density correlations and transport in models of many-body localization," Annalen der Physik **529**, 1600362 (2017).

[171] K. Agarwal, E. Altman, E. Demler, S. Gopalakrishnan, D. A. Huse, and M. Knap, "Rare-region effects and dynamics near the many-body localization transition," Annalen der Physik (2017).

[172] Žnidarič, Marko and Scardicchio, Antonello and Varma, Vipin Kerala, "Diffusive and Subdiffusive Spin Transport in the Ergodic Phase of a Many-Body Localizable System," Phys. Rev. Lett. **117**, 040601 (2016).

[173] Y. B. Lev, D. M. Kennes, C. Klöckner, D. R. Reichman, and C. Karrasch, "Transport in quasiperiodic interacting systems: From superdiffusion to subdiffusion," EPL (Europhysics Letters) **119**, 37003 (2017).

[174] M. Žnidarič and M. Ljubotina, "Interaction instability of localization in quasiperiodic systems," Proceedings of the National Academy of Sciences **115**, 4595 (2018).

[175] S. F. Edwards and P. W. Anderson, "Theory of spin glasses," Journal of Physics F: Metal Physics **5**, 965 (1975).

[176] Y. Bar Lev and D. R. Reichman, "Dynamics of many-body localization," Phys. Rev. B **89**, 220201 (2014).

[177] Y. B. Lev and D. R. Reichman, "Slow dynamics in a two-dimensional anderson-hubbard model," EPL (Europhysics Letters) **113**, 46001 (2016).

[178] S. Aubry and G. André, "Analyticity breaking and anderson localization in incommensurate lattices," Ann. Israel Phys. Soc **3**, 18 (1980).

[179] T. Devakul and R. R. P. Singh, "Early breakdown of area-law entanglement at the many-body delocalization transition," Phys. Rev. Lett. **115**, 187201 (2015).

[180] E. V. H. Doggen, F. Schindler, K. S. Tikhonov, A. D. Mirlin, T. Neupert, D. G. Polyakov, and I. V. Gornyi, "Many-body (de)localization in large quantum chains," arXiv:1807.05051 (2018).

[181] S. Gopalakrishnan, K. R. Islam, and M. Knap, "Noise-induced subdiffusion in strongly localized quantum systems," Physical Review Letters **119**, 046601 (2017).

[182] R. Nandkishore, S. Gopalakrishnan, and D. A. Huse, "Spectral features of a many-body-localized system weakly coupled to a bath," Physical Review B **90**, 064203 (2014).

[183] Aarts, Gert and Berges, Jürgen, "Nonequilibrium time evolution of the spectral function in quantum field theory," Phys. Rev. D **64**, 105010 (2001).

[184] Jürgen Berges and Jürgen Cox, "Thermalization of quantum fields from time-reversal invariant evolution equations," Physics Letters B **517**, 369 (2001).

[185] Jürgen Berges, "Controlled nonperturbative dynamics of quantum fields out of equilibrium," Nuclear Physics A **699**, 847 (2002).

[186] S. A. Weidinger and M. Knap, "Floquet prethermalization and regimes of heating in a periodically driven, interacting quantum system," Sci. Rep. **7**, 45382 (2017).

[187] Jonathan Wurtz and Anatoli Polkovnikov and Dries Sels, "Cluster truncated Wigner approximation in strongly interacting systems," Annals of Physics **395**, 341 (2018).

[188] S. A. Moses, J. P. Covey, M. T. Miecnikowski, D. S. Jin, and J. Ye, "New frontiers for quantum gases of polar molecules," Nature Physics **13**, 13 (2017).

[189] A. Bohrdt, D. Greif, E. Demler, M. Knap, and F. Grusdt, "Angle-resolved photoemission spectroscopy with quantum gas microscopes," Phys. Rev. B **97**, 125117 (2018).

[190] Christoph Holzhey and Finn Larsen and Frank Wilczek, "Geometric and renormalized entropy in conformal field theory," Nuclear Physics B **424**, 443 (1994).

[191] M. Srednicki, "Entropy and area," Phys. Rev. Lett. **71**, 666 (1993).

[192] Pasquale Calabrese and John Cardy, "Entanglement entropy and quantum field theory," Journal of Statistical Mechanics: Theory and Experiment **2004**, P06002 (2004).

[193] L. Bombelli, R. K. Koul, J. Lee, and R. D. Sorkin, "Quantum source of entropy for black holes," Phys. Rev. D **34**, 373 (1986).

[194] L. Amico, R. Fazio, A. Osterloh, and V. Vedral, "Entanglement in many-body systems," Rev. Mod. Phys. **80**, 517 (2008).

[195] A. Kitaev and J. Preskill, "Topological entanglement entropy," Phys. Rev. Lett. **96**, 110404 (2006).

[196] M. Levin and X.-G. Wen, "Detecting topological order in a ground state wave function," Phys. Rev. Lett. **96**, 110405 (2006).

[197] R. Islam, R. Ma, P. M. Preiss, M. Eric Tai, A. Lukin, M. Rispoli, and M. Greiner, "Measuring entanglment entropy in a quantum many-body system," Nature **528**, 77 (2015).

[198] A. M. Kaufman, M. E. Tai, A. Lukin, M. Rispoli, R. Schittko, P. M. Preiss, and M. Greiner, "Quantum thermalization through entanglement in an isolated many-body system," Science **353**, 794 (2016).

[199] H. F. Song, C. Flindt, S. Rachel, I. Klich, and K. Le Hur, "Entanglement entropy from charge statistics: Exact relations for noninteracting many-body systems," Phys. Rev. B **83**, 161408 (2011).

[200] H. F. Song, S. Rachel, C. Flindt, I. Klich, N. Laflorencie, and K. Le Hur, "Bipartite fluctuations as a probe of many-body entanglement," Phys. Rev. B **85**, 035409 (2012).

[201] I. Klich, G. Refael, and A. Silva, "Measuring entanglement entropies in many-body systems," Phys. Rev. A **74**, 032306 (2006).

[202] I. Klich and L. Levitov, "Quantum noise as an entanglement meter," Phys. Rev. Lett. **102**, 100502 (2009).

[203] H. Steinberg, G. Barak, A. Yacoby, L. N. Pfeiffer, K. W. West, B. I. Halperin, and K. Le Hur, "Charge fractionalization in quantum wires," Nature Physics **4**, 116 (2007).

[204] G. Vidal, J. I. Latorre, E. Rico, and A. Kitaev, "Entanglement in quantum critical phenomena," Phys. Rev. Lett. **90**, 227902 (2003).

[205] J. I. Latorre, E. Rico, and G. Vidal, "Ground state entanglement in quantum spin chains," Quantum Info. Comput. **4**, 48 (2004).

[206] S. R. White, "Density matrix formulation for quantum renormalization groups," Phys. Rev. Lett. **69**, 2863 (1992).

[207] Schollwöck, U., "The density-matrix renormalization group," Rev. Mod. Phys. **77**, 259 (2005).

[208] B. Reulet, J. Senzier, and D. E. Prober, "Environmental effects in the third moment of voltage fluctuations in a tunnel junction," Phys. Rev. Lett. **91**, 196601 (2003).

[209] G. Gershon, Y. Bomze, E. V. Sukhorukov, and M. Reznikov, "Detection of non-gaussian fluctuations in a quantum point contact," Phys. Rev. Lett. **101**, 016803 (2008).

[210] C. Flindt, C. Fricke, F. Hohls, T. Novotný, K. Netočný, T. Brandes, and R. J. Haug, "Universal oscillations in counting statistics," Proceedings of the National Academy of Sciences **106**, 10116 (2009).

[211] E. V. Sukhorukov, A. N. Jordan, S. Gustavsson, R. Leturcq, T. Ihn, and K. Ensslin, "Conditional statistics of electron transport in interacting nanoscale conductors," Nature Physics **3**, 243 (2007).

[212] S. Ejima, H. Fehske, and F. Gebhard, "Dynamic properties of the one-dimensional Bose-Hubbard model," EPL (Europhysics Letters) **93**, 30002 (2011).

[213] V. A. Kashurnikov and B. V. Svistunov, "Exact diagonalization plus renormalization-group theory: Accurate method for a one-dimensional superfluid-insulator-transition study," Phys. Rev. B **53**, 11776 (1996).

[214] S. M. A. Rombouts, K. Van Houcke, and L. Pollet, "Loop updates for quantum monte carlo simulations in the canonical ensemble," Phys. Rev. Lett. **96**, 180603 (2006).

[215] A. M. Läuchli and C. Kollath, "Spreading of correlations and entanglement after a quench in the one-dimensional bose?hubbard model," Journal of Statistical Mechanics: Theory and Experiment **2008**, P05018 (2008).

[216] P. Calabrese and J. Cardy, "Evolution of entanglement entropy in one-dimensional systems," Journal of Statistical Mechanics: Theory and Experiment **2005**, P04010 (2005).

[217] P. Calabrese and J. Cardy, "Quantum quenches in 1+1 dimensional conformal field theories," Journal of Statistical Mechanics: Theory and Experiment **2016**, 064003 (2016).